Coherent Light-Matter Interactions in Monolayer Transition-Metal Dichalcogenides

by

Edbert Jarvis Sie

B.S. Physics, Nanyang Technological University

Submitted to the Department of Physics
in partial fulfillment of the requirements for the degree of

Doctor of Philosophy
at the Massachusetts Institute of Technology

June 2017

Signature redacted

Author..... .....
Department of Physics
May 24, 2017

Signature redacted

Certified by..... .....
Nuh Gedik
Associate Professor of Physics
Thesis Supervisor

Signature redacted

Accepted by..... .....
Nergis Mavalvala
Professor of Physics
Associate Head, Department of Physics

Coherent Light-Matter Interactions in Monolayer Transition-Metal Dichalcogenides

Edbert Jarvis Sie

Submitted to the Department of Physics
on May 24, 2017, in partial fulfillment of the
requirements for the degree of
Doctor of Philosophy

Abstract

Semiconductors that are thinned down to a few atomic layers can exhibit novel properties beyond those encountered in bulk forms. Transition-metal dichalcogenides (TMDs) such as MoS_2, WS_2 and WSe_2 are prime examples of such semiconductors. They appear in layered structure that can be reduced to a stable single layer where remarkable electronic properties can emerge. Monolayer TMDs have a pair of electronic valleys which have been proposed as a new way to carry information in next generation devices, called valleytronics. However, these valleys are normally locked in the same energy level, which limits their potential use for applications.

This dissertation presents the optical methods to split their energy levels by means of coherent light-matter interactions. Experiments were performed in a pump-probe technique using a transient absorption spectroscopy on MoS_2 and WS_2, and a newly developed XUV light source for time and angle-resolved photoemission spectroscopy (TR-ARPES) on WSe_2 and WTe_2. Hybridizing the electronic valleys with light allows us to optically tune their energy levels in a controllable valley-selective manner. In particular, by using off-resonance circularly polarized light at small detuning, we can tune the energy level of one valley through the optical Stark effect. At larger detuning, we observe a separate contribution from the so-called Bloch-Siegert effect, a delicate phenomenon that has eluded direct observation in solids. The two effects obey opposite selection rules, which enables us to separate the two effects at two different valleys.

Monolayer TMDs also possess strong Coulomb interaction that enhances many-body interactions between excitons, both bonding and non-bonding interactions. In the former, bound excitonic quasiparticles such as biexcitons play a unique role in coherent light-matter interactions where they couple the two valleys to induce opposite energy shifts. In the latter, non-bonding interactions between excitons are found to exhibit energy shifts that effectively mimics the Lennard-Jones interactions between atoms. Through these works, we demonstrate new methods to optically tune the energy levels of electronic valleys in monolayer TMDs.

Thesis Supervisor: Nuh Gedik
Title: Associate Professor of Physics

Acknowledgments

First and foremost, I would like to thank my advisor Prof. Nuh Gedik for his mentorship and support. He has been a constant source of inspiration since I first started my graduate studies. Actually it was even before that. I remember my first meeting at a conference in Boston where he presented a real-time image of crystalline lattice motion. The idea of watching Michael Jackson performing Billie Jean flashed through my head, because he was that cool and inspiring, and he continues to be so. He has been a tremendous support since day one, where I was given the opportunity to design and build the XUV beamline for ARPES in the lab as well as the freedom to build the white-light setup next to it. His vigor to make new innovations in time-resolved experiments is always inspiring. Throughout my graduate studies, he has been a true role model of how to be a good scientist and to search for a good question like 'So what?' in a perfectly well stated manner. I also learn that "no problem is too small, and no problem is too big". He gave me and other group members many opportunities to attend international conferences with the intention that we could learn how to communicate our findings with new people and meet fellow scientists in the field. Despite his busy schedule, he always makes time to discuss with group members regularly through the weekly group meetings, bi-weekly sub-group meetings, and individual meetings. Apart from discussing about research, he has been a constant source of encouragement and guidance where he would chat to discuss about our personal matters and future careers. Sometimes I was left wondering how one person can do so much in a little time and can become so quick and sharp minded like laser while being gentle at all times. I sincerely thank Nuh for every aspect of my graduate education.

I am very grateful to other members of my thesis committee, Prof. Liang Fu and Prof. Pablo Jarillo-Herrero. Liang has been a theory advisor to me where many fundamental explanations of my experiments are inspired by him. One of many insightful wisdoms, he taught me that the optical Stark effect can be extended to create a topologically nontrivial phase of matter in monolayer TMDs. Discussing research with him has always been exciting and stimulating, not because we know anything more about the theory, but because he knows very well the reality about what the experiments can do. Much of the theory I understand has been patiently explained to me after I went to his office several times. He showed me to use simple diagrams and mathematical expressions that capture the essence of physics. I will remember to use the Cartesian coordinates every time I face the spherical harmonics.

Pablo has been my academic advisor at MIT where he regularly checked up my academic progress throughout my graduate studies. His office is like the holy and respected temple where I can freely confess about my classes, research progress, academic career, and ask for his guidance. I always remember his suggestions that a lot of times it is better to complete tasks one at a time rather than attempting to complete everything at once. I sincerely thank Pablo for letting me have the access for his labs to borrow some optics or to perform sample

characterization with his group members. Every time I entered his fabrication lab, most likely to ask his group members out for lunch or dinner, I always feel humbled because this lab have very highly skilled people who are capable of creating cool devices.

My learning and working experience in the lab has been very enjoyable because of the highly spirited colleagues in the Gediklab. I am very grateful to Yihua Wang (now professor at Fudan) who has taught me the 'Introduction to Gediklab 101' since I first joined the group in August 2011. He constructed the ARPES system in the lab and taught me how it works and how to use it. I learned how to use Solidworks from him in order to accurately design and assemble many ultra high vacuum (UHV) apparatus for the new extreme ultraviolet (XUV) beamline in the lab. Since then it has becoming my favorite software to draw three-dimensional figures, some of them appears in the last chapter of this dissertation. David Hsieh (now professor at Caltech) has always been inspiring and he introduced me to many interesting material systems that can be explored. Timm Rohwer has been a great colleague that I had a real pleasure to work together with and a good friend to have. He joined the group during my third year and since then we have been working together to setup the XUV beamline for ARPES. He has an infinite reservoir of energy and motivation, which constantly inspires me. There is no lab equipment that he cannot fix. Zhanybek Alpichshev has been a constant source of joy and inspiration in the office. I am very fortunate to share an office with him. I learn something new almost every time I had conversation with him. There is no question that he cannot answer. Joshua Lui (now professor at UC Riverside) taught me how to write stories clearly and worth telling. He gave me very helpful advices during my transition from a graduate student into a more devoted profession in later stage of my career.

I also enjoyed having discussions with former group members James McIver, Alex Frenzel, Darius Torchinsky, Daniel Pilon, Fahad Mahmood, Byron Freelon, Inna Vishik, Hengyun Zhou, Mahmoud Ghulman, and Steven Drapcho. As well as with current group members Ozge Ozel, Changmin Lee, Emre Ergecen, Alfred Zong, Anshul Kogar, Carina Belvin, Suyang Xu, Nikesh Koirala, Mehmet Yilmaz, Guy Marcus, and Edoardo Baldini. They are very talented individuals and enjoyable to work with in the lab. There were many good memories that we shared together which enriched my experience as a graduate student at MIT.

Outside our lab, I am very thankful to Prof. Yi-Hsien Lee (now professor at NTHU Taiwan) and Prof. Jing Kong for their expertise and generous supports to synthesize the high-quality monolayer TMDs that I used in all of my experiments. My first encounter with Yi-Hsien in the corridor of MIT Building 13 results in a long-lasting friendship and professional collaboration, which I look forward to continue in future. I would like to thank Wenjing Fang, who happens to be the source of all interesting information surrounding our community. I remember her telling me about the new thin semiconducting materials that could be synthesized in Jing's group with the help from Yi-Hsien. This started my pursuit in studying the monolayer TMDs. I am very grateful to my wonderful friend and colleague Qiong Ma from Pablo's group for being my study buddy over the years. She shows a great and professional enthusiasm at work

(and outside…), which inspires me to work harder and be more productive. Every time I have questions regarding graphene or low-dimensional devices, she has always been the first person I had to consult with, and she usually gave more useful tips beyond my questions. She is like a living dictionary made of graphene; … I mean a strong one that can even hold an elephant! Everybody knows this is not a joke, right. I also thank Yaqing Bie and Yuan Cao for being my dinner buddies whenever I have a craving for good foods (like every time…). Yaqing, the 'Queen of Optics' in Pablo's group, has always been helpful every time I wanted to discuss about optics in low-dimensional devices. I also thank the rest of the people in MIT Building 13: Yafang Yang, Linda Ye, Shengxi Huang, Yuxuan Lin, Lin Zhou, and Xi Ling (now professor at Boston University) who have been amusing companions during my graduate studies, as well as in exploring different options for oriental foods. I thank Raga Markely for being my lunch buddy where I can also share my thoughts about everyday life and future career. I am very grateful to Monica Wolf who has done a lot more than being our admin secretary. She took care everything about travel plans, reimbursements, lab equipment purchases, employment transition, as well as the big celebration for thesis defense (with the help from Qiong and Ozge) that I went through, multiplied by the number of people like me in MIT Building 13, floor 2.

I would like to thank Christopher Gies and Alexander Steinhoff in University of Bremen, Germany for their immense contributions in the theoretical study of highly excited monolayer TMDs, presented in Chapter 7. It was a wonderful experience to collaborate with Chris and Alex, from whom I learned a great deal about the role of plasma screening in monolayer TMDs.

Throughout the years as a graduate student, there are also other researchers whom I often encountered at conferences: Jonghwan Kim, Long Ju, Xiaoxiao Zhang, Yilei Li, Ziliang Ye, Jan Buss, and Shiang Fang. I am very grateful to know them, which makes the conference visit more interesting and more fruitful, because we work in a similar field and we can learn from each other. I am sure I will see them more often in future, and I look forward to it.

My very special gratitude goes to my parents for their unconditional love, support and wisdom. My mother taught me how to speak, to stand, and to love one another. My father fixed what my mother taught me.

Edbert J. Sie
Cambridge, MA

Table of Contents

Chapter 1

Introduction

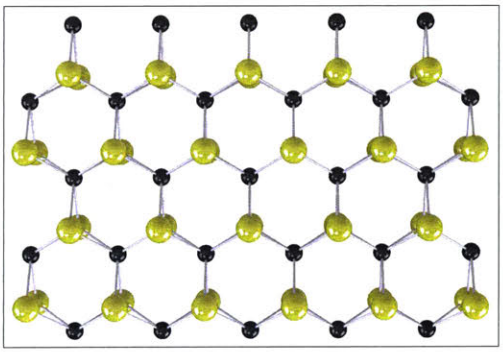

Contents

Two-dimensional materials can exhibit novel properties beyond those normally encountered in the bulk compounds. Most evidently is the change in their electronic density of states and their increasing susceptibility to a Peierls transition. More interestingly, a number of fascinating phenomena emerge from two-dimensional materials. This includes quantum well system with quantized energy levels, two-dimensional electron gas (2DEG) that can exhibit the integer and fractional quantum Hall effect, layered materials that demonstrate high-temperature superconductors, as well as topological insulators that feature nontrivial metallic states at the surface while remain insulating on the inside. Some of these material systems can appear as compounds from multiple different elements with complex lattice structures while maintaining their quasi two-dimensionality.

Graphene, a single layer of carbon atoms, is a prime example of such 2D materials that can exhibit some of the above remarkable properties despite its very simple structure. The electronic structure of graphene is described by a massless Dirac fermion at around the Fermi level, with the valence and conduction bands touching at a single point [7]. This allows graphene to exhibit extremely high electron mobility, which is a promising property in developing nanoscale electronic applications. However, the gapless electronic structure in graphene makes it challenging to use this material for switchable electronics such as transistors. Various approaches can be used to open a gap in graphene [8], for example by placing graphene above a particular substrate that breaks graphene's sublattice symmetry. However, the resulting gap induced this way is reported to be around 100 meV [9], which is still rather small for practical applications.

Transition-metal dichalcogenides (TMDs) comprise a family of II-VI semiconductors such as MoS_2, WS_2, $MoSe_2$ and WSe_2. These materials are layered in structure, from which we can isolate a monolayer of TMDs through mechanical exfoliation or chemical vapor deposition (CVD) growth method [10, 11]. Monolayer TMDs have a lattice structure similar to graphene but, unlike graphene, these materials possess a semiconducting gap between 1-2 eV. The large gap in this class of materials offers promising electronic applications based on two-dimensional materials. Recently, a microprocessor based on a 2D semiconductor (MoS_2) has been reported [12]. The device consists of 115 transistors

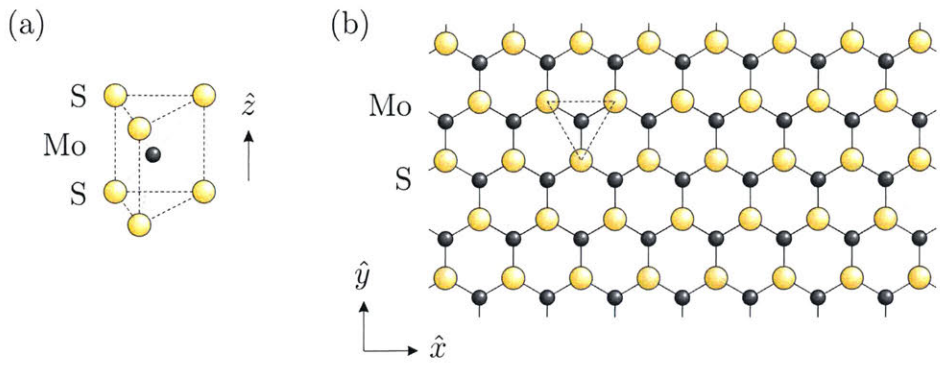

Figure 1.1: (a) Unit cell of monolayer 2H-MoS_2 in a trigonal prismatic arrangement. This structure lacks an inversion center. **(b)** Top view of monolayer 2H-MoS_2.

comprising all basic building blocks that are common to most microprocessors. While this class of materials could be an important element for the development of future 2D devices, they are found to have novel electronic and optical properties as we discuss below.

1.1. Monolayer transition-metal dichalcogenides (TMDs)

The properties of monolayer TMDs were first studied through pioneering optical measurements on monolayer MoS_2 by Mak et al. [13] and Splendiani et al. [14]. Monolayer MoS_2 is a one-unit-cell thick semiconductor with a graphene-like hexagonal lattice of Mo and S atoms where the S-Mo-S layers are stacked in a trigonal prismatic arrangement **(Fig 1.1a-b)**. It is a direct band gap semiconductor with an optical energy gap of 1.96 eV (10 K) at K and K' valleys in the Brillouin zone and a valence band splitting of 160 meV due to strong spin-orbit coupling **(Fig 1.2)**. Other monolayer TMDs have similar properties but the magnitudes differ slightly, for example monolayer WS_2 has an optical gap of 2.1 eV at 300 K and a valence band splitting of 400 meV. Monolayer TMDs are promising material systems for future low-energy electronics because it has a unique spin-valley coupling and a strong Coulomb interaction.

1.1.1. Electronic bandstructure

In this section we describe the electronic bandstructure of monolayer MoS_2, following the theoretical studies by Xiao et al. [15] and Liu et al. [2, 16], but the general

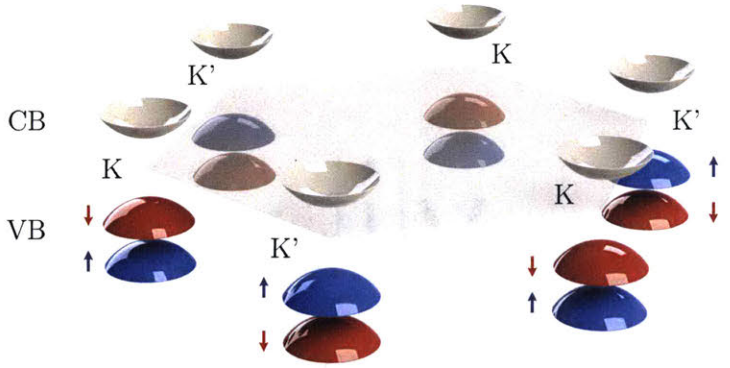

Figure 1.2: Hexagonal Brillouin zone of monolayer MoS_2. The band edges from conduction bands (CB) and valence bands (VB) are located at the K and K' points.

description should also applies to WS_2, WSe_2, and $MoSe_2$ monolayers. The bandstructure of monolayer MoS_2 around the gap is well described by considering the Mo-*d* orbitals and S-*p* orbitals. This material has a unit cell that forms a trigonal prismatic coordination around the Mo atom that splits its d orbitals into three groups: $A_1(d_{z^2}), E(d_{xy}, d_{x^2-y^2})$ and $E'(d_{xz}, d_{yz})$. The mirror symmetry along the $\hat{z}$ direction allows a hybridization between A_1 and E orbitals, which constitutes the gap opening at the K and K' valleys in the Brillouin zone **(Fig 1.3)**. In the vicinity of these symmetry points, the wavefunction of the bands are described by the following symmetry-adapted basis functions:

$$|\phi_c\rangle = |d_{z^2}\rangle, \qquad |\phi_v\rangle = \frac{1}{\sqrt{2}}\left(|d_{x^2-y^2}\rangle \pm i|d_{xy}\rangle\right) \tag{1.1}$$

where $|\phi_c\rangle$ is the basis for conduction band, $|\phi_v\rangle$ for valence band, and the $\pm$ sign denotes the K or K' valley index. The two-band Hamiltonian of monolayer MoS_2 mimics that of graphene because both systems have similar symmetry properties, except for the gap opening due to the differing on-site potentials between the Mo and S sublattices and the strong spin-orbit coupling (SOC) originated from the Mo-*d* orbitals:

$$\hat{H} = at\left(\pm k_x\hat{\sigma}_x + k_y\hat{\sigma}_y\right) + \frac{\Delta}{2}\hat{\sigma}_z \mp \lambda\frac{\hat{\sigma}_z - 1}{2}\hat{s}_z \tag{1.2}$$

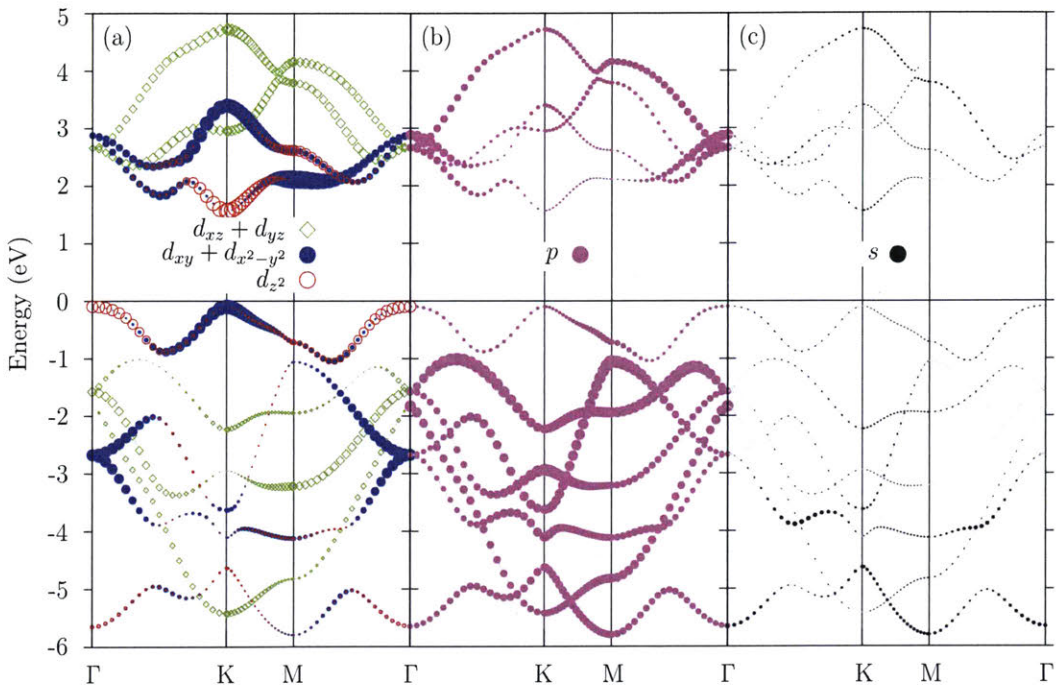

Figure 1.3: Atomic orbital projection of band structures for monolayer MoS_2 from first-principle calculations, without spin-orbit coupling. Fermi energy is set to zero. Symbol size is proportional to its contribution to corresponding state. **(a)** Contributions from Mo-*d* orbital. **(b)** Total contributions from *p* orbitals, dominated by S atoms. **(c)** Total *s* orbitals. Figure is obtained from Reference [2].

where a is the lattice constant, t the hopping integral, k the wavevector, $\hat{\sigma}$ the Pauli matrices for the two basis functions, Δ the energy gap, 2λ the spin splitting at the top of the valence band caused by the SOC interaction $H' = \lambda \boldsymbol{L} \cdot \boldsymbol{S}$ ($m_l = \pm 2, m_s = \pm 1/2$), and $\hat{s}_z$ the Pauli matrices for the electron's spin.

There are three important features that distinguish monolayer MoS_2 from graphene. *First*, the resulting electronic structure is described by a massive Dirac fermion due to the finite gap in the second term. This allows an interband electronic transition at the K and K' valleys that can be induced through an optical excitation in the visible regime. *Second*, the two valleys possess finite and opposite Berry curvatures owing to the lack of crystalline inversion symmetry. This gives rise to distinct optical selection rules, which we will discuss further in the next section. *Third*, the SOC contribution in the third term leads to a large spin splitting at the valence band top (160 meV). Meanwhile, the spin splitting at the conduction band bottom is negligible in the first-order approximation because it is mostly

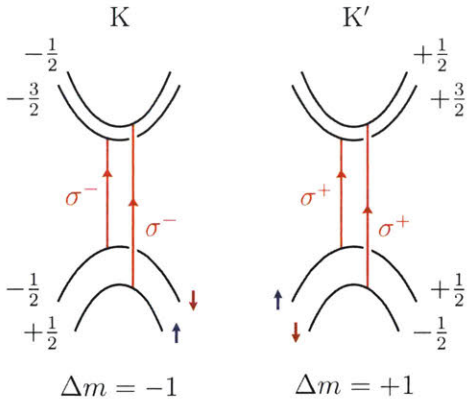

Figure 1.4: Optical selection rules in monolayer MoS_2.

composed by d_{z^2} orbital ($m_l = 0$). Its magnitude can be obtained by using a second-order perturbation from the Mo-d orbitals and a first-order perturbation from the minor S-p orbitals ($m_l = \pm 1$) [4]. Although the conduction band splitting is much smaller in magnitude (3 meV in MoS_2), it plays an important role in the formation of stable dark excitons in monolayer WS_2 and WSe_2 [17] where the splitting is larger (20-40 meV) and inverted.

1.1.2. Optical selection rules

In monolayer TMDs, the two valleys couple differently with left and right circularly polarized light [15, 18-20]. At K valley, optical transition from the valence band top (VB) to the conduction band bottom (CB) is induced exclusively by left-circularly polarized light. At K' valley, the optical transition is induced exclusively by right-circularly polarized light. Such valley selection rules arise from the different quantum numbers m associated to the bands at the two valleys **(Fig 1.4)**. At K valley, the valence bands are assigned $m = -1/2$ and $+1/2$ for the down-spin and up-spin respectively, while the conduction bands are assigned $m = -3/2$ and $-1/2$ for the down-spin and up-spin respectively. Interband transitions from VB to CB can occur through absorption of left-circularly polarized light (σ^-) that carries an angular momentum $\Delta m = -1$, where we consider electric dipole approximation that leaves the spin unchanged. At K' valley, the quantum numbers have the opposite signs with respect to the K valley because of time-reversal symmetry. Hence,

interband transition at K' valley can occur through absorption of right-circularly polarized light (σ^+) with $\Delta m = +1$.

The above description can explain the origin of valley selection rules because the quantum numbers are given. However, obtaining these quantum numbers is not as straightforward as the addition of orbital and spin angular momenta in atoms. Isolated atoms in free space have a full spherical symmetry that allows electron orbitals to acquire magnetic quantum numbers $m = 0, \pm1, \pm2, \pm3, ...$ with no limit. Meanwhile, the crystal lattice of monolayer TMDs has a space group D_{3h}^1 that imposes a trigonal symmetry C_3 at the K symmetry points, so the linear combination of atomic orbitals (LCAO) throughout the lattice must conform this symmetry. This limits the effective quantum numbers $m = 0, \pm1, \pm2$ (modulo 3) that can be present in the system.

In order to obtain the quantum numbers of the conduction and valence bands, we must find the eigenvalue γ_α ($\alpha = c, v$) of the C_3 rotation on the Bloch functions $C_3\psi_\alpha = \gamma_\alpha\psi_\alpha$. This should include both the constructing atomic orbitals and the plane wave component of the Bloch functions, expressed as

$$\psi_\alpha(\boldsymbol{r}) = \frac{1}{\sqrt{N}}\sum_{\boldsymbol{R}} e^{\pm i\boldsymbol{K}\cdot(\boldsymbol{r}+\boldsymbol{\delta})} d_\alpha(\boldsymbol{r} - \boldsymbol{R} - \boldsymbol{\delta}) \tag{1.3}$$

where R is the lattice vector, δ is the position of Mo atom in the unit cell, $d_c = d_{z^2}$ and $d_v = \left(d_{x^2-y^2} \pm id_{xy}\right)/\sqrt{2}$. There are two contributions to the eigenvalue, first the C_3 rotation about the center of atomic orbital $C_3 d_c = d_c$ and $C_3 d_v = e^{\pm i2\pi/3} d_v$, and second the change of lattice phase factor $e^{\pm i\boldsymbol{K}\cdot\boldsymbol{r}}$ at each lattice site. The eigenvalue γ_α depends on the position of the rotation center ρ, which can be Mo atom, S atom or the h position (center of hexagon), as shown in **Fig 1.5 (inset)**. By using symmetry analysis of C_3 on the above Bloch functions, we can obtain the eigenvalue

$$\gamma_\alpha^\rho = e^{\pm i\boldsymbol{K}\cdot(C_3^{-1}\boldsymbol{\delta}-\boldsymbol{\delta})}\gamma_{d_\alpha} \tag{1.4}$$

where $\boldsymbol{\delta}$ is the Mo atom position with respect to the rotation center ρ, and γ_{d_α} is the eigenvalue about the center of atomic orbitals [16]. In short, the orbital quantum number

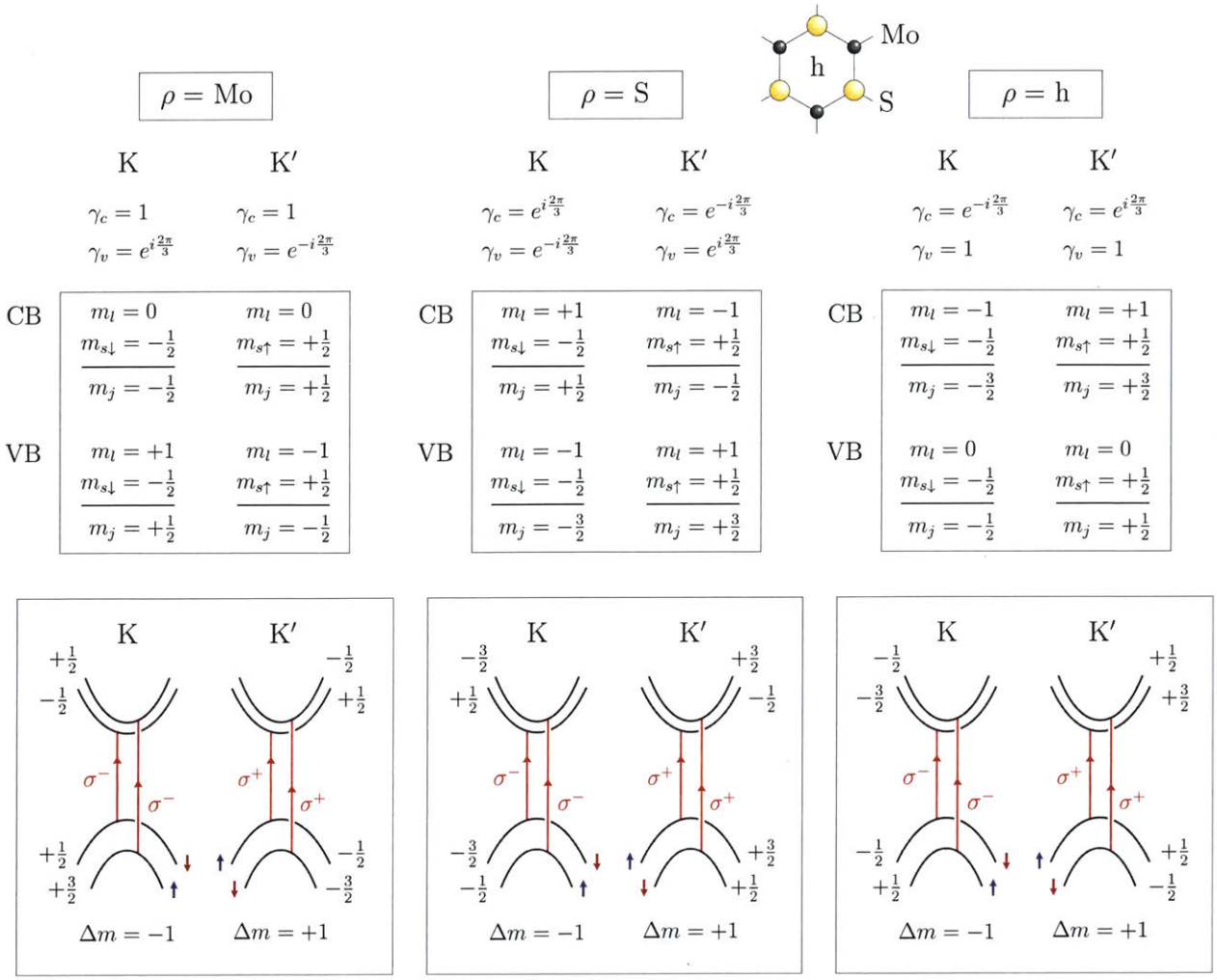

Figure 1.5: The C_3 rotation eigenvalues $\gamma_{c,v}$ [2] and quantum numbers of bands in monolayer MoS_2, specified for different rotation centers ρ = Mo, S, and h positions **(see inset)**. The quantum numbers inside the middle row are shown only for the band edges, i.e. spin-down at K valley and spin-up at K' valley.

m_l is obtained from $\gamma = \exp(i2\pi m_l/3)$. The simplest example is given at ρ = Mo ($\boldsymbol{\delta} = 0$) where the lattice phase contribution is zero and hence $\gamma_c^{Mo} = \gamma_{d_c} = 1$ and $\gamma_v^{Mo} = \gamma_{d_v} = e^{\pm i2\pi/3}$. The conduction bands are assigned $m_l = 0$ at K and K' valleys, while the valence bands are assigned $m_l = -1$ at K valley and $+1$ at K' valley. By adding the spin contributions m_s, we can obtain the total quantum numbers m_j of these bands **(Fig 1.5)**.

We emphasize that the quantum numbers associated with conduction and valence bands depend on the choice of rotation center, but the upward optical transition between

the spin-conserving bands remain the same, i.e. $\Delta m = -1$ at K valley and $+1$ at K' valley. This is a consequence of the lattice symmetry in monolayer TMDs that also gives rise to the nonzero and opposite Berry curvatures at the K and K' valleys. Berry curvature can be viewed as the self-rotating motion of the electron wavepacket or the orbital magnetic moment, and the opposite Berry curvatures between the K and K' valleys give rise to the opposite selection rules at the two valleys.

1.1.3. Excitons

Upon photoexcitation, an electron will occupy the conduction band and leave a hole in the valence band. They have opposite charges and can attract each other through Coulomb interaction. This allows a formation of bound quasiparticle called an exciton. Monolayer TMDs are atomically thin semiconductors; so electronic excitation is confined within 2D structure similar to the situation in quantum wells. There are two important consequences that differentiate the excitons in this system and in the bulk. First, there is a strong spatial overlap between the electron and hole orbitals in the $\hat{z}$ direction due to quantum confinement. Second, the electric field between the electron-hole pair can penetrate outside the material where screening is absent **(Fig 1.6a-c)**. These two features enhance the Coulomb attraction significantly and result in the large excitonic binding energy of 320 meV in monolayer TMD WS_2 as compared to 50 meV in bulk WS_2 [6]. The binding energies are determined through comparing the series of exciton energy levels obtained experimentally and theoretically. Note that as the electron-hole separation increases, a larger amount of electric field between them penetrates outside the material and the overall screening gets suppressed. This leads to a pronounced deviation from the usual hydrogenic series of exciton energy levels.

The optical selection rules in previous section are discussed in terms of one-particle picture where Coulomb interaction between the electron-hole pair is ignored. Note that the selection rules result from the symmetry properties in monolayer TMDs. Since Coulomb interaction appears as $1/r$ with a full spherical symmetry, the symmetry properties in monolayer TMDs are unaffected. Thus, novel selection rules at the two valleys are

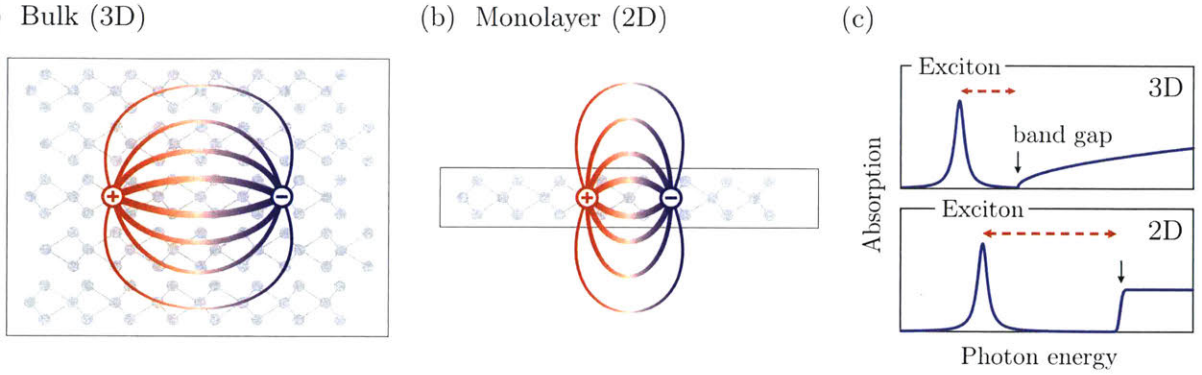

Figure 1.6: Interactions between electron and hole that form an exciton is mediated by Coulomb attraction. **(a)** In bulk, the electric field is screened by the surrounding material. **(b)** In monolayer, large fraction of the electric field penetrates outside the material into the vacuum where screening is absent, or to an appropriate substrate where screening can be varied. **(c)** The suppressed screening in monolayer leads to a larger exciton binding energy with respect to the band gap. Figures are adapted and redrawn from Reference [6].

maintained, and excitons can be created in a valley-selective manner using circularly polarized light.

1.2. Time-resolved spectroscopy

Monolayer TMDs have a pair of electronic valleys (K and K') whose index can be used as a new degree of freedom for next generation *valleytronics*. Owing to the optical selection rules, we can use left-circularly polarized light to promote charge carriers at K valley to carry information with valley index of -1. However, since the two valleys are energetically degenerate, these carriers can scatter from K valley to K' valley and carry the incorrect valley index of +1 **(Fig 1.7)**. Such intervalley scattering introduces a valley index mixture throughout propagation until the population between the two valleys reaches equilibrium. In order to use the valley index for practical valleytronic devices, it is desirable to suppress the intervalley scattering. There are two methods to follow up on this line: (i) split the energy levels between the two valleys, and (ii) identify the dominant intervalley scattering mechanisms and suppress its scattering rate. In our approach, we use light-matter interactions in a time-resolved manner to achieve this.

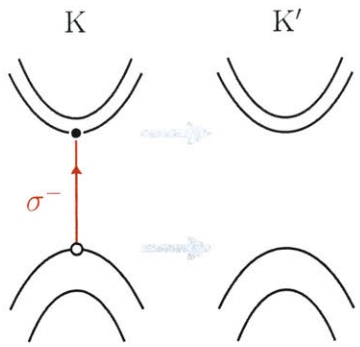

Figure 1.7: Intervalley scattering of charge carriers from K valley to K' valley.

1.2.1. Coherent light-matter interactions

Hybridizing light with electrons in materials can result in newly created photon-dressed states or Floquet states with energy levels that are modified from their original states. An effective hybridization can be achieved in materials that are subject to a *coherent* light field so there exists a phase correlation between the induced polarization and the incident light. Hence the resulting hybrid quasiparticle, when written using Bogoliubov transformation, can maintain well-defined amplitude and energy. This is in a similar situation with the forced harmonic oscillator, where the interaction energy is transferred periodically between light and electrons in materials without energy loss. In practice, energy loss can occur through incoherent interactions. This could be mediated by dissipative scattering channels upon absorption of resonance light.

In order to suppress the absorption process, we use coherent light source (laser) that is tuned off-resonance with the material system. Coherent interactions with off-resonance light can be used to shift the energy levels of materials. As we will discuss in later chapters, the energy shift (often called the "light shift") can occur through two mechanisms, the optical Stark shift and the Bloch-Siegert shift. These processes can be used to split the energy level between the two valleys using circularly polarized light that breaks time-reversal symmetry. This optical technique can offer a much larger energy splitting as compared to that of magnetic field.

1.2.2. Quasi-equilibrium dynamics

In monolayer TMDs, excitons can be created at a specific valley and switched to the other valley through intervalley scattering. The lifetime of this scattering process can be measured using pump-probe spectroscopy, which can occur in subpicosecond timescale. In this experiment, a left-circularly polarized pump pulse is used to create excitons at K valley and no excitation at K' valley. After some time delay, exciton populations at K and K' valleys are monitored using left- and right- circularly polarized probe pulse. The intervalley scattering process can be measured through the increasing bleaching signal at K' valley in time-resolved absorption spectroscopy or through the decreasing polarization rotation of the probe pulse in time-resolved Faraday or Kerr spectroscopy. The obtained scattering lifetime can be scrutinized through its dependencies in temperature, charge doping, spin-orbit coupling strength, exciton density, and substrates. As such, the dominant intervalley scattering mechanism can be identified and the scattering rate can be suppressed.

Mutual interactions between excitons can also be probed using time-resolved spectroscopy. In later chapters, we will discuss the bound state of two excitons, called biexciton, which can be induced using two-step excitation. Two excitons that are created at two different valleys can form an *intervalley biexciton*, which possess a unique combination of orbital, spin and valley degree of freedoms, with no analogue in atomic systems. Non-bonding interactions between two separate excitons can also occur through atom-like van der Waals interactions. Unlike atoms, however, excitons usually have much smaller binding energies and can break into free electron-hole pairs or plasma. This introduces complexities to non-bonding interactions between excitons in conventional semiconductors. Monolayer TMDs, on the other hand, provide a special platform for exploring quasiparticle interactions because of their unique two-dimensionality and strong Coulomb interactions, which render these quasiparticles stable at room temperature. This should allow more in depth studies of such interactions at higher excitation density regime that was previously unexplored in conventional semiconductors.

Chapter 2

Time-resolved absorption spectroscopy

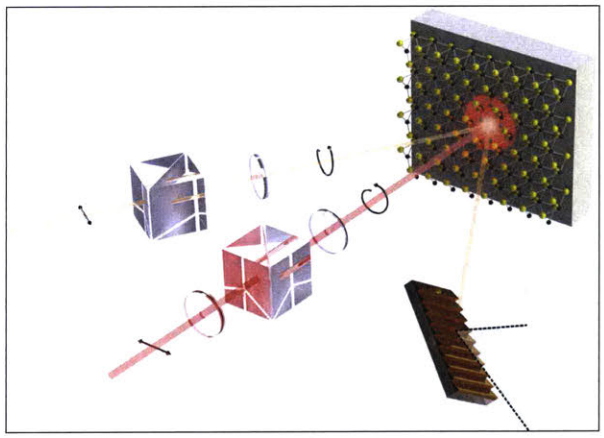

Contents

This dissertation work emphasizes on the exciton energy shift that is induced by femtosecond light pulses. At equilibrium, the exciton energy level in monolayer TMDs sits in the visible regime, e.g. $E_0 = 2$ eV in monolayer WS_2. In order to detect this energy shift, we need a broadband probe pulse that is centered in the visible spectrum. White light continuum generation is a nonlinear optical process capable of producing such broadband light pulse between 500-700 nm ($\hbar\omega = 1.8 - 2.4$ eV). In this chapter, we will discuss about time-resolved absorption spectroscopy setup (or simply *transient absorption*) that utilizes white light continuum to probe the exciton energy shift in monolayer TMDs. In the first section, we will show the overview of the transient absorption setup. In later sections, we will discuss in more details about (i) laser amplifier, (ii) optical parametric amplifier, and (iii) white light continuum generation. Finally, we will discuss about the data analysis based on the optical physics of monolayer materials on a transparent substrate.

2.1. Experimental setup

2.1.1. Overview

Transient absorption spectroscopy consists of synchronized pump pulses and broadband probe pulses to monitor the pump-induced absorption of materials. Light has three properties namely photon energy, polarization and intensity that, when tuned precisely, can induce various nonequilibrium phenomena in materials. Examples are resonant excitation of quasiparticles, off-resonance shifting of energy levels, and valley-selective light-matter interaction. For this reason, a transient absorption setup can incorporate different stages of light management area on the optical table to generate light pulses with different photon energies and to control their polarizations and intensities before reaching the sample.

The overview of this transient absorption setup is schematically drawn in **Fig 2.1**. In this setup, we use a Ti:sapphire laser amplifier producing laser pulses with duration of 50 fs and at 30 kHz repetition rate. Each pulse is split into two arms. For the pump arm, the pulses are sent to an optical parametric amplifier (OPA) to generate tunable photon energies and modulated by an optical chopper; while for the probe arm the pulses are sent

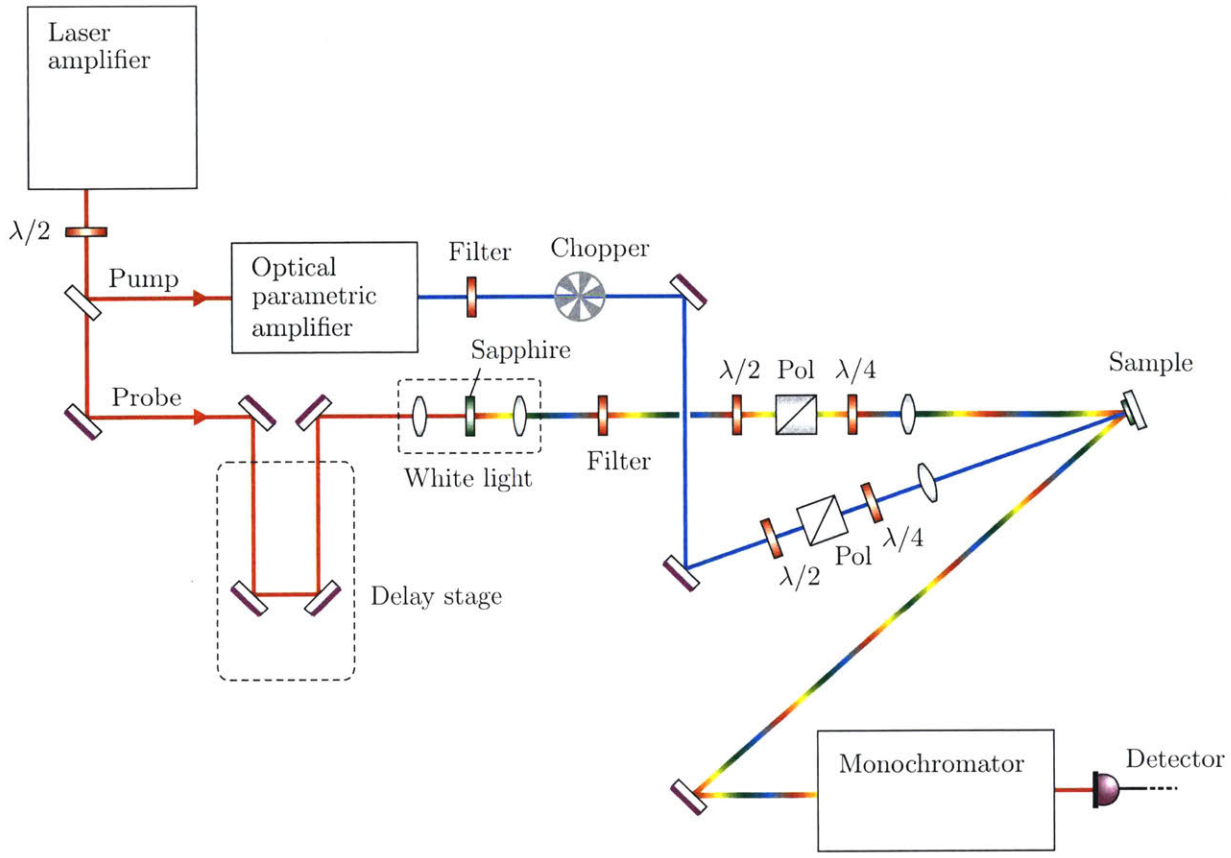

Figure 2.1: Optical layout of transient absorption spectroscopy setup.

through a delay stage and a white light continuum generator. The pump and probe polarizations are varied separately by two sets of polarizers and quarter-wave plates, allowing us to perform polarization-dependent measurements, and an additional half-wave plate for tuning the pump pulse intensity. The two beams are focused at the sample, and the probe beam is reflected to a monochromator and a photodiode for lock-in detection. The optical chopper is externally triggered at 7.5 kHz by the 30 kHz laser amplifier. Here, in every optical modulation cycle, two adjacent pump pulses are passed and the next two adjacent pump pulses are blocked by the optical chopper. By scanning the grating and the delay stage, we are able to measure induced reflection $\Delta R/R$ (hence induced absorption $\Delta\alpha$) as a function of energy and time delay.

2.1.2. Laser amplifier

One important aspect to consider when setting up a transient absorption setup is the laser pulse energy. White light continuum generation is a nonlinear optical process that requires femtosecond pulse energy of 3-5 μJ when using a transparent nonlinear medium such as a sapphire glass. Although this requirement is easily managed using a tiny fraction from a laser amplifier's output, it certainly is a huge energy barrier for a laser oscillator. Femtosecond laser amplifiers can produce pulse energy between 10 μJ to 100 mJ, while laser oscillators are limited with pulse energy between 10-100 nJ. There is an alternative to generate white light continuum from laser oscillators by using nonlinear photonic crystal fibers. However, laser amplifiers offer more versatile options for transient absorption setup because the remaining pulse energy can be used to generate laser pulses at various wavelengths in the ultraviolet, visible and mid-infrared using an optical parametric amplifier with typical pulse energy input of 200 uJ.

In our experiment, we use a Ti:sapphire laser amplifier Wyvern 500 from KM Labs and set its repetition rate to 30 kHz. The overview of this amplifier is schematically drawn in **Fig 2.2** and briefly discussed as follows. A mode-locked femtosecond oscillator Griffin (KM Labs) generates laser pulses with pulse duration 50 fs, energy 2 nJ, center wavelength 790 nm, and repetition rate 80 MHz. This oscillator output (seed pulse) is stretched spectrally and temporally to several tens of picoseconds using a pair of diffraction gratings before sent to pulse selection and amplification in gain medium. This technique is called chirped pulse amplification (CPA) and it reduces the peak intensity of the seed pulse to avoid damage to the gain medium through self-focusing and to avoid gain saturation that prevents further amplification. The amplifier uses a cryogenically cooled (-180°C) gain medium Ti:sapphire single crystal that is optically pumped to achieve population inversion using two external pump laser diodes (Photonics Industries) each with pulse duration 20 ns (quasi-CW), power 35 W, wavelength 532 nm, and repetition rate 30 kHz (tunable up to 300 kHz).

Regenerative amplifier cavity – The seed polarization is initially perpendicular to the plane of incidence until it passes through an entrance Pockel's cell (PC1) to rotate the

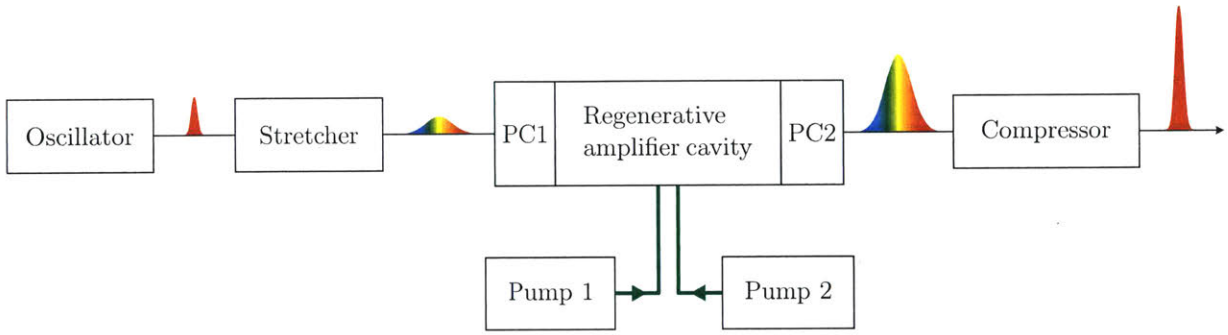

Figure 2.2: Optical layout inside Wyvern laser amplifier.

polarization by $\pi/2$ when activated. The Ti:sapphire crystal is cut at Brewster angle so that a seed pulse that is polarized along the plane of incidence gets trapped in the cavity and amplified. After six to ten passes the seed pulse is amplified by a factor of 10^6, and an exit Pockel's cell (PC2) is activated to rotate the polarization by $\pi/2$ so that the amplified pulse gets reflected from the Brewster's cut surface of the Ti:sapphire crystal and leaves the cavity. The timing of PC1 and PC2 are synchronized with the external laser diodes at 30 kHz, with 80 MHz clock from the oscillator, such that in the time span of 33 μs only one seed pulse is trapped and amplified.

After exiting the cavity, the amplified pulse is compressed spectrally and temporally using (effectively) a pair of gratings to achieve short pulse duration and very high peak intensity. The Wyvern amplifier output produces pulse duration 50 fs, energy 400 μJ (12 W at best), center wavelength 790 nm, and repetition rate 30 kHz. The laser beam is split by a thin polarizing beam splitter: (i) 230 μJ (7 W) to pump an optical parametric amplifier, and (ii) 170 μJ is directed toward white light continuum generation (3-5 μJ) where the excess energy is sent to a beam dumper.

2.1.3. Optical parametric amplifier

An optical parametric amplifier (OPA) is an optical setup that converts the laser fundamental wavelength into variable wavelengths through parametric amplification process. The principle operation of OPA is based on an optical parametric generation process $\omega_0 = \omega_s + \omega_i$ where one photon of frequency ω_0 (fundamental) is converted into

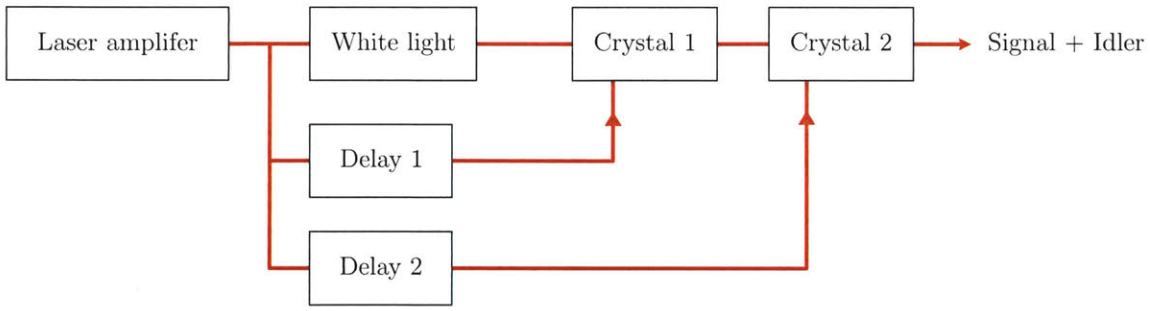

Figure 2.3: Optical layout inside optical parametric amplifier (OPA).

two photons of frequencies ω_s (signal) and ω_i (idler). The output frequencies are varied by tuning the phase matching condition and time delay between pulses in a nonlinear crystal. In our experiment, we use OPA Palitra from Quantronix that allows tunable wavelengths of signal and idler between 1.1 μm – 2.5 μm. Longer wavelengths up to 20 μm can be generated inside the OPA through a difference frequency generation (DFG) $\omega_s - \omega_i$, while shorter wavelengths down to 550 nm can be generated outside the OPA through a second harmonic generation (SHG) $2\omega_s$ or $2\omega_i$.

The overview of this OPA is schematically drawn in **Fig 2.3** and briefly discussed as follows. An input laser beam at wavelength 790 nm and pulse energy 230 μJ is split into two beams. About 10% of this beam will be used for the first amplification stage and 90% for the second amplification stage.

In the first amplification stage, the 10% beam is further split into two beams. One beam is used to generate white light continuum in a sapphire glass and directed through a ZnSe substrate to pass only the infrared wing of the continuum and to stretch the beam spectrally and temporally (chirped). This infrared continuum contains the signal frequency component ω_s, and it will be used as a seed pulse. The other beam of frequency ω_0 is directed to a delay stage and used as the pump pulse. The two beams meet at the first nonlinear crystal (Crystal 1) where the optical parametric generation $\omega_0 = \omega_s + \omega_i$ occurs. The output signal and idler frequencies can be tuned by varying the pump pulse time delay (Delay 1) to pick a particular frequency component ω_s from the seed pulse and by rotating

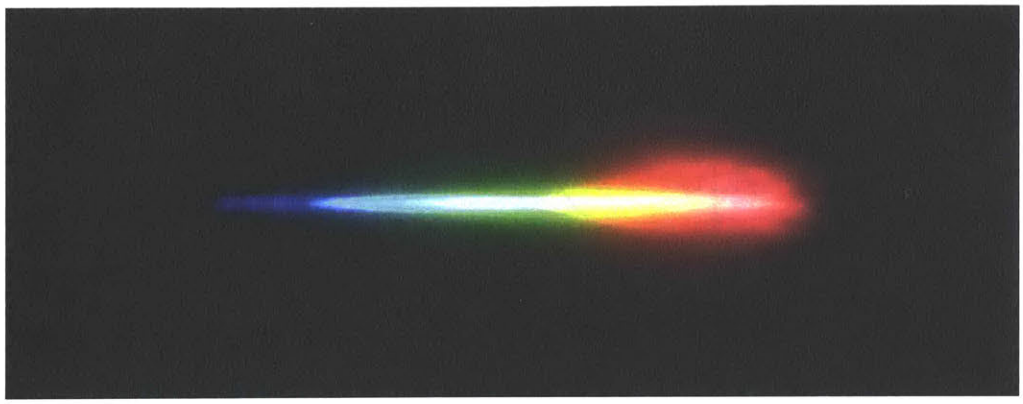

Figure 2.4: Real image of white light continuum generated in our setup.

the crystal optical axis to achieve a phase matching condition. The first amplification stage typically produces total pulse energy of 1 μJ (signal and idler).

In the second amplification stage, the amplified beam is directed to the second nonlinear crystal (Crystal 2) and meets the 90% pump beam. Similarly, the amplification efficiency is tuned by varying the second pump delay (Delay 2) and by rotating the crystal axis. This OPA is capable of producing total output energy of 45 μJ (signal + idler) with efficiency of 20% when the idler wavelength is set to 2.1 μm. The output of this OPA is used as the pump pulse in transient absorption setup because it can provide a tunable pump wavelength at high peak intensity.

2.1.4. White light continuum

White light continuum generation is a nonlinear optical process that converts laser pulses with narrow spectral bandwidth into pulses with very broad spectral bandwidth. For instance, in our setup we use a near infrared laser pulse that is focused into a transparent nonlinear medium to generate a visible white beam when projected on the screen **(Fig 2.4)**. This phenomenon was first observed by R. Alfano and S. Shapiro in 1970 [21]. Such a spectral broadening is driven by the nonlinear effects of self-phase modulation (SPM). This results from the Kerr nonlinearity of materials that also gives rise to Kerr self-focusing. We discuss this briefly as follows. Laser pulses with a gaussian intensity time profile is given by

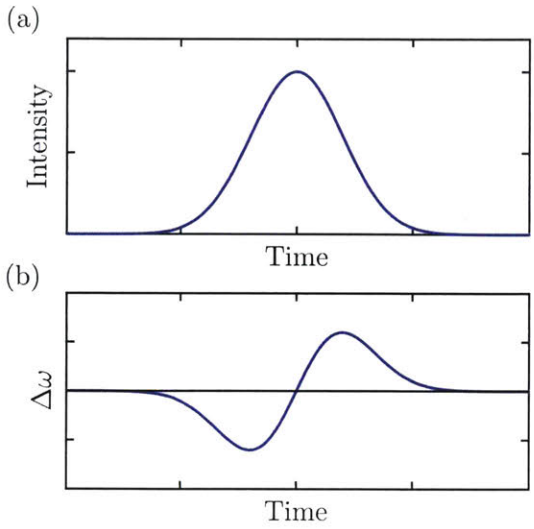

Figure 2.5: (a) Laser pulse with a gaussian temporal profile. **(b)** Frequency shift due to self-phase modulation after passing through a transparent nonlinear medium.

$$I(t) = I_0 \exp\left(-\frac{t^2}{\tau^2}\right) \tag{2.1}$$

where I_0 is the peak intensity and τ is the $1/e$ pulse duration **(Fig 2.5a)**. At high intensity, laser pulses that are traveling inside a medium can induce a refractive index change

$$n(I) = n_0 + n_2 I \tag{2.2}$$

where n_0 is the linear refractive index and n_2 is the nonlinear refractive index due to $\chi^{(3)}$ nonlinearity of the medium. The electric field of an incident laser pulse propagating in vacuum in $\hat{z}$ direction can be expressed as $\mathcal{E}(t) = \mathcal{E}_0 \cos(kz - \omega t)$. The time-varying laser intensity results in a time-varying refractive index of material $n(t)$, leading to a phase shift of the pulse's electric field

$$\phi(t) = \omega_0 t - kz = \omega_0 t - \frac{2\pi n(t)}{\lambda_0} L \tag{2.3}$$

where ω_0 and λ_0 are the carrier frequency and vacuum wavelength of the pulse, and L is the distance the pulse has traveled. The time-varying phase shift results in a time-varying frequency shift of the pulse **(Fig 2.5b)**, and the instantaneous frequency is given by

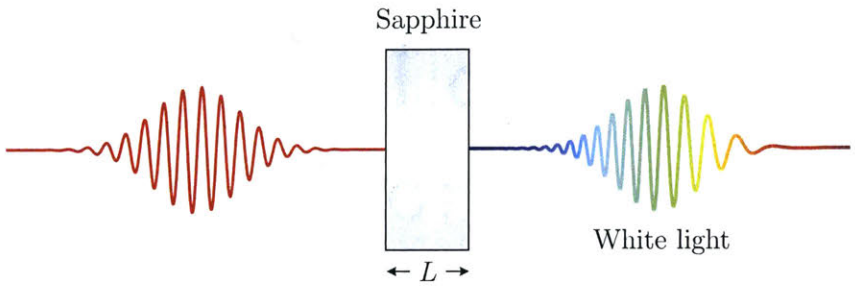

Figure 2.6: Incoming near IR laser pulse undergoes a self-phase modulation inside a sapphire glass, resulting in an outgoing white light continuum with a linear chirp.

$$\omega(t) = \frac{d\phi(t)}{dt} = \omega_0 + \left(\frac{4\pi L n_2 I_0}{\lambda_0 \tau^2}\right) t \exp\left(-\frac{t^2}{\tau^2}\right) \tag{2.4}$$

We can analyze the frequency shifts in three different time segments. The leading edge of the pulse shifts to lower frequencies (red-shifted), the trailing edge shifts to higher frequencies (blue-shifted), while the center exhibits no frequency shift. Although the carrier frequency $\omega(t)$ varies in time, the envelope temporal profile is effectively unchanged. Thus the spectral broadening maintains the incident pulse duration. However, the effect of group velocity dispersion through a transparent medium still occurs. In medium with normal dispersion, the red leading edge of the pulse travels with a faster group velocity, while the blue trailing edge with a slower group velocity. This effect spreads the frequency components temporally, an effect known as *chirp*, which can be as wide as 1 picosecond for wavelength range of 500-700 nm **(Fig 2.6)**. Nevertheless, the individual packets of frequency components still maintain the femtosecond pulse duration of the incident pulse, which is an important criterion for ultrafast transient absorption experiment.

In the above discussion, we have shown that self-phase modulation in the time domain can result in a white light continuum generation. Meanwhile, self-phase modulation in the spatial domain can also result in a distinct appearance of the white light pattern on the screen. The continuum appears as a round white disk surrounded by a concentric rainbow-like pattern **(Fig 2.7a-d)**. This is called a *conical emission* and it exhibits a large divergence angle. This is similar to the Kerr self-focusing effect except now we have multiple different wavelengths in the continuum.

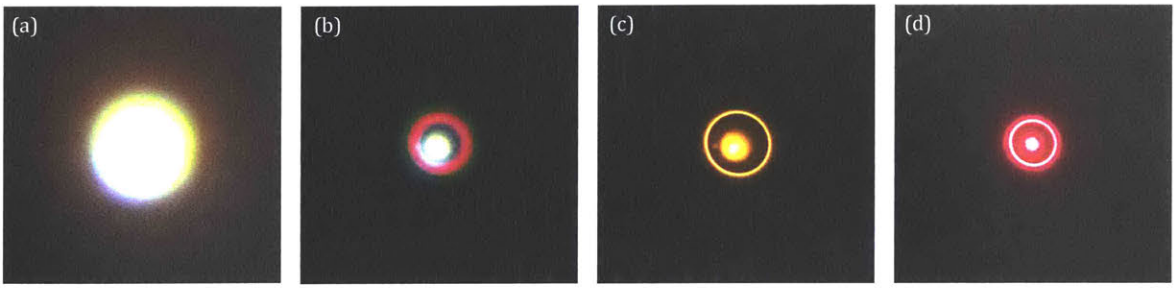

Figure 2.7: Capturing the conical emission feature. **(a)** Full intensity white light continuum. **(b)** Reduced intensity white light continuum, showing the rainbow-like pattern due to conical emission. **(c)** Orange color component after using 590 nm band pass filter. **(d)** Red color component after using 660 nm band pass filter.

2.2. Data analysis

Throughout our analysis, we used the proper definitions of reflectance R, transmittance T and absorptance α, which respectively means the fractions of incident electromagnetic power that is reflected, transmitted and absorbed at the monolayer interface (between vacuum and substrate). This is in contrast to reflectivity and transmittivity, which are technically only valid for semi-infinite system. We also used more familiar names such as absorbance and absorption to mean, quantitatively, the absorptance α of monolayer TMDs.

Pump-probe experiments detect small changes in probe reflectance (or transmittance) that is induced by pump excitation. This gives the differential reflectance $\Delta R/R$ as a function of energy and time delay, from which we can obtain the transient reflectance, $R(t) = R_0(1 + \Delta R(t)/R_0)$, where R_0 is the reflectance of the system in equilibrium. In fact, the absorptance α (or the induced absorptance $\Delta\alpha$) is what we really want (as shown in the main text) because it provides the explicit information about the optical transition matrix element of the system. The absorptance and the reflectance are related through the complex dielectric function $\tilde{\epsilon}$. This relation can be derived using Maxwell equations shown in section 2.2.2. We obtain $\tilde{\epsilon}(\omega, t)$ by fitting $R(\omega, t)$ using a Kramers-Kronig (KK) constrained variational analysis [22] shown in Section 2.2.1. Finally, we construct $\alpha(\omega, t)$ by repeating this procedure at different time delays. The details of the above procedure are described as follows, in the case for monolayer TMD WS_2.

2.2.1. Kramers-Kronig analysis

First, we want to find the relation between the complex dielectric function and the optical properties such as reflectance, transmittance and absorptance by using Maxwell's equations. It is important to include the substrate influence on electromagnetic radiation especially for atomically-thin materials. Here, the current density in a monolayer WS_2 sample is described by a delta function, $j_x = \tilde{\sigma}(\omega)\delta(z)E_x$ where $\tilde{\sigma}$ is the complex conductivity and E_x is the x-component of the probe electric field (along the sample's surface). By substituting this into Maxwell's equations and using the appropriate boundary conditions between the monolayer and the substrate, we can obtain the reflectance as

$$R(\omega) = \frac{(1 - n_s - \frac{\omega d}{c}\epsilon_2)^2 + (\frac{\omega d}{c}(\epsilon_1 - 1))^2}{(1 + n_s + \frac{\omega d}{c}\epsilon_2)^2 + (\frac{\omega d}{c}(\epsilon_1 - 1))^2} \tag{2.5}$$

and the transmittance as

$$T(\omega) = \frac{4n_s}{(1 + n_s + \frac{\omega d}{c}\epsilon_2)^2 + (\frac{\omega d}{c}(\epsilon_1 - 1))^2} \tag{2.6}$$

where n_s is the substrate's refractive index (1.7675 for sapphire at photon energy of 2.07 eV), d is the effective thickness of the monolayer (0.67 nm), ϵ_1 and ϵ_2 are the real and imaginary parts of the dielectric function, respectively. Here, the 2D dielectric function is expressed as

$$\tilde{\epsilon}(\omega) = 1 + \frac{4\pi i\tilde{\sigma}/d}{\omega} \tag{2.7}$$

Meanwhile, the absorptance can be expressed as

$$\alpha(\omega) = \frac{4\frac{\omega d}{c}\epsilon_2}{(1 + n_s + \frac{\omega d}{c}\epsilon_2)^2 + (\frac{\omega d}{c}(\epsilon_1 - 1))^2} \tag{2.8}$$

These expressions are exact, and they are valid for any monolayer materials on a dielectric substrate. We find that the presence of the substrate significantly influences the optical properties of the monolayer WS_2 above it. As compared to an isolated monolayer WS_2, the reflectance is enhanced, while both the transmittance and the absorptance are reduced. In graphene, the above expressions can be further simplified because the real part

of its dielectric function is featureless in the visible spectrum ($\epsilon_1 \sim 1$, negligible σ_2). This is, however, not the case for monolayer WS_2, and we must include both the real and imaginary parts of the dielectric function to obtain accurate results. In situation where none of the equilibrium absorptance, reflectance or transmittance spectrum is available, the pump-induced absorptance $\Delta\alpha$ can still be estimated from the measured $\Delta R/R$ or $\Delta T/T$ through the following expression

$$\frac{\Delta R}{R} = \left[\left(\frac{n_s + 1}{n_s - 1}\right) + \frac{n_s}{(n_s - 1)^2}\frac{(\gamma_1^2 + \gamma_2^2)}{\gamma_2}\right]\Delta\alpha \tag{2.9}$$

$$\frac{\Delta T}{T} = -\left[\left(\frac{n_s + 1}{2}\right) + \frac{(\gamma_1^2 + \gamma_2^2)}{4\gamma_2}\right]\Delta\alpha \tag{2.10}$$

where ΔR and ΔT are the pump-induced changes of the probe reflectance R and transmittance T, n_s is the refractive index of the substrate, $\gamma_1 = \omega d(\epsilon_1 - 1)/c$, and $\gamma_2 = \omega d\epsilon_2/c$. In situation where γ_1^2 and γ_2^2 are small, such as graphene and few other TMDs, only the first term in the bracket needs be considered.

In our analysis, we used the equilibrium absorptance α of monolayer WS_2 measured using differential reflectance microscopy. The absorptance spectrum contains peaks from the A exciton at 2.0 eV. The equilibrium reflectance R_0 can then be constructed from α by finding the appropriate complex dielectric function $\tilde{\epsilon}$ as expressed in Equations 2.7 & 2.8. To do this, we implemented a Kramers-Kronig (KK) constrained variational analysis [22] to extract $\tilde{\epsilon}$ from the measured α in thin-film approximation. Here, the total dielectric function is constructed by many Drude-Lorentz oscillators, which are anchored at equidistant energy spacing, in the following form

$$\tilde{\epsilon}(\omega) = \epsilon_\infty + \sum_{k=1}^{N} \frac{\omega_{p,k}^2}{\omega_{0,k}^2 - \omega^2 - i\omega\gamma_k} \tag{2.11}$$

In our calculations, we used $N = 40$ oscillators with a fixed linewidth of $\gamma_k = 50$ meV spanning the energy range of $1.77\,eV \leq \omega_{0,k} \leq 2.40\,eV$, and we found that these parameters can fit α spectrum very well. We can then construct R_0 spectrum by using $\tilde{\epsilon}$ obtained from the above analysis.

The transient absorptance spectra $\alpha(t)$ can be obtained by performing similar (KK) analysis. This time we inferred the absorptance from the reflectance at different time delays: $R(t) = R_0(1 + \Delta R(t)/R_0)$, where the differential reflectance $\Delta R(t)/R_0$ is measured directly from the experiments.

2.2.2. Maxwell's equations for monolayer sample

In this section, we provide a full derivation from Maxwell's equations in order to obtain the exact solutions of reflectance $R(\omega)$, transmittance $T(\omega)$ and absorptance spectra $\alpha(\omega)$ for any monolayer materials on a substrate. Readers who are interested in this section should also refer to the original articles by L. A. Falkovsky [23] and T. Stauber [24] in the study of graphene. Here, we express the solutions in terms of the complex dielectric function $\tilde{\epsilon}(\omega)$ or conductivity $\tilde{\sigma}(\omega)$ for Kramers-Kronig analysis shown in previous section.

The electromagnetic wave equation at frequency ω, inside a medium with a dielectric constant ϵ and a current density $\mathbf{j}$, can be expressed as

$$\nabla(\nabla \cdot \mathbf{E}) - \nabla^2 \mathbf{E} = \epsilon \frac{\omega^2}{c^2} \mathbf{E} + \frac{4\pi i \omega}{c^2} \mathbf{j} \tag{2.12}$$

We consider a situation **(Fig 2.8)** where the monolayer medium spreads on the xy plane with a current density $j_x = \tilde{\sigma}(\omega)\delta(z)E_x(x,t)$ that is driven by a propagating electric field on the xz plane of the form $\mathbf{E} = (E_{0x}, 0, E_{0z})e^{i(\mathbf{k}\cdot\mathbf{r}-\omega t)}$. By evaluating the partial derivatives of $\mathbf{E}$, the two components of the wave equation can be expressed as

$$ik_x \frac{\partial E_z}{\partial z} - \frac{\partial^2 E_x}{\partial z^2} - \epsilon \frac{\omega^2}{c^2} E_x = \frac{4\pi i \omega}{c^2} j_x \tag{2.13}$$

$$ik_x \frac{\partial E_x}{\partial z} + \left(k_x^2 - \epsilon \frac{\omega^2}{c^2}\right) E_z = 0 \tag{2.14}$$

where we have used $\partial/\partial x \rightarrow ik_x$ because the law of refraction requires that k_x is conserved, while k_z is not. Boundary conditions for the tangential and normal components of the field (red arrows) yield

$$E_x = (E_i - E_r)\cos\theta_i = E_t \cos\theta_t \tag{2.15}$$

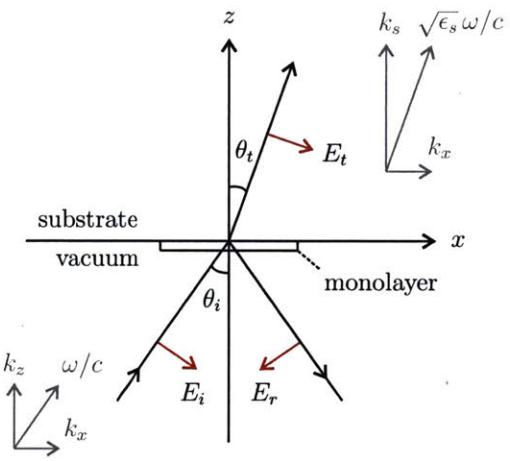

Figure 2.8: Schematic of the plane of incidence

$$\epsilon_s E_z|_{z=0^+} - E_z|_{z=0^-} = 4\pi \int_{0^-}^{0^+} \rho(z)dz \tag{2.16}$$

where we have used $\epsilon = \epsilon_s$ for the substrate and $\epsilon = 1$ for the vacuum. The charge density ρ and the current density j_x must satisfy the continuity equation $\partial\rho/\partial t + \nabla \cdot \mathbf{j} = 0$. Since they are driven by the same external field $E_x(x,t)$, we can then obtain a relation

$$\rho = j_x k_x/\omega \tag{2.17}$$

Equation 2.16 can now be evaluated by substituting E_z from Equation 2.14 and ρ from Equation 2.17, which yields

$$\frac{\epsilon_s}{k_s^2}\frac{\partial E_x}{\partial z^+} - \frac{1}{k_z^2}\frac{\partial E_x}{\partial z^-} = \frac{4\pi\tilde{\sigma}}{i\omega}E_x|_{z=0} \tag{2.18}$$

where the relations between k_x, k_z and k_s are shown in **Fig 2.8**. Note that the fields at the boundary are $E_x|_{z^+} = E_t e^{i(k_x x + k_s z)}\cos\theta_t$ and $E_x|_{z^-} = \left(E_i e^{i\mathbf{k}\cdot\mathbf{r}} - E_r e^{-i\mathbf{k}\cdot\mathbf{r}}\right)\cos\theta_i$. Substituting these will yield

$$\left(\frac{\epsilon_s}{k_s} + \frac{4\pi\tilde{\sigma}}{\omega}\right)E_t\cos\theta_t = \frac{1}{k_z}(E_i + E_r)\cos\theta_i \tag{2.19}$$

$$(E_i - E_r)\cos\theta_i = E_t\cos\theta_t \tag{2.20}$$

These are the two equations that will be used to obtain the reflectance, transmittivity, and absorptance of the monolayer. For convenience, we have moved Equation 2.15 into 2.20.

At normal incidence, $k_s = \sqrt{\epsilon_s}\omega/c$ and $k_z = \omega/c$, hence the coefficients of amplitude reflection and transmission [25] can be simplified into

$$-r = -\frac{E_r}{E_i} = \frac{1 - n_s - \frac{4\pi\tilde{\sigma}}{c}}{1 + n_s + \frac{4\pi\tilde{\sigma}}{c}} \tag{2.21}$$

$$t = \frac{E_t}{E_i} = \frac{2}{1 + n_s + \frac{4\pi\tilde{\sigma}}{c}} \tag{2.22}$$

where $\tilde{\sigma} = \sigma_1 + i\sigma_2$ is the complex conductivity of the monolayer, and we have used $\sqrt{\epsilon_s} = n_s$ for an insulating substrate. Finally, we can obtain the reflectance R and the transmittance T, as well as the absorptance α through the energy conservation $|r|^2 + n_s|t|^2 + \alpha = 1$ [25],

$$R = |r|^2 = \frac{\left(1 - n_s - \frac{4\pi\sigma_1}{c}\right)^2 + \left(\frac{4\pi\sigma_2}{c}\right)^2}{\left(1 + n_s + \frac{4\pi\sigma_1}{c}\right)^2 + \left(\frac{4\pi\sigma_2}{c}\right)^2} \tag{2.23}$$

$$T = n_s|t|^2 = \frac{4n_s}{\left(1 + n_s + \frac{4\pi\sigma_1}{c}\right)^2 + \left(\frac{4\pi\sigma_2}{c}\right)^2} \tag{2.24}$$

$$\alpha = \frac{4\left(\frac{4\pi\sigma_1}{c}\right)}{\left(1 + n_s + \frac{4\pi\sigma_1}{c}\right)^2 + \left(\frac{4\pi\sigma_2}{c}\right)^2} \tag{2.25}$$

The obtained $\alpha(\omega)$ is the absorptance of a monolayer medium deposited on an insulating substrate. The whole derivation already accounts for the out-of-phase back-reflected electric field that reduces the light intensity impinging on the monolayer. The above solutions can be expressed in terms of $\tilde{\epsilon}$ instead of $\tilde{\sigma}$ using the following relation

$$\tilde{\epsilon} = 1 + \frac{4\pi i\tilde{\sigma}/d}{\omega} \tag{2.26}$$

Note that $\tilde{\sigma}$ has different units in 2D (here) and in 3D; hence we keep the dielectric function dimensionless by introducing the monolayer thickness d. In order to convert these gaussian-unit equations into the SI-unit, we can use $4\pi \rightarrow 1/\epsilon_0$ where $\epsilon_0 (= 8.85 \times 10^{-12}$ F/m) is the vacuum permittivity.

Chapter 3

Intervalley biexcitons in monolayer MoS_2

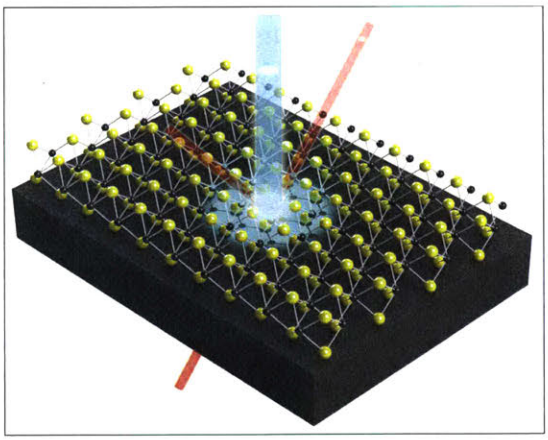

Contents[1]

[1] The work presented in this chapter is published in the following journal:
Edbert J. Sie, Alex J. Frenzel, Yi-Hsien Lee, Jing Kong, Nuh Gedik
***Physical Review B* 92**, 125417 (2015)

Interactions between two excitons can result in the formation of bound quasiparticles, known as biexcitons. Their properties are determined by the constituent excitons, with orbital and spin states resembling those of atoms. Monolayer transition metal dichalcogenides (TMDs) present a unique system where excitons acquire a new degree of freedom, the valley pseudospin, from which a novel *intervalley* biexciton can be created. These biexcitons comprise two excitons from different valleys, which are distinct from biexcitons in conventional semiconductors and have no direct analogue in atomic and molecular systems. However, their valley properties are not accessible to traditional transport and optical measurements. Here, we report the observation of intervalley biexcitons in the monolayer TMD MoS_2 using ultrafast pump-probe spectroscopy [26]. By applying broadband probe pulses with different helicities, we identify two species of intervalley biexcitons with large binding energies of 60 meV and 40 meV. In addition, we also reveal effects beyond biexcitonic pairwise interactions in which the exciton energy redshifts at increasing exciton densities, indicating the presence of many-body interactions among them.

3.1. Intervalley biexcitons

Monolayer transition metal dichalcogenides (TMDs) comprise a new class of atomically thin semiconducting crystals in which electrons exhibit strong spin-valley coupling that results in novel valleytronic properties when interrogated with circularly polarized light [15]. These include valley-selective photoexcitation [18-20], valley Hall effect [27], valley-tunable magnetic moment [28], and valley-selective optical Stark effect [29, 30]. Unlike traditional semiconductors, the Coulomb interaction in monolayer TMDs is unusually strong because screening is greatly suppressed and spatial overlap of the interaction is much larger [6]. This enhances the stability of a variety of excitonic quasiparticles with extremely large binding energies, including excitons [31, 32], trions [33-35], and exciton-trion complexes [36].

In addition to excitons and trions, monolayer TMDs should also host biexcitons, van der Waals quasiparticles formed from two neutral excitons bound by residual Coulomb fields. Moreover, the unique spin-valley coupling of these electrons, which also behave as

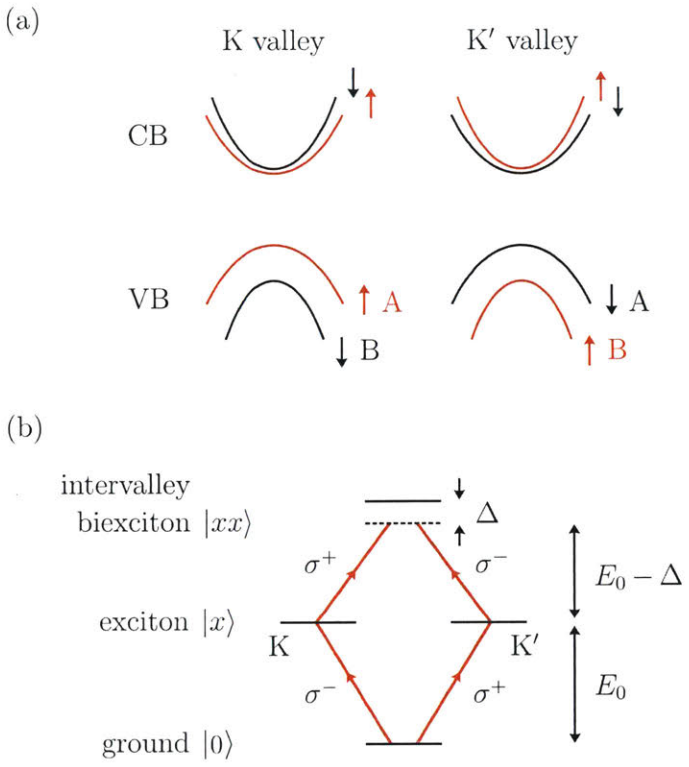

Figure 3.1: (a) Schematic band structure of the two valleys. **(b)** Optical transitions to intervalley biexciton state.

massive Dirac fermions at two different valleys **(Fig 3.1a)**, offers an ideal system to form unique intervalley biexcitons that have two-dimensional positronium-molecular-like structure. Apart from the large binding energies, they are also expected to show novel properties such as entanglement between the pair of valley pseudospins. Thorough investigation of these properties is crucial to assess their potential use in applications. Advanced experimental probes are needed to uncover these unique quasiparticles that cannot be accessed by more conventional techniques.

Transient absorption spectroscopy is ideally suited to access intervalley biexciton states via two-step excitation **(Fig 3.1b)**. In this experiment, an ultrashort laser pulse is split into two portions: the first pulse (pump) is used to create a population of excitons, $|0\rangle \rightarrow |x\rangle$, and the second pulse (probe) is used to induce a second transition to form biexcitons, $|x\rangle \rightarrow |xx\rangle$. In monolayer TMDs, there are two degenerate valleys (K and K') where different excitons can be created using left (σ^-) and right (σ^+) circularly polarized

light [15, 18-20]. In order to form intervalley biexcitons, we used a succession of pump and probe pulses with opposite helicities. The biexcitons are revealed as a pump-induced absorption of the probe pulse at energy slightly below the primary exciton absorption peaks.

Here, we show that there are two intervalley biexciton species in monolayer TMD MoS_2, which we identify as AA biexcitons and AB heterobiexcitons. We measure the binding energies of these biexcitons to be 60 meV and 40 meV, respectively. Experiments using excess pump photon energy reveal the stability of the biexcitons at high temperatures. We also investigate the effect of high excitation densities on the excitons, which shows the presence of many-body effects in monolayer MoS_2.

3.2. Experimental methods

In our experiments, we used a Ti:sapphire regenerative amplifier producing laser pulses at 30 kHz, with center wavelength 785 nm and duration 50 fs FWHM. Each pulse was split into two arms. For the pump arm, the pulses were frequency-converted using an optical parametric amplifier (for resonant excitation) or a second-harmonic crystal (for nonresonant excitation), and then chopped at 7.5 kHz. For the probe arm, the pulses were sent through a delay stage and a white-light continuum generator ($h\nu$ = 1.78-2.48 eV, chirp-corrected). The two beams were focused onto the sample with 450 μm (pump) and 150 μm (probe) FWHM diameters. The probe beam was reflected or transmitted from the sample to a monochromator with FWHM resolution 1 nm and a photodiode for detection. Lock-in detection at 7.5 kHz allowed measurement of fractional changes in reflectance $\Delta R/R$ or transmittance $\Delta T/T$ as small as 10^{-4}. By scanning the grating and the delay stage, we were able to measure $\Delta R/R$ or $\Delta T/T$ as a function of energy and time delay Δt, from which the induced absorptance α was obtained using Kramers-Kronig analysis (Chapter 2). The pump fluence was varied by a combination of a half-wave plate and polarizer, allowing us to tune the exciton excitation density. High-quality monolayers of MoS_2 were CVD-grown on a sapphire substrate [10, 11] and mounted inside a cold-finger cryostat with temperature of 10 K or all measurements in this study.

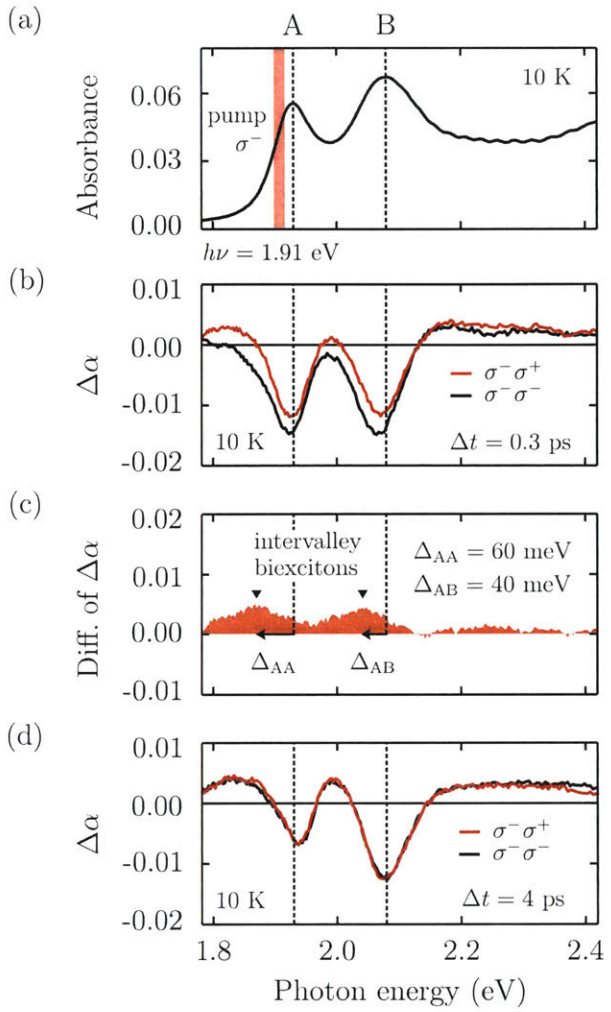

Figure 3.2: (a) Measured equilibrium absorbance of monolayer MoS_2. **(b)** Pump-induced absorption of the probe pulses at $\Delta t = 0.3$ ps using different helicities. **(c)** The difference between the two $\Delta\alpha$ spectra shown in (b), where the biexciton binding energies are obtained. **(d)** $\Delta\alpha$ spectra at $\Delta t = 4$ ps.

3.3. Experimental results & discussions

The equilibrium absorption spectrum of monolayer MoS_2, measured using differential reflectance microscopy, consists of two exciton resonances ($E_A = 1.93$ eV and $E_B = 2.08$ eV) and a background from higher-energy states [31] **(Fig 3.2a)**. To create a population of excitons at the K valley, we used σ^- pump pulses with photon energy tuned near the A exciton resonance ($h\nu = 1.91$ eV) and fluence 5 μJ cm^{-2}. Further excitation to the intervalley biexciton state can be detected from induced absorption ($\Delta\alpha > 0$) of σ^+

probe pulses. In an ideal system with negligible scattering, one would also expect to see optical bleaching ($\Delta\alpha < 0$) at the A exciton transition using σ^- probe pulses and no bleaching anywhere using σ^+ probe pulses. **Fig 3.2b** shows a pair of $\Delta\alpha$ spectra measured using broadband probe pulses with helicities σ^- (black) and σ^+ (red) at $\Delta t = 0.3$ ps. This time delay was chosen to avoid contaminating effects of coherent light-matter interaction [29, 30]. In contrast to what is expected, we observed strong bleaching peaks not only at A but also at B exciton transitions, and strikingly, these two peaks were present in both spectra measured using different helicities [37].

3.3.1. Intravalley & intervalley scattering

The unexpected bleaching of the B exciton transition can only originate from electron state filling in the conduction band. This is because the pump photon energy is insufficient to excite holes to form a B exciton, and hole scattering between the A and B bands is very unlikely due to the large energy splitting (150 meV). Meanwhile, the photoexcited electron spin-up state (for A exciton) at the K valley can exhibit an *intravalley* spin reversal to occupy the electron spin-down state (for B exciton). This process can be mediated by flexural phonons [38], and it can occur during the pump pulse duration (Supplementary Section 3.3.1).

Intravalley electron spin reversal – In order to further understand the bleaching of B exciton transition, we note that at the K valley the electron states in the conduction band are split by the spin-orbit coupling into two spin states, where the electron spin-up state (for A exciton) is 3 meV lower in energy than the electron spin-down state (for B exciton) [2, 4, 39, 40]. These two states preserve the good spin quantum numbers (out of plane) due to the σ_h mirror symmetry of the lattice. Resonant excitation of the A exciton using σ^- pump pulses only populates the electron spin-up state at K valley **(Fig 3.1a)**, and should in principle not bleach the B exciton transition. Hence, the observed bleaching of B exciton can only be explained by the electron spin reversal in the conduction band that immediately occurs during the pump pulse duration (160 fs). In this flexible material, intravalley electron spin reversal can be mediated by flexural phonons in the realm of Elliott-Yafet spin-flip mechanism [38]. Spin-flip transition is allowed in the scattering via

long-wavelength in-plane optical phonon and out-of-plane acoustic phonon, for which the respective deformation potentials are even and odd with respect to mirror symmetry. Because of the small spin-splitting in the conduction band, the strong spin-orbit coupling and the flexible lattice structure, the spin lifetime could be as short as 50 fs for suspended monolayer MoS_2 at room temperature. Supporting the membrane with sapphire substrate at 10 K can in principle prolong the spin lifetime [38] but substrate roughness, domain boundaries and impurities could conversely increase the rate of carrier collisions that will enhance the spin-reversal scattering rate. The fast electron spin reversal could thus explain the B exciton bleaching shown in **Fig 3.2b**.

On the other hand, the bleaching peaks that are observed using the opposite probe helicity can be explained by *intervalley* scattering, which is expected to be very fast due to electron-hole exchange interaction in this material [37, 41, 42]. In particular, valley excitons with finite in-plane momentum can have exchange interaction that generates an in-plane effective magnetic field, around which the exciton pseudospin precesses from K to K' valley. Calculations show that such valley depolarization can be as fast as tens to hundreds of fs [41], consistent with our observation.

3.3.2. Signature of intervalley biexcitons

Comparison of the two spectra in **Fig 3.2b** shows that the red curve gains an appreciable offset in certain spectral ranges with respect to the black curve that, according to the pump-probe scheme in **Fig 3.1b**, can be attributed to induced absorption to intervalley biexciton states. To isolate the biexciton contribution, we evaluate the difference between the two spectra **(Fig 3.2c)** from which we extract the biexciton binding energies (Δ_{xx}). We find peak energies of $\Delta_{AA} = 60$ meV and $\Delta_{AB} = 40$ meV, consistent with recently estimated values [37, 43]. Since we only excited the A excitons at resonant excitation, we expect the biexcitons to contain at least one A exciton. Thus, by the proximity of the biexciton peaks in **Fig 3.2c** to the exciton resonances, we deduce that the former is comprised of two A excitons (AA biexcitons), while the latter consists of one A and one B exciton (AB heterobiexcitons). The intervalley nature of these biexcitons is guaranteed by our measurement protocol, where we used pump and probe pulses with opposite helicities.

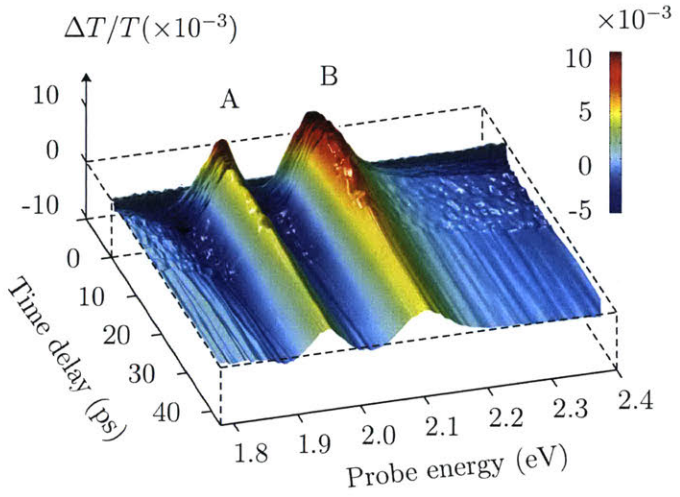

Figure 3.3: $\Delta T/T$ spectra as a function of Δt after pump pulse excitation at $h\nu = 3.16$ eV.

Additional contributions apart from the intervalley biexcitons are eliminated by taking the difference in Δα spectra as shown in **Fig 3.2c**. At later time delays, both $\Delta\alpha$ spectra become nearly identical **(Fig 3.2d)** because intervalley scattering establishes balance between the exciton populations at the two valleys. Biexciton formation can then be induced from these excitons via absorption of probe pulses with either polarization (σ^- and σ^+).

We measured biexciton binding energies to be greater than the thermal energy at room temperature, $\Delta_{xx} > 25$ meV. This is expected because the excitons in monolayer MoS_2 have large binding energies (E_b), with measured values reported from 440 meV [32] to 570 meV [31]. Despite this variation in the reported values, the obtained binding energies are consistent with theoretical models [44, 45] that predict $\Delta_{AA} = (0.13 - 0.23)\, E_b$ in monolayer MoS_2 [46]. The large biexciton binding energies share the same origin as those of the excitons where, in the 2D limit, quantum confinement and suppressed screening greatly enhance the Coulomb interaction in this system [6].

3.3.3. Time-resolved cooling process

We now turn to discuss the time evolution of biexciton formation upon photoexcitation using excess pump photon energy ($h\nu = 3.16$ eV) and exciton excitation density of 1.4×10^{12} cm^{-2}. In this section, we measured the differential transmittance

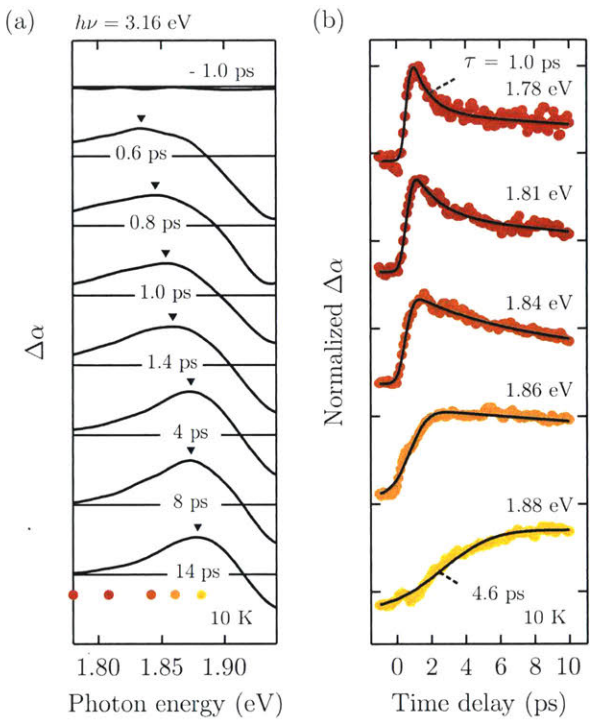

Figure 3.4: (a) $\Delta\alpha$ spectra at increasing time delays, showing the peak sharpening and the shifting to higher probing energy. **(b)** Time-traces of $\Delta\alpha$ at probe energies as indicated by the colored dots in (a).

$\Delta T/T$ as a function of probe photon energy and time delay **(Fig 3.3)**. We plot the corresponding $\Delta\alpha$ spectra at different time delays in **Fig 3.4a**, expanded around the A exciton resonance. The induced absorption peak exhibits a gradual shift in energy from 1.83 eV at 0.6 ps to 1.88 eV at 14 ps, which is accompanied by a peak sharpening. To elucidate this behavior we plot, in **Fig 3.4b**, the $\Delta\alpha$ time-traces (normalized) between energies 1.78–1.88 eV, as indicated by the colored dots in **Fig 3.4a**. We find that the decay at 1.78 eV is accompanied by a buildup at 1.88 eV. The latter value is consistent with the peak position of the biexciton signature measured in the near resonant excitation.

We interpret this observation as resulting from the exciton cooling process, where the energy distribution of the photoexcited excitons varies with the time delay, as depicted in **Fig 3.5**. In the first panel, we show the density of exciton states $D(E)$ surrounding the A exciton resonance. In our experiment, the non-resonant excitation by the pump pulse ($h\nu > E_A$) imparts an excess energy of $\delta E \sim 1$ eV per exciton. This leads to the immediate

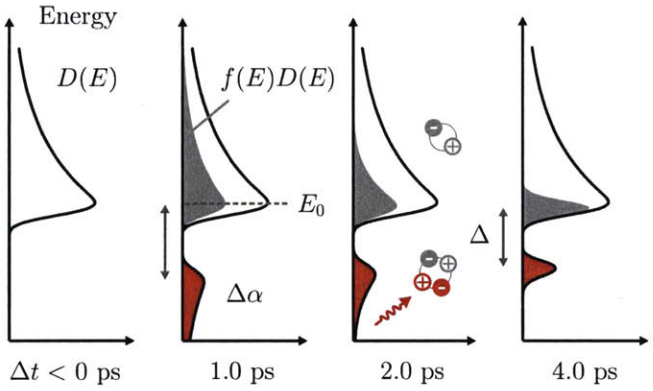

Figure 3.5: Time evolution of the exciton energy distribution (gray) and the corresponding biexciton induced absorption $\Delta\alpha$ (red) through the cooling process.

formation of a hot exciton gas ($T_e \sim 10^3$ K), where the population of highly energetic excitons $f(E)D(E)$ at $E > E_A$ becomes substantial. This is shown on the second panel of **Fig 3.5** (grey), including the associated $\Delta\alpha$ spectra (red). The biexciton energy can now be expressed as

$$E_{AA} = (E_A + \delta E)_{pump} + (E_A - \Delta - \delta E)_{probe} \tag{4.19}$$

where δE is the excess exciton energy whose distribution depends on T_e. Hence, we only need to create a probe exciton with energy lower than $E_A - \Delta$ to form a biexciton of energy E_{AA}. This explains the low-energy tail of $\Delta\alpha$ at $\Delta t \leq 1.4$ ps **(Fig 3.4a)**. Moreover, the presence of biexciton absorption at such an early relaxation stage of the hot exciton gas shows that they are stable at high temperatures. At later time delays (**Fig 3.5**, right panels), the highly energetic excitons gradually relax into the lowest state, via releasing energy to the lattice and the substrate, to form a cold exciton gas. During this process, the $\Delta\alpha$ spectral weight (red) at lower energy gradually climbs to higher energy, consistent with the observed dynamics in **Fig 3.4b** and the $\Delta\alpha$ peak shifting and sharpening in **Fig 3.4a**.

3.4. Conclusions

In conclusion, by using transient absorption spectroscopy we have observed intervalley biexcitons in monolayer MoS_2, measured their binding energies, and monitored their relaxation processes. Studying intervalley biexcitons could offer a new concept of

quasiparticles in solids where valley pseudospin states play significant roles, apart from the usual atom-like orbital and spin states. The large biexciton binding energies in this material offer a promising direction to search for higher-order bound excitons such as *triexcitons* and the elusive *quadexcitons* [47, 48] as well as their interplay with spin-valley degrees of freedom. We also found that, while two excitons can interact and form a biexciton, the interactions between *free* excitons in this system reveal a large energy red-shift that obeys a simple power-law behavior with density. This experimentally obtained relation between the energy shift and the density, as well as the obtained biexciton binding energies, should be used to aid future theoretical works and additional experiments in exploring many-body physics in atomically thin materials.

Chapter 4

Valley-selective optical Stark effect in monolayer WS_2

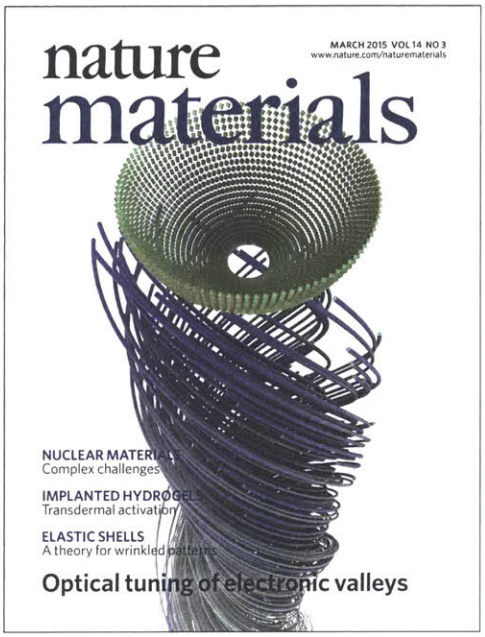

Contents[2]

[2] The work presented in this chapter is published in the following journal:
Edbert J. Sie, James W. McIver, Yi-Hsien Lee, Liang Fu, Jing Kong, Nuh Gedik
Nature Materials **14**, 290-294 (2015)

Breaking space-time symmetries in two-dimensional crystals (2D) can dramatically influence their macroscopic electronic properties. Monolayer transition-metal dichalcogenides (TMDs) are prime examples where the intrinsically broken crystal inversion symmetry permits the generation of valley-selective electron populations [15, 18-20], even though the two valleys are energetically degenerate, locked by time-reversal symmetry. Lifting the valley degeneracy in these materials is of great interest because it would allow for valley-specific band engineering and offer additional control in valleytronic applications. While applying a magnetic field should in principle accomplish this task, experiments to date have observed no valley-selective energy level shifts in fields accessible in the laboratory. Here we show the first direct evidence of lifted valley degeneracy in the monolayer TMD WS_2 [29]. By applying intense circularly polarized light, which breaks time-reversal symmetry, we demonstrate that the exciton level in each valley can be selectively tuned by as much as 18 meV via the optical Stark effect. These results offer a novel way to control valley degree of freedom, and may provide a means to realize new valley-selective Floquet topological phases [49-51] in 2D TMDs.

4.1. Optical Stark effect

The coherent interaction between light and matter offers a means to modify and control the energy level spectrum of a given electronic system. This interaction can be understood using what is known as Floquet theory [52], which states that a Hamiltonian periodic in time has quasistatic eigenstates that are evenly spaced in units of the photon driving energy. The simplest example of this is given by a two-level atomic system in the presence of monochromatic light, which can be fully described by the semi-classical Hamiltonian

$$\hat{H}(t) = \hat{H}_0 + \hat{p}\mathcal{E}(t) \tag{4.1}$$

where $\hat{H}_0$ is the equilibrium Hamiltonian describing a two-level atom with eigenstates $|a\rangle$ and $|b\rangle$, $\hat{p}$ is the electric dipole moment operator of the atom, and $\mathcal{E}(t) = \mathcal{E}_0 \cos 2\pi\nu t$ is the oscillating electric field of light with amplitude $\mathcal{E}_0$ and frequency ν. The perturbation term in the Hamiltonian contains a time-dependent factor ($\cos 2\pi\nu t$) that enables the coherent

absorption of light by $|a\rangle$ to form the photon-dressed state $|a + h\nu\rangle$, and the stimulated emission of light by $|b\rangle$ to form another photon-dressed state $|b - h\nu\rangle$, as shown in **Fig 4.1b**. Additional states $|a - h\nu\rangle$ and $|b + h\nu\rangle$, as well as higher order terms, also arise in this situation. This semi-classical description is consistent with the fully quantized approach.

The series of photon-dressed states formed in this way are called the Floquet states, which can hybridize with the equilibrium states $|a\rangle$ and $|b\rangle$ through the electric field term $\mathcal{E}$ in Equation 4.1. This hybridization often results in energy repulsion between the equilibrium and Floquet states, the physics of which is equivalent to the hybridization between two atomic orbitals by the Coulomb interaction to form the bonding and anti-bonding molecular orbitals in quantum chemistry. The interaction between the two states always results in a wider energy level separation, and the magnitude of the energy repulsion becomes more substantial if the states are energetically closer to each other. In our case, there are two such pairs of states shown in **Fig 4.1b** and **Fig 4.2a** denoted as $\{|a + h\nu\rangle, |b\rangle\}$ and $\{|a\rangle, |b - h\nu\rangle\}$ with identical energy difference of $\Delta = (E_b - E_a) - h\nu$. Through the simultaneous energy repulsion of these pairs, the optical transition between states $|a\rangle$ and $|b\rangle$ is shifted to a larger energy. This phenomenon is known as the optical Stark effect [53, 54], and the corresponding energy shift (ΔE) is given by

$$\Delta E = \frac{\mathcal{M}_{ab}^2 \langle \mathcal{E}^2 \rangle}{\Delta} \tag{4.2}$$

where $\mathcal{M}_{ab}$ is the polarization matrix element between $|a\rangle$ and $|b\rangle$, and $\langle \mathcal{E}^2 \rangle$ $(= \mathcal{E}_0^2/2)$ is the time-averaged value of the electric field squared, proportional to the light intensity. Owing to the tunability of this energy shift by changing either the light intensity or frequency, the optical Stark effect has been routinely employed in the study of atomic physics and to facilitate the cooling of atoms below the Doppler limit [55].

4.1.1. Semi-classical description

For the purpose of understanding the optical Stark effect in atoms, it is often sufficient to write down the semi-classical form of the Hamiltonian, in which light is

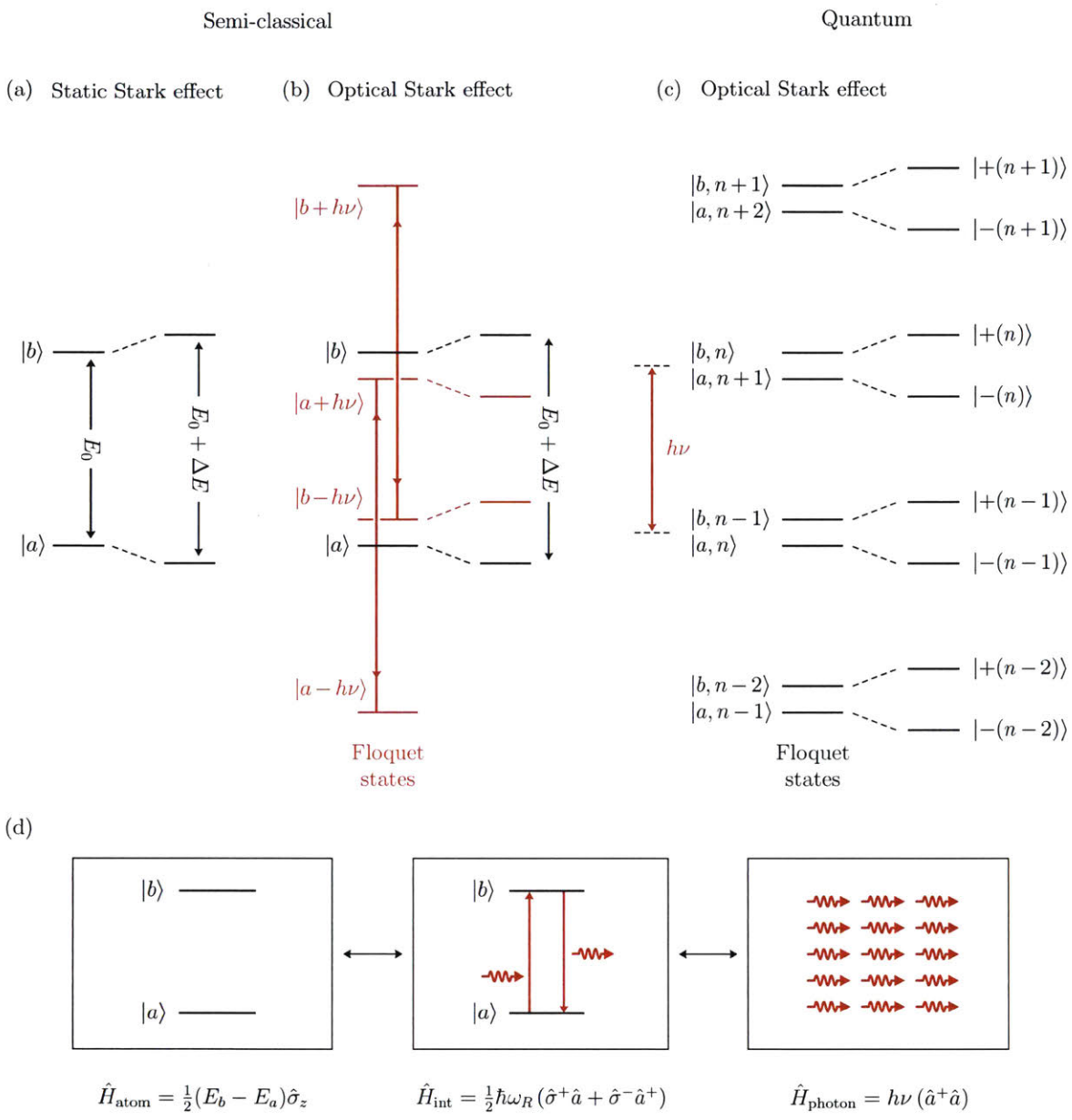

Figure 4.1: (a) Energy level diagram of the static Stark effect in two-level atoms. **(b)** Semi-classical and **(c)** quantum picture of the optical Stark effect. **(d)** Schematic of the three Hamiltonian terms in describing the coherent light-matter interaction.

represented by the classical fields as external perturbation. By diagonalizing the Hamiltonian, the atomic energy levels can be obtained and the optical Stark effect is apparent in the light-induced change of the energy spectrum. The creation of the Floquet states can also be seen from the energy denominator of the shift as will be described below. In the quantum description, on the other hand, light is represented by quantized

oscillators, from which the Floquet states are seen in the quantized photon energy spacing in the energy spectrum. In the following, we will begin by discussing the semi-classical picture of the interaction, and later compare with the quantum picture.

Similar to the static Stark effect, the optical Stark effect also results from induced energy repulsion between two states. To understand this, we consider a two-level atomic system of states $|a\rangle$ and $|b\rangle$ with respective energies of E_a and E_b **(Fig 4.1a)**, and we put this atom in the presence of static electric field $\mathcal{E}$. Since the atomic orbitals have a definite parity, either even or odd under spatial inversion symmetry, the application of first-order perturbation with $\mathcal{E}$ keeps the energy levels unchanged. Hence, the Stark effect in atoms emerges from the second-order perturbation with $\mathcal{E}$, inducing a hybridization between states $|a\rangle$ and $|b\rangle$ that results in shifted energy levels by as much as

$$\Delta E_b = \frac{|\langle b|\hat{p}\mathcal{E}|a\rangle|^2}{E_b - E_a} = \frac{\mathcal{M}_{ab}^2|\mathcal{E}|^2}{E_b - E_a} \tag{4.3}$$

$$\Delta E_a = \frac{|\langle b|\hat{p}\mathcal{E}|a\rangle|^2}{E_a - E_b} = -\frac{\mathcal{M}_{ab}^2|\mathcal{E}|^2}{E_b - E_a} \tag{4.4}$$

where $\hat{p}$ is the electric dipole moment operator of the atom, $\mathcal{E}$ is the static electric field strength, and $\mathcal{M}_{ab}$ is the polarization matrix element between $|a\rangle$ and $|b\rangle$. Such energy shifts result in a wider separation of the energy levels, also known as the state repulsion, with magnitude

$$\Delta E = 2\frac{\mathcal{M}_{ab}^2|\mathcal{E}|^2}{E_b - E_a} \tag{4.5}$$

where the magnitude is quadratic in $\mathcal{E}$ and is inversely proportional to the energy separation $E_b - E_a$ before the application of the field **(Fig 4.1a)**.

In the optical Stark effect, the perturbation is written as $\hat{H}'(t) = \hat{p}\mathcal{E}(t)$, where $\mathcal{E}(t) = \mathcal{E}_0 \cos 2\pi\nu t$ is the oscillating electric field with amplitude $\mathcal{E}_0$ and frequency ν. Here, we can use the standard time-dependent perturbation theory [56] to find the shift of the energy levels

$$\Delta E_b(t) = H'_{ab}(t)\exp\left(\frac{i(E_b - E_a)t}{\hbar}\right)\frac{1}{i\hbar}\int_0^t H'_{ab}(t')\exp\left(-\frac{i(E_b - E_a)t'}{\hbar}\right)dt' \qquad (4.6)$$

where $\Delta E_a(t)$ has a similar expression after switching the index. It is insightful to write the perturbation Hamiltonian as $\hat{H}'(t) = \hat{p}\mathcal{E}_0\left(e^{i2\pi\nu t} + e^{-i2\pi\nu t}\right)/2$. In this way, we can identify the perturbation as coherent absorption and emission of light from the atomic states. By evaluating Equation 4.6, we can obtain the time-averaged shift of the energy levels

$$\Delta\bar{E}_b = \frac{1}{2}\left[\frac{\mathcal{M}_{ab}^2\langle\mathcal{E}^2\rangle}{E_b - E_a - h\nu} + \frac{\mathcal{M}_{ab}^2\langle\mathcal{E}^2\rangle}{E_b - E_a + h\nu}\right] \qquad (4.7)$$

$$\Delta\bar{E}_a = -\frac{1}{2}\left[\frac{\mathcal{M}_{ab}^2\langle\mathcal{E}^2\rangle}{E_b - E_a - h\nu} + \frac{\mathcal{M}_{ab}^2\langle\mathcal{E}^2\rangle}{E_b - E_a + h\nu}\right] \qquad (4.8)$$

where $\langle\mathcal{E}^2\rangle = \mathcal{E}_0^2/2$ is the time-averaged value of the electric field squared. These expressions are consistent with the case of the static electric field in Equation 4.3 & 4.4 in which $h\nu \to 0$ and $\langle\mathcal{E}^2\rangle \to \mathcal{E}_0^2$. Furthermore, by comparing the energy denominator with the static case, we can see that the two terms in $\Delta\bar{E}_b$ correspond to the state repulsion of $|b\rangle$ by two photon-dressed states. These two states originate from the coherent absorption and emission of light from state $|a\rangle$, as shown in **Fig 4.1b**. Similarly, the two terms in $\Delta\bar{E}_a$ are the state repulsion of $|a\rangle$ by the two photon-dressed states of $|b\rangle$. These photon-dressed states are the Floquet states that we identified in the main text. In our experiment, $h\nu$ is detuned only slightly below $E_b - E_a$ such that the contribution from the first term to the energy shift dominates, and that of the second term can be neglected. As a result, the energy level separation increases by

$$\Delta\bar{E} = \frac{\mathcal{M}_{ab}^2\langle\mathcal{E}^2\rangle}{E_b - E_a - h\nu} \qquad (4.9)$$

This is the semi-classical result of the optical Stark shift that we obtained for Equation 4.2 previously. As can be seen from this expression, the energy shift is linearly proportional to the light intensity and is inversely proportional to the light energy detuning from the $E_b - E_a$ transition.

4.1.2. Quantum-mechanical description

On the other hand, the fully quantized description of the optical Stark effect can be described by using the standard Jaynes-Cummings model [57] where light is represented by quantized oscillators with energy of $h\nu$. The Hamiltonian is given by

$$\hat{H} = \frac{1}{2}(E_b - E_a)\hat{\sigma}_z + h\nu\hat{a}^+\hat{a} + \frac{1}{2}\hbar\omega_R(\hat{\sigma}^+\hat{a} + \hat{\sigma}^-\hat{a}^+) \tag{4.10}$$

where the three terms correspond to the two-level atom, the photon reservoir, and the atom-photon interactions, respectively **(Fig 4.1d)**, $\hbar\omega_R$ is the atom-photon coupling strength (Rabi frequency), and the Pauli matrices and the ladder operators are given by

$$\hat{\sigma}_z = |b\rangle\langle b| - |a\rangle\langle a| \tag{4.11}$$

$$\hat{\sigma}^- = |a\rangle\langle b| \tag{4.12}$$

$$\hat{\sigma}^+ = |b\rangle\langle a| \tag{4.13}$$

$$\hat{a}|n\rangle = \sqrt{n}|n-1\rangle \tag{4.14}$$

$$\hat{a}^+|n\rangle = \sqrt{n+1}|n+1\rangle \tag{4.15}$$

where $|n\rangle$ is the number of photons. Due to the interaction term, this Hamiltonian only couples states $|a, n+1\rangle$ and $|b, n\rangle$, which we can use as the basis for the Hamiltonian matrix

$$H = h\nu\left(n + \frac{1}{2}\right)\begin{pmatrix}1 & 0\\ 0 & 1\end{pmatrix} + \frac{1}{2}\begin{pmatrix}E_b - E_a - h\nu & \hbar\omega_R\sqrt{n+1}\\ \hbar\omega_R\sqrt{n+1} & -(E_b - E_a - h\nu)\end{pmatrix} \tag{4.16}$$

This Hamiltonian matrix can be diagonalized to give the energies

$$E_{n,\pm} = h\nu\left(n + \frac{1}{2}\right) \pm \frac{1}{2}\sqrt{(E_b - E_a - h\nu)^2 + (\hbar\omega_R)^2(n+1)} \tag{4.17}$$

As can be seen from this expression, the Floquet states emerge naturally through the discrete energy term in units of $h\nu$ **(Fig 4.1c)**. Additionally, even in the absence of external perturbation of light ($n = 0$), states $|a\rangle$ and $|b\rangle$ can still exhibit hybridization through the

vacuum field, for which the coupling strength is $\hbar\omega_R$ [58]. The optical stark shift of $|a\rangle \rightarrow |b\rangle$ optical transition can also be evaluated, after taking a weak field approximation in which $\hbar\omega_R \ll E_b - E_a - h\nu$, giving

$$\Delta E \cong \frac{1}{2}\frac{n(\hbar\omega_R)^2}{E_b - E_a - h\nu} \tag{4.18}$$

where $(\hbar\omega_R)^2$ is proportional to $\langle\mathcal{E}^2\rangle$. Thus, both the semi-classical and the quantum description of coherent light-matter interaction give consistent picture about the Floquet states and the energy shift due to the optical Stark effect.

4.2. Experimental methods

The sample consists of high-quality monolayers of WS_2 that were CVD-grown on sapphire substrates [10, 11, 59], and all measurements in this study were conducted at ambient condition (300 K, 1 atm). In our experiments, we used a Ti:sapphire amplifier producing laser pulses with duration of 50 fs and at 30 kHz repetition rate. Each pulse was split into two arms. For the pump arm, the pulses were sent to an optical parametric amplifier to generate tunable photon energy below the exciton absorption ($h\nu < E_x$), while for the probe arm the pulses were sent through a delay stage and a white-light continuum generator ($h\nu = 1.78$–2.48 eV, chirp-corrected). The two beams were focused at the sample, and the probe beam was reflected to a monochromator and a photodiode for lock-in detection [26]. By scanning the grating and the delay stage, we were able to measure $\Delta R/R$ (and hence $\Delta\alpha$) as a function of energy and time delay. Here, $\Delta\alpha(\omega, t) = \alpha(\omega, t) - \alpha_0(\omega)$. The pump and probe polarizations were varied separately by two sets of polarizers and quarter-wave plates, allowing us to perform valley-selective measurements, and an additional half-wave plate for tuning the pump pulse intensity.

4.3. Observation of the optical Stark effect

Similar effects have been encountered in solid-state systems, where the electronic states are in the form of Bloch bands that are periodic in momentum space. In the presence of monochromatic light, the Hamiltonian of crystalline solids becomes periodic in both

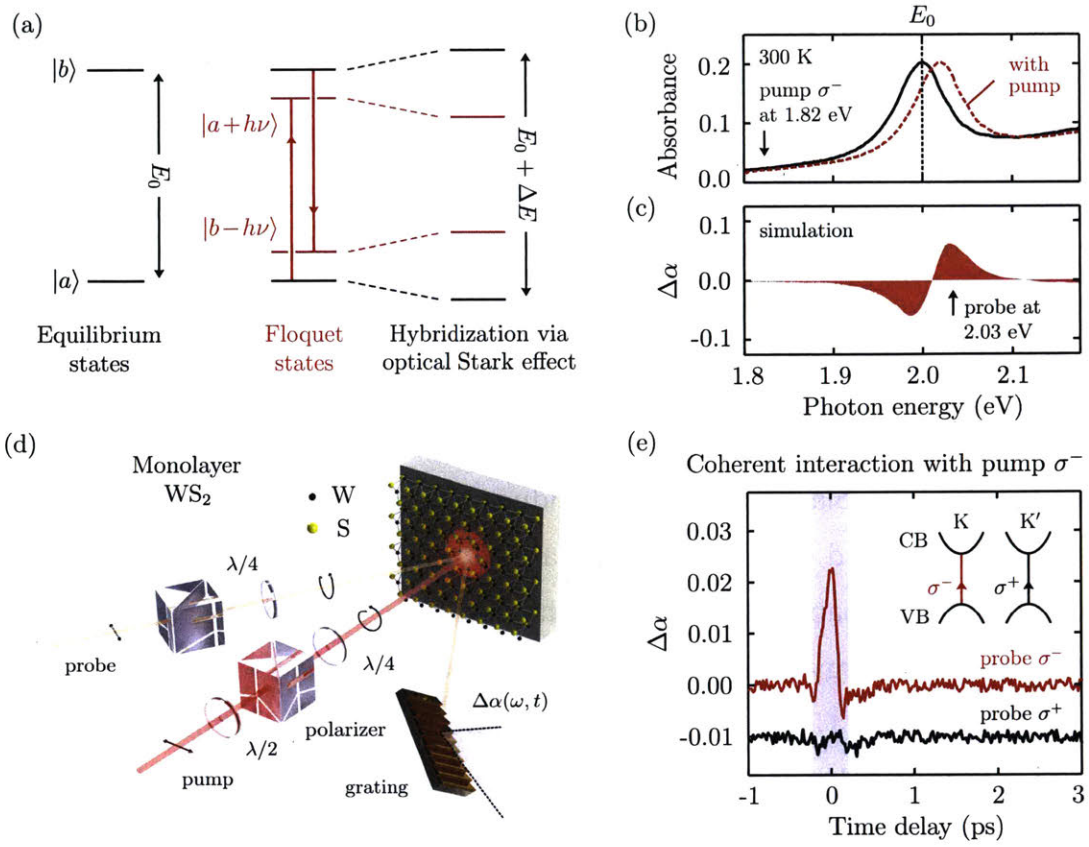

Figure 4.2: The optical Stark effect and its observation in monolayer WS_2. **(a)** Energy level diagram of two-level $|a\rangle$ and $|b\rangle$ atoms showing that the equilibrium and Floquet states $|a + h\nu\rangle$ and $|b - h\nu\rangle$ can hybridize, resulting in shifted energy levels. **(b)** Measured absorbance of monolayer WS_2 (black) and a hypothetical absorbance curve (dashed) that simulates the optical Stark effect. **(c)** The simulated change of absorption induced by the pump pulses. **(d)** Schematic of transient absorption spectroscopy set-up. **(e)** Time trace of α, induced by pump pulses of σ^- helicity, measured using probe pulses of the same (σ^-, red) and opposite (σ^+, black, with offset for clarity) helicities. It shows that the optical Stark effect occurs only during the pump pulse duration ($\Delta t = 0$ ps) and when the pump and probe helicities are the same.

space and time, which leads to the creation of Floquet-Bloch bands that repeat in momentum and energy. Floquet-Bloch bands were very recently observed for the first time on the surface of a topological insulator irradiated by mid-infrared light [60]. The optical Stark effect can also occur in solids through the interaction between photo-induced Floquet-Bloch bands and equilibrium Bloch bands [61]. To date, this effect has only been reported in a very limited number of materials, with Cu_2O [62], GaAs [63-66] and Ge [67] semiconductors among the few examples.

Here we report the first observation of the optical Stark effect in a monolayer TMD WS_2. The recently discovered monolayer TMDs are 2D crystalline semiconductors with unique spin-valley properties [15] and energetically degenerate valleys at the K and K' points in the Brillouin zone that are protected by time-reversal symmetry. We demonstrate by using circularly polarized light that the effect can be used to break the valley degeneracy and raise the exciton level at one valley by as much as 18 meV in a controllable valley-selective manner.

In monolayer WS_2, the energy of the lowest exciton state is 2.00 eV at room temperature (**Fig 4.2b**, black). In order to induce a sufficiently large energy shift of this exciton (as simulated and exaggerated for clarity in **Fig 4.2b**, dashed), we use an optical parametric amplifier capable of generating ultrafast laser pulses with high peak intensity and tunable photon energy (1.68–1.88 eV). To measure the energy shift we use transient absorption spectroscopy **(Fig 4.2d)**, which is a powerful technique capable of probing the resulting change in the absorption spectrum $\Delta\alpha$, as simulated in **Fig 4.2c** [26]. The unique optical selection rules of monolayer TMDs allow for $\Delta\alpha$ at the K (or K') valley to be measured with valley-specificity by using left (or right) circularly polarized probe light (inset in **Fig 4.2e**).

To search for the optical Stark effect in WS_2, we start by measuring the change in the optical absorption $\Delta\alpha$ as a function of time delay Δt between the pump and probe laser pulses **(Fig 4.2e)**. To generate the necessary Floquet-Bloch bands, we tune the pump photon energy to 1.82 eV so that it is just below the absorption peak, with pulse duration 160 fs at FWHM, fluence 60 uJ/cm2, and polarization σ^- (left circularly polarized). Since the optical Stark effect is expected to shift the absorption peak to higher energy, the probe photon energy is chosen to be 2.03 eV, which is above the equilibrium absorption peak. **Fig 4.2e** shows that when σ^- is used to probe $\Delta\alpha$ (red trace), there is a sharp peak that only exists at $\Delta t = 0$ ps when the pump pulse is present. This signifies that we are sensitive to a coherent light-matter interaction occurring between the pump pulse and the sample. When σ^+ is used to probe $\Delta\alpha$ (black trace), we observe no discernible signal above the noise level at all time delays. This shows that probing the optical Stark effect in this material is strongly sensitive to the selection of pump and probe helicities. Closer examination of $\Delta\alpha$

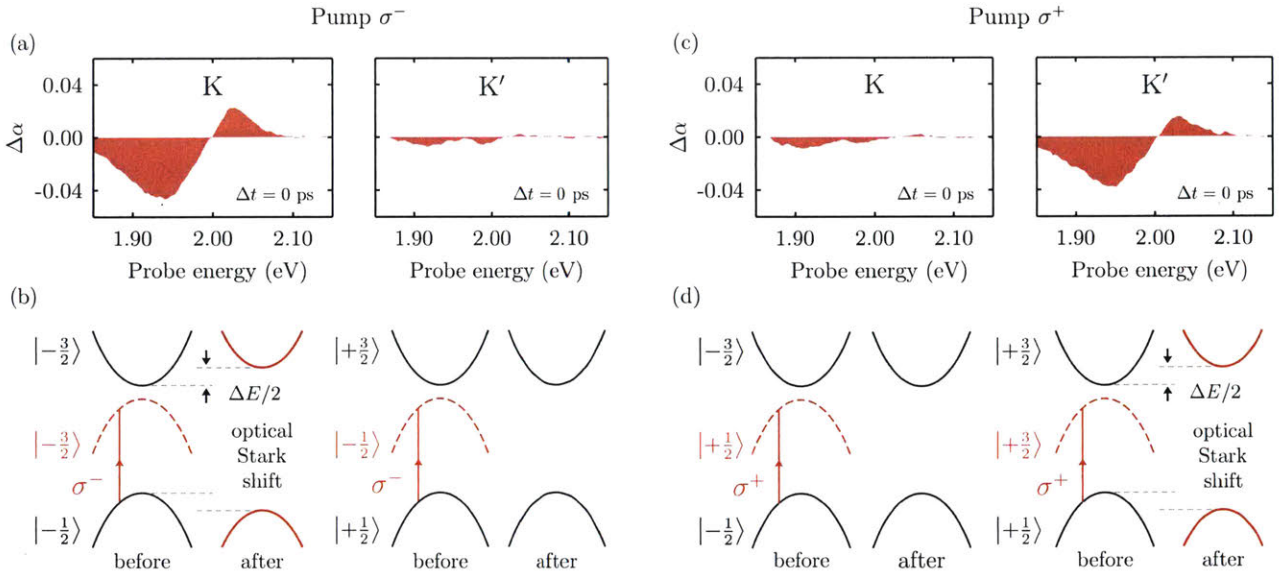

Figure 4.3: The valley selectivity of the optical Stark effect. **(a)** Valley-specific α spectra (background-subtracted) induced by σ^- pump pulses probed by using σ^- (K valley) and σ^+ (K' valley) helicities. **(b)** Band diagrams with the pump-induced Floquet-Bloch bands (red dashed curves) and their associated magnetic quantum numbers m. **(c,d)** By switching the pump pulse helicity to σ^+, we also measured the valley-specific α spectra **(c)** and show their corresponding band diagrams **(d)**. The optical Stark effect occurs only between states having the same magnetic quantum numbers.

spectrum in the range of 1.85–2.15 eV reveals a faint but noticeable background signal that is present at both valleys (Supplementary Section 4.7.1). In the following discussion, we only consider results taken at $\Delta t = 0$ ps for which the background signals (BG) have also been subtracted in order to focus on the optical Stark effect.

4.4. Valley-selectivity

Having demonstrated that the optical Stark effect can be induced in a monolayer TMD, we now study its valley-specificity and demonstrate that it can be used to lift the valley degeneracy. **Fig 4.3a** shows the $\Delta\alpha$ spectra induced by σ^- pump pulses probed in a valley-selective manner by using σ^- (K valley) and σ^+ (K' valley) probe helicities. When the same pump and probe helicities are used ($\sigma^-\sigma^-$, **Fig 4.3a** left panel), the spectrum displays a positive (and negative) $\Delta\alpha$ at energies higher (and lower) than the original absorption peak, clearly indicates that the absorption peak at the K valley is shifted to higher energy

via the optical Stark effect. The spectrum of the opposite pump and probe helicities ($\sigma^-\sigma^+$, **Fig 4.3a** right panel), in contrast, shows a negligible signal across the whole spectrum, indicating an insignificant change to the absorption peak at the K' valley. **Fig 4.3c** shows identical measurements of $\Delta\alpha$ using instead a σ^+ pump helicity, where it can be seen that the effect is switched to the K' valley. This valley-selective probing of the optical Stark shift shows that the effect is well isolated within a particular valley determined by the pump helicity. The magnitude of the effect in either valley can also be smoothly tuned as the pump helicity is continuously varied from fully σ^- to fully σ^+ (Supplementary Section 4.7.2).

The valley-specific optical Stark effect shares the same origin with the valley-selective photoexcitation as previously reported in this class of materials [18-20]. Both effects arise due to valley selection rules. In monolayer TMDs, the highest-occupied states in the valence band (VB) are associated with magnetic quantum numbers m, where m = -1/2 and +1/2 at K and K' valleys, respectively, as shown in **Fig 4.3b** and repeated in **Fig 4.3d**. Meanwhile, the lowest-unoccupied states in the conduction band (CB) consist of four quasi-degenerate states, with m = -3/2 and -1/2 at K valley, and m = +3/2 and +1/2 at K' valley. Two of these states ($m = \pm 1/2$) have no role in the effect, thus omitted from the figures. Coherent absorption of light by the VB creates a Floquet-Bloch band $|VB + h\nu\rangle$ for which the magnetic quantum numbers are added by the light helicity that carries Δm = -1 (σ^-) or +1 (σ^+). The proximity in energy between this Floquet-Bloch band and the equilibrium CB can induce a hybridization that leads to an energy shift provided that they have the same magnetic quantum numbers. Although this material is known to possess a strong excitonic interaction, the physical description of the valley-selectivity still remains the same and, for the purpose of understanding the effect, the energy of the equilibrium CB is essentially reduced by as much as the exciton binding energy [68]. This explains the valley-selective energy shift we observed in our experiments. These optical selection rules can be described by Equation 4.2 after replacing $\mathcal{M}_{ab}$ by $\mathcal{M}_v$, which now represents the valley selection rules for different laser polarizations [68]. Additional experiments (below) investigating the dependence on the light intensity and frequency show that the measured energy shift obeys Equation 4.2 extremely well.

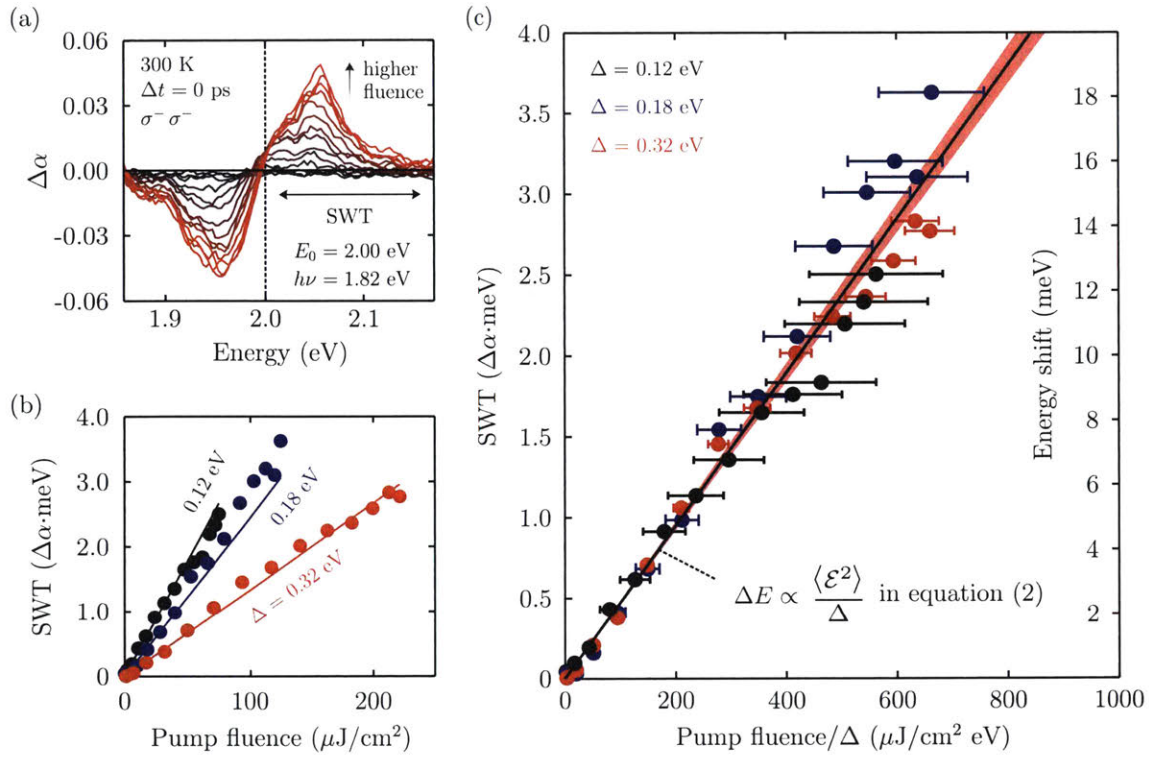

Figure 4.4: Fluence and detuning dependences of the optical Stark shift. **(a)** Fluence dependence of α spectra with fluences up to 120 μJ cm^{-2} measured with the same pump and probe helicities. **(b)** Fluence and detuning dependences of the SWT with the integration range shown in (a). **(c)** SWT plotted as a function of fluence/Δ, showing that all of the data points fall along a common slope (black line). The horizontal error bars correspond to the pump bandwidth of 43 meV at full-width at half-maximum. The fitting slope (black line) and the 95% confidence band (red shading) shows an excellent agreement with the characteristic dependences of the optical Stark shift in Equation 4.2.

4.5. Fluence & detuning dependences

Fig 4.4a shows a series of $\Delta\alpha$ spectra that grow with increasing pump fluence. It can be shown (in Supplementary Section 4.7.3) that the integrated $\Delta\alpha$ as a function of energy, namely the spectral weight transfer (SWT), is proportional to the energy shift,

$$\int_{E_0}^{\infty} \Delta\alpha(\omega) d\omega = A\,\Delta E \tag{4.19}$$

where A is the peak absorbance of the sample. In our analysis, it is sufficient to integrate $\Delta\alpha$ in the range of $2.00 \leq \omega \leq 2.18$ eV because the signal vanishes beyond this upper limit. The

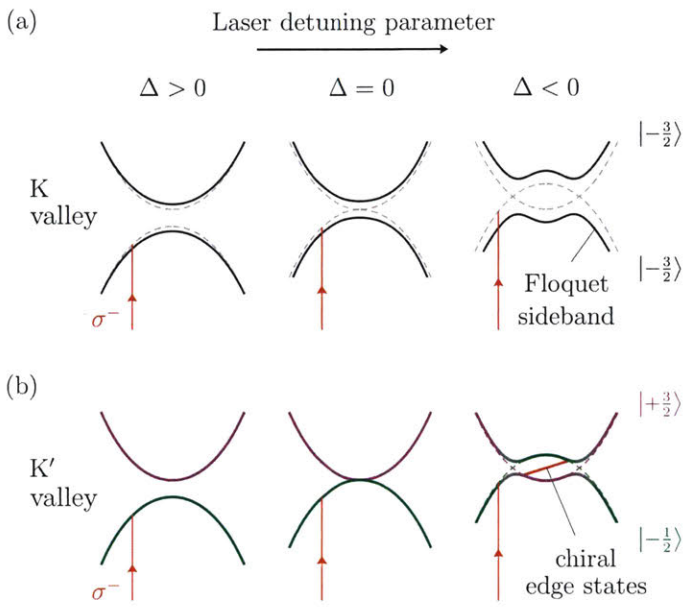

Figure 4.5: Valley-specific Floquet topological phase. **(a, b)** Hybridization between the Floquet–Bloch band and the conduction band when Δ is varied, which gives rise to the avoided crossing at the K valley (a) and the band inversion at the K' valley (b). The crossing straight line (red) at the K' valley is the anticipated chiral edge states due to the band inversion.

SWT is plotted in **Fig 4.4b** (blue circles) as a function of pump fluence, together with accompanying results measured with smaller (black) and larger (red) laser detuning energies Δ. Not only they show a linear dependence with fluence but they also share a common slope when plotted as a function of fluence/Δ in **Fig 4.4c**. This is in excellent agreement with Equation 4.2. By obtaining the peak absorbance $A = 0.2$ from **Fig 4.2c**, we can set an energy scale for ΔE in the right vertical axis of **Fig 4.4c**, which estimates an energy shift of 18 meV measured at the highest fluence. We note that, for a given fluence and energy detuning, this material exhibits the largest optical Stark shift in any materials reported to date. We have used Equation 4.2 to calculate the expected energy shift by using an estimated Rabi frequency, which agrees very well with the measured value (see Supplementary Section 4.7.4).

4.6. Proposal: valley-specific Floquet topological phase in TMDs

The ability to create valley-specific Floquet-Bloch bands in monolayer TMDs offers a means to induce new topological phases [49-51] with valley-specific edge states. To elucidate its valley-specificity, we can ignore the excitonic interaction without loss of

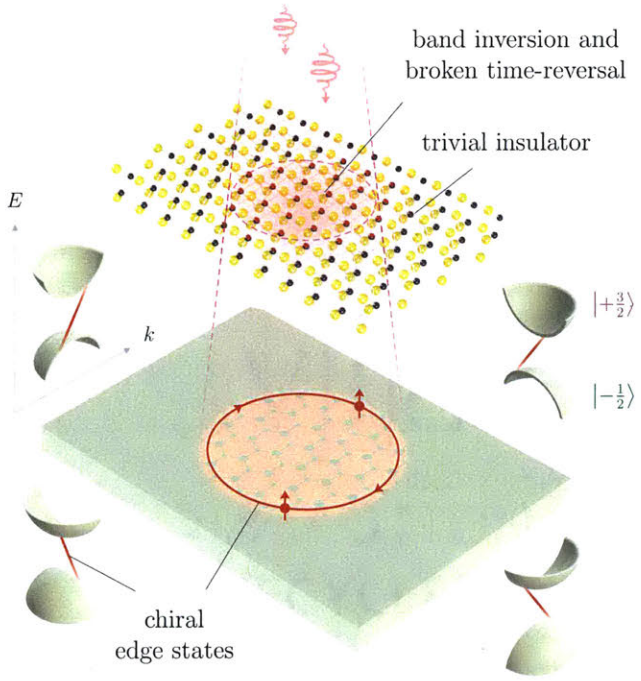

Figure 4.6: Schematic of the Floquet-driven chiral edge state along the boundary of the laser-exposed region.

generality, and we conceive a situation where the σ^- detuning energy is varied across the interband transition, as shown in **Fig 4.5a** (K valley) and **4.5b** (K' valley). In these figures, the coherent absorption of light (red line) from the valence band creates a Floquet-Bloch band close to the conduction band edge (dashed curves) and induces hybridization that results in energy repulsion (solid curves). When the pump detuning is set at $\Delta < 0$, band inversion should occur at K' valley which is accompanied by an avoided crossing away from the symmetry point ($k = K' + \delta k$). This gap-opening allows the creation of topological edge states (red) [69]. Here the pump helicity breaks time-reversal symmetry, inducing chiral edge states along the boundary of the laser-exposed region where the topological order changes **(Fig 4.6c)** [70]. We note that this description is robust when the Floquet-Bloch band is far above the interband transition. In a situation where the photon energy approaches the exciton resonance, careful consideration of the excitonic effects is necessary especially within the Rabi splitting of the exciton-polariton energy dispersion [71]. In future works, it should be possible to investigate such Floquet chiral edge states provided that the probing signal is made insensitive to contributions from photoexcited

excitons and intervalley scattering [37, 72]. This opens an exciting avenue, which merges Floquet-driven topological transition and valley physics together.

The observation of a large valley-selective optical Stark effect in monolayer WS_2 represents the first clear demonstration of broken valley degeneracy in a monolayer TMD. This is possible because of the formation of Floquet-Bloch states via the application of circularly polarized light, which breaks time-reversal symmetry and allows for the lifting of the intervalley spin degeneracy. These findings offer additional control for valley-switching applications on a femtosecond timescale, as well as provide a means to generate new valley-selective topological phases in monolayer TMDs.

4.7. Supplementary

4.7.1. Time-resolved spectra

The equilibrium absorption spectrum of our sample (**Fig 4.7a**, black), as measured using differential reflectance microscopy, shows an absorption peak at $E_0 = 2.00$ eV, which is also consistent with other measurements [73]. Optical Stark effect gives rise to an energy shift of this peak (simulated in **Fig 4.7a**, dashed), which can be measured as induced absorption $\Delta\alpha$ at slightly higher energy (simulated in **Fig 4.7b**, red shaded). This $\Delta\alpha$ spectrum is the signature of the optical Stark effect in our experiment.

In **Fig 4.7c**, we present a pair of experimentally measured $\Delta\alpha$ spectra as a function of pump-probe time delay. Here, we used left circularly polarized (σ^-) pump pulses with photon energy of 1.82 eV (below the absorption peak), fluence of 60 uJ/cm2, and duration of 160 fs at FWHM. The probe helicity is tuned to be the same (σ^-, left panel) and opposite (σ^+, right panel) to the pump helicity. On the left panel, the spectra show a distinct feature centered within the pump pulse duration ($\Delta t = 0$ fs), which consists of positive $\Delta\alpha$ above the original absorption peak and negative below it. On the right panel, however, the spectra show only a faint and premature signal during the pump pulse duration, in contrast to that of the left panel. At $\Delta t > 200$ fs, both panels share common spectra, where $\Delta\alpha$ is negative at the absorption peak and positive below it.

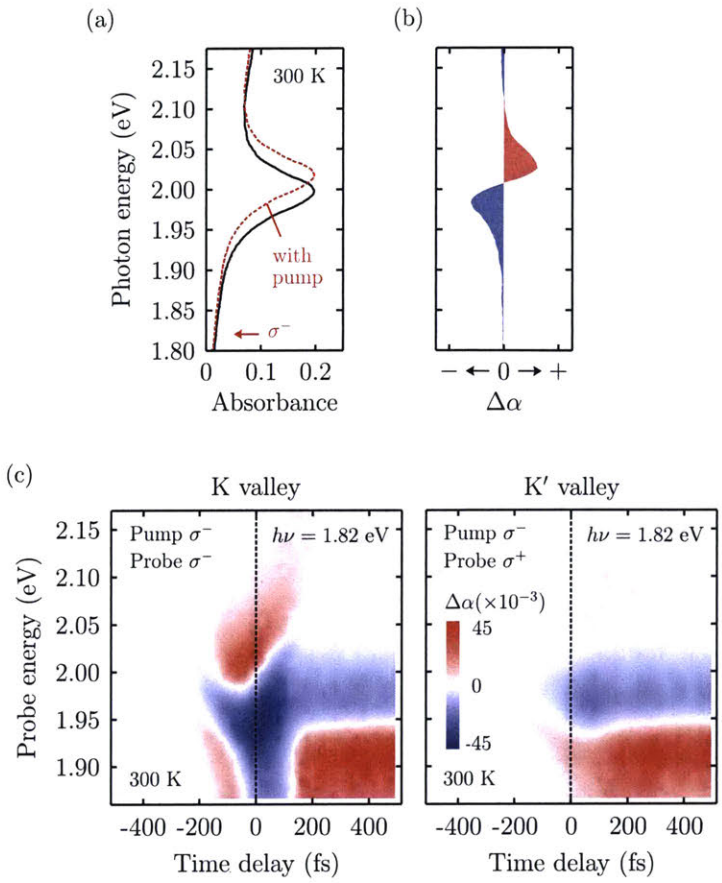

Figure 4.7: (a) Measured absorbance of monolayer WS_2 (black) and a rigidly shifted one (dashed) to simulate the optical Stark effect. **(b)** The simulated change of absorption induced by the pump pulse. **(c)** Valley-specific $\Delta\alpha(\omega, t)$ spectra measured using pump-probe pulses of the same (left panel) and opposite (right panel) helicities. It shows a peak shift only at the K valley ($\Delta t = 0$ fs) and common background signals from the photoexcited excitons ($\Delta t > 200$ fs).

The $\Delta\alpha$ spectra at $\Delta t = 0$ fs shown on the left panel indicate that the absorption peak is shifted to higher energy. The absence of this feature on the right panel indicates that the shift is well isolated within only the light-driven valley. The non-zero $\Delta\alpha$ values at $\Delta t > 200$ fs in both panels, when the pump pulse no longer persist, are induced by photoexcited excitons, due to excitonic bleaching and biexcitonic absorption [26, 37], and they are present in both valleys. These excitons, however, do not contribute to the optical Stark effect and just add common background signals in both valleys. The different signatures of $\Delta\alpha$ spectra (**Fig 4.7c**, left panel) that are induced by the pump pulse ($\Delta t = 0$ fs) and by the photoexcited excitons ($\Delta t > 200$ fs) prove that the observed valley-selective energy shift is driven coherently by light, and not by photoexcited excitons. In order to

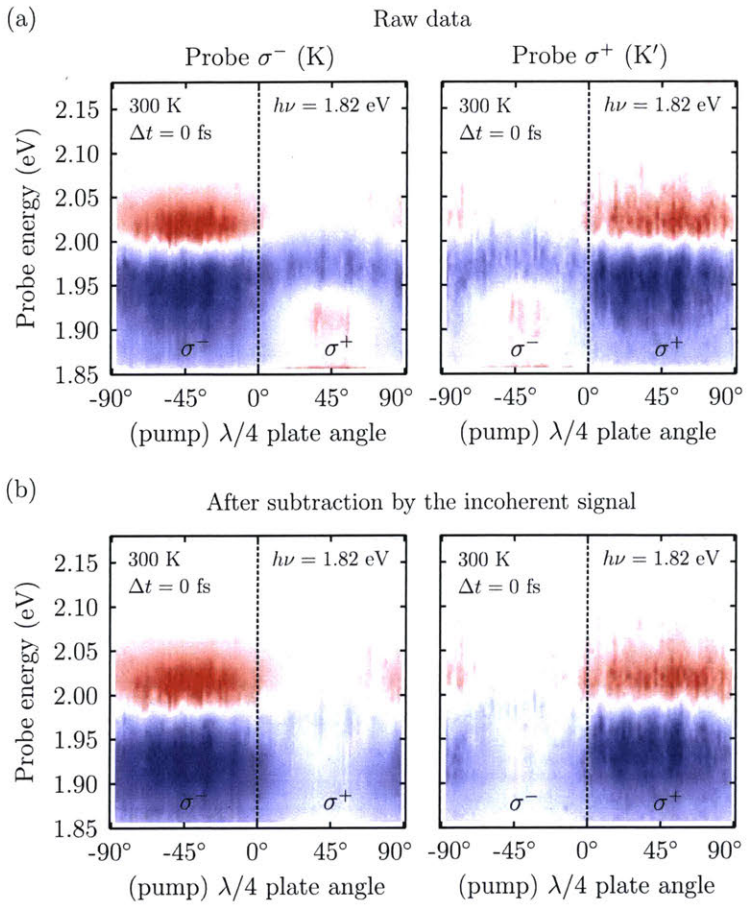

Figure 4.8: (a) Valley-specific $\Delta\alpha(\omega, t = 0)$ spectra measured as a function of pump polarization, before and **(b)** after the background (BG) signal subtraction. These spectra show that the energy shifts are well isolated in either valley.

eliminate slight contributions from the photoexcited excitons at $\Delta t = 0$ fs, we take $0.5\times\Delta\alpha(\omega, \Delta t = 400$ fs) from the right panel of **Fig 4.7c** as the background (BG) signal. This BG signal will be used in the next section.

4.7.2. Polarization-resolved spectra

In the following discussion, we only consider results taken at $\Delta t = 0$ fs where the optical Stark effect takes place. We present the valley specific $\Delta\alpha$ spectra, before **(Fig 4.8a)** and after **(Fig 4.8b)** BG subtraction, as a function of pump polarization. We used σ^- and σ^+ probe pulses to monitor the K valley (left panels) and K' valley (right panels), respectively. The latter figures show a clear transition of $\Delta\alpha$ value: largest when the pump pulses have the same helicities with the probe pulses, halved when linearly polarized, and nearly zero

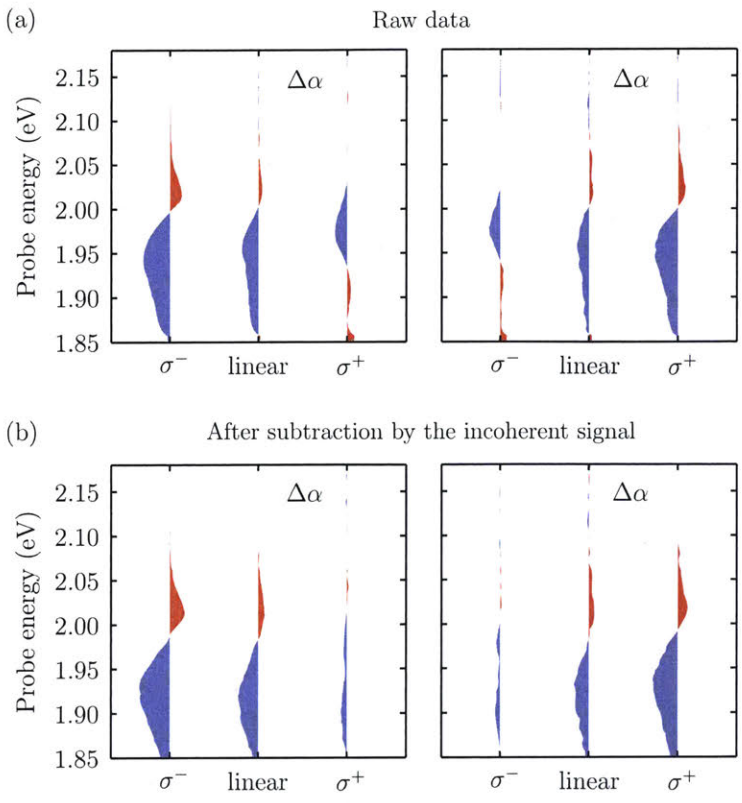

Figure 4.9: (a, b) Spectral polarization cuts at K (left) and K' (right) valleys from the corresponding panels in **Fig 4.8** for a clearer comparison.

for opposite helicites, as is also summarized in **Fig 4.9b**. This results from the shifting of energy levels as a function of pump polarization, as is schematically depicted in **Fig 4.10**. This behavior arises from the selection rule in the matrix element $\mathcal{M}_v$, which is responsible for the previously reported valley-selective photoluminescence.

4.7.3. Obtaining energy shift

We can represent the absorption peak by a Gaussian lineshape. The resulting absorption spectrum due to an energy shift of ΔE can be expressed as

$$\alpha(\omega, \Delta E) = A \exp\left(-\frac{(\omega - \Delta E)^2}{2c^2}\right) \tag{4.20}$$

where A is the absorption peak, c is the FWHM$/2\sqrt{2\,ln2}$, and $\hbar = 1$. **Fig 4.11a** shows the absorption spectra before (grey shaded) and after (red curve) the peak is shifted by ΔE. We

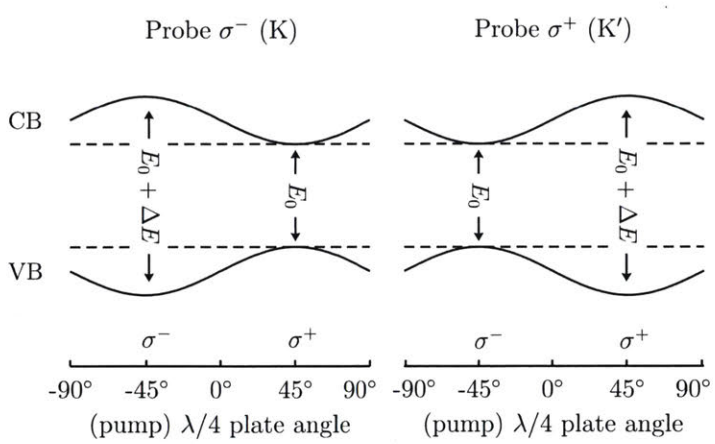

Figure 4.10: Band diagrams showing how the energies of the conduction band (CB) and the valence band (VB) are shifted as a function of pump polarization.

can then obtain the change of the absorption spectrum **(Fig 4.11b)** before and after the shift

$$\begin{aligned}\Delta\alpha(\omega,\Delta E) &= \alpha(\omega,\Delta E) - \alpha(\omega) \\ &= -\left(\frac{\alpha(\omega) - \alpha(\omega-\Delta E)}{\Delta E}\right)\Delta E \\ &= -\frac{\partial\alpha}{\partial\omega}\Delta E \\ &= \frac{\omega}{c^2}\alpha(\omega)\Delta E\end{aligned} \tag{4.21}$$

where we only keep terms in the first order of ΔE. This result has been routinely used to estimate the energy shift ΔE via optical Stark effect through measuring the change in the absorption $\Delta\alpha$ at a particular energy ω [61]. This method, however, is insensitive to distinguishing a peak shift from a peak broadening. Thus, it is crucial to measure the full spectrum of $\Delta\alpha$, which can be performed in transient absorption spectroscopy [26], and verify if the measured $\Delta\alpha$ spectrum profile results from a peak shift **(Fig 4.11b)**.

To determine the shift in the peak position, we can integrate the area of this $\Delta\alpha(\omega,\Delta E)$ curve in the range of $0 \leq \omega \leq \infty$, which is referred in the main text as the spectral weight transfer (SWT), and by using Equations 4.20 & 4.21 it can be evaluated as

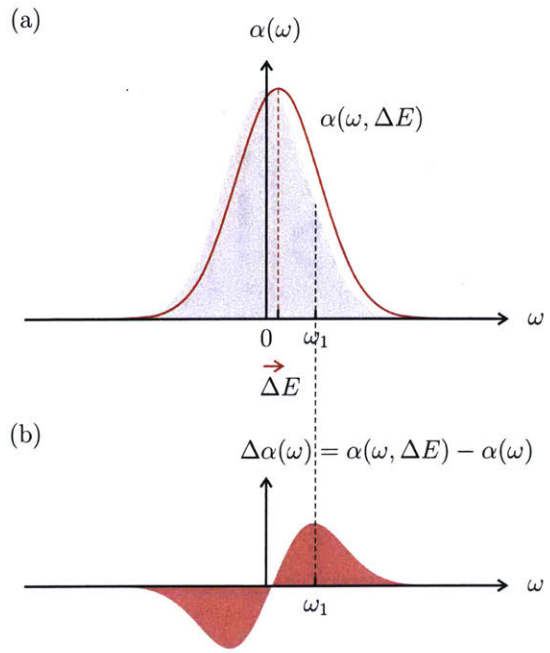

Figure 4.11: (a) Absorption spectra before (black) and after (red) the absorption peak is shifted by ΔE. **(b)** The change of the absorption spectrum due to shifted energy.

$$\begin{aligned}\int_0^\infty \Delta\alpha(\omega, \Delta E)d\omega &= \int_0^\infty \left(\frac{\omega}{c^2}\alpha(\omega)\Delta E\right)d\omega \\ &= \frac{\Delta E}{c^2}\int_0^\infty \omega A \exp\left(-\frac{\omega^2}{2c^2}\right)d\omega \\ &= A\Delta E\int_0^\infty dx \exp(-x) \\ &= A\Delta E\end{aligned} \tag{4.22}$$

That is, by measuring the SWT and the absorption peak A, we can extract the energy shift ΔE due to the optical Stark effect. The measured SWT is plotted in **Fig 4.4b-c** in the main text with a new energy scale as determined by Equation 4.22.

4.7.4. Comparison from semi-classical theory

In theory, the optical Stark shift is completely described by the transition dipole moment $\mathcal{M}_{ab}$, pump field strength $\mathcal{E}_0$ and pump detuning Δ, which can be calculated and

compared with the data in **Fig 4.4c**. The energy shift has a simple expression (Equations 4.9 and 4.18) given by

$$\Delta E = \frac{(\hbar\omega_R)^2}{2\Delta} \tag{4.23}$$

where $\hbar\omega_R$ $(= \mathcal{M}_{ab}\mathcal{E}_0)$ is the Rabi frequency. We can estimate for $\mathcal{M}_{ab}$ from the study of quantum well semiconductors [74] given as

$$(\mathcal{M}_{ab})^2 = \left(\frac{eh}{2E_0}\right)^2 \frac{E_g}{m_c} \tag{4.24}$$

where E_0 (= 2 eV) is the transition energy of the exciton, E_g (= 2.3 eV) is the quasiparticle band gap [6], m_c (= 0.32 m_0) is the effective mass of the conduction electron [75]. This gives $\mathcal{M}_{ab} = 56$ Debye for monolayer WS_2 (1 Debye = 3.3×10^{-30} Cm), which is about twice the value obtained for GaAs quantum wells [76]. For the maximum energy shift of 18 meV, as measured at $\Delta = 180$ meV, we used pump fluence of 120 uJ/cm2 with pulse width of 160 fs (obtained from **Fig 4.2e**). This gives the peak irradiance of I = fluence/width = $\varepsilon_0 c \mathcal{E}_0{}^2/2$ from which we can determine the field strength of $\mathcal{E}_0 = 75$ MV/m and the Rabi frequency of $\hbar\omega_R = 87$ meV. This calculation yields the energy shift of $\Delta E = 21$ meV which is consistent with the measured value of 18 meV from our experiments.

In comparison to the optical Stark effect, the energy shift resulted if we were applying a static field instead of the optical field is given by

$$\Delta E = 2\frac{(\mathcal{M}_{ab}\mathcal{E}_0)^2}{E_0} \tag{4.25}$$

As can be seen, in order to obtain the same energy shift, we need $\mathcal{E}_0 = 125$ MV/m, which is very difficult to achieve in dc. Note also that the application of a static electric field in monolayer WS_2 will not lift the intervalley degeneracy.

Chapter 5

Intervalley biexcitonic optical Stark effect in monolayer WS_2

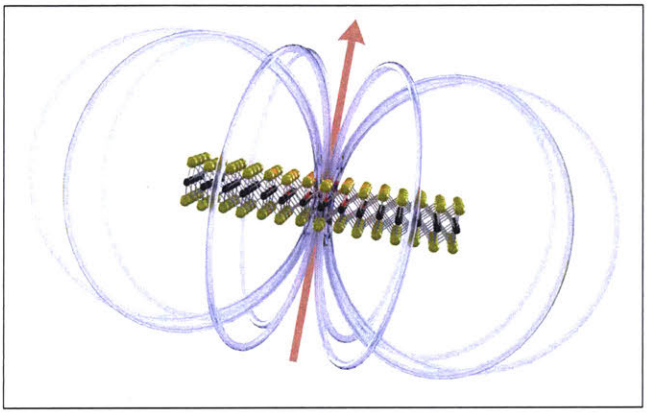

Contents[3]

[3] The work presented in this chapter is published in the following journal:
Edbert J. Sie, Chun Hung Lui, Yi-Hsien Lee, Jing Kong, Nuh Gedik
***Nano Letters* 16**, 7421-7426 (2016)

Coherent optical driving can effectively modify the properties of electronic valleys in transition metal dichalcogenides. Here we observe a new type of optical Stark effect in monolayer WS_2, one that is mediated by *intervalley biexcitons* under the blue-detuned driving with circularly polarized light [77]. We find that such helical optical driving not only induces an exciton energy downshift at the excitation valley, but also causes an anomalous energy upshift at the opposite valley, which is normally forbidden by the exciton selection rules but now made accessible through the intervalley biexcitons. These findings reveal the critical, but hitherto neglected, role of biexcitons to couple the two seemingly independent valleys, and to enhance the optical control in valleytronics.

5.1. Blue detuned optical Stark effect

Monolayer transition metal dichalcogenides (TMDs) host tightly-bound excitons in two degenerate but inequivalent valleys (K and K'), which can be selectively photoexcited using left (σ^-) or right (σ^+) circularly polarized light **(Fig 5.1a)** [15, 18-20]. The exciton energy levels can be tuned optically in a valley-selective manner by means of the optical Stark effect [29, 30]. Prior research has demonstrated that monolayer TMDs driven by below-resonance (red-detuned) circularly polarized light can exhibit an upshifted exciton level, either at the K or K' valleys depending on the helicity, while keeping the opposite valley unchanged. This valley-specific phenomenon arises from the exciton state repulsion by the photon-dressed (Floquet) state in the same valley, a mechanism consistent with the optical Stark effect in other solids [63, 78].

Despite much recent progress, a complete understanding of the optical Stark effect in monolayer TMDs is still lacking. First, the downshift of exciton level, an anticipated complementary effect using above-resonance (blue-detuned) optical driving, has not been demonstrated. This is challenging because the blue-detuned light excites real exciton population, which can easily obscure the optical Stark effect. Secondly, when the detuning is sufficiently small and comparable to the biexciton binding energy, the effect may involve a coherent formation of the recently identified intervalley biexcitons [26, 37]. These biexcitons are expected to contribute to the optical Stark effect, as indicated by earlier

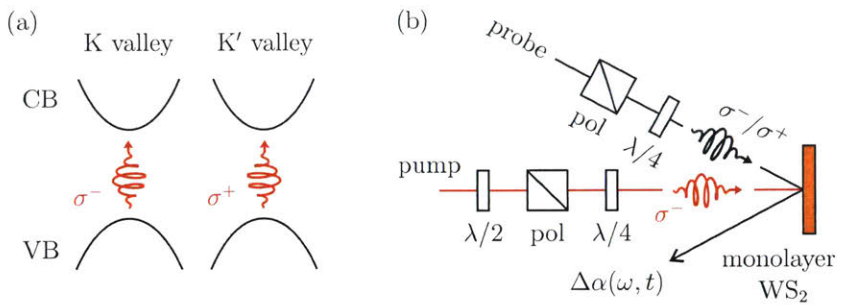

Figure 5.1: (a) K and K' valleys couple selectively with left (σ^-) and right (σ^+) circularly polarized light due to selection rules. **(b)** Schematic of the pump-probe spectroscopy setup.

studies in semiconductor quantum wells [79, 80]. Elucidating these processes is therefore crucial to understand the coherent light-matter interactions in monolayer TMDs.

In this chapter, we explore the optical Stark effect in monolayer WS_2 under blue-detuned optical driving. By pumping the system above the A exciton resonance using left-circularly polarized laser pulses, we can *lower* the exciton energy at the K valley. In addition, as the driving photon energy approaches the resonance, an unexpected phenomenon emerges – the exciton energy at the opposite (K') valley is *raised*. This observation is anomalous because interaction with the driving photon is forbidden at this valley by the exciton selection rules. The upshifted exciton level also contrasts sharply with the downshifted level at the K valley. These findings reveal the strong influence of intervalley biexcitons on the optical Stark effect. By including their contributions in an expanded four-level scheme of optical Stark effect, we are able to account for all the main observations in our experiment.

5.2. Experimental methods

High-quality monolayer WS_2 samples were grown by chemical vapor deposition (CVD) on sapphire substrates [10, 11, 59]. We performed all of the optical measurements at ambient condition (300 K, 1 atm). In our experiments, we used a Ti:sapphire amplifier that emits laser pulses with 50 fs duration and 30 kHz repetition rate. Each pulse was split into two arms. For the pump arm, the pulses were sent to an optical parametric amplifier to generate tunable pump photon energy. For the probe arm, the pulses were sent through a

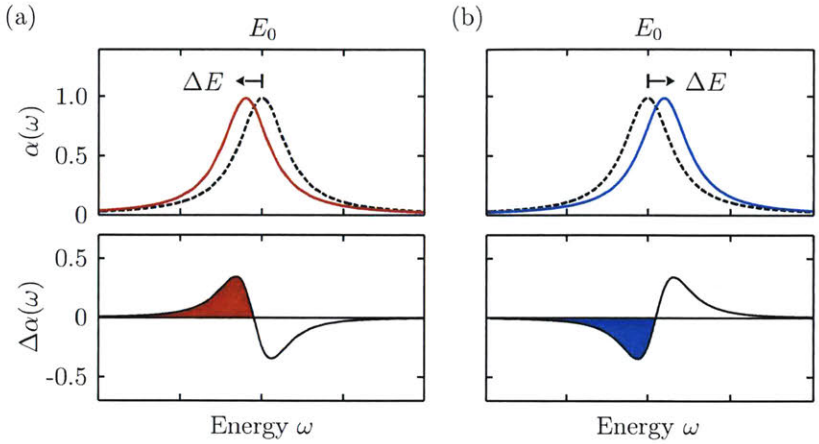

Figure 5.2: (a, b) Simulated absorption spectra $\alpha(\omega)$ that are shifted by ΔE to lower and higher energies (upper panels), as well as their induced absorption spectra $\Delta\alpha(\omega)$ (lower panels).

delay stage and a white-light continuum generator ($h\nu = 1.78$–2.48 eV, chirp-corrected). The pump and probe polarizations were varied separately by two sets of polarizers and quarter-wave plates **(Fig 5.1b)**. The two beams were focused onto the sample, and the reflected probe beam was diffracted by a monochromator and measured by a photodiode for lock-in detection. By scanning the grating and the delay stage, we were able to measure $\Delta R/R$ as a function of photon energy and time delay, from which we extracted the corresponding change of absorption $\Delta\alpha(\omega, t) = \alpha(\omega, t) - \alpha_0(\omega)$ using the method in ref. [26].

5.3. Experimental results & data analysis

We monitor the pump-induced change of exciton levels at the K (K') valley by using the reflection of synchronized broadband probe pulses with σ^- (σ^+) polarization **(Fig 5.1b)**. Our samples are high-quality WS_2 monolayers grown by chemical vapor deposition on sapphire substrates [10, 11, 59]. The change of absorption ($\Delta\alpha$) in monolayer WS_2 can be extracted from the change of reflection by using Kramers-Kronig analysis within a thin-film approximation [10, 16]. The resulting $\Delta\alpha$ spectrum typically shows a single-cycle waveform, which allows us to determine the direction and magnitude of the exciton energy shift (ΔE) **(Fig 5.2a-b)**. In our experiment, we examine the lower-energy part of $\Delta\alpha$ spectrum (filled color in **Fig 5.2a-b**), because the coherent contribution is more pronounced below the energy resonance (E_0). For a blue-detuned optical Stark effect **(Fig**

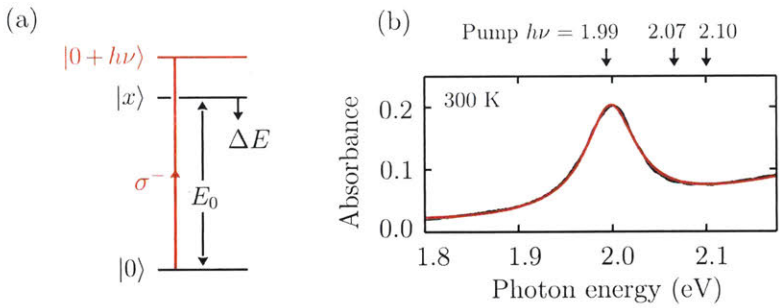

Figure 5.3: Blue-detuned optical Stark effect and its observation in monolayer WS_2. **(a)** Blue-detuned optical driving scheme, where we use σ^- pump pulse with photon energy $h\nu$ slightly above the exciton resonance E_0. **(b)** Measured absorption spectrum of monolayer WS_2 shows that E_0 = 2.00 eV at 300 K (black curve), which can be fitted with a single Lorentzian (neutral) exciton peak plus a background polynomial slope from the higher energy states (red curve).

5.3a), the pump photon energy lies slightly higher than the A exciton resonance in monolayer WS_2, which is at E_0 = 2.00 eV from our measured absorption spectrum **(Fig 5.3b)** as well as from other experiments [81]. We observe no side peak or shoulder below the exciton absorption peak, implying that our samples have weak trionic effect **(Fig 5.3b)**.

Figure 5.4a-b shows the $\Delta\alpha$ spectra at zero pump-probe delay at three different pump photon energies ($h\nu$ = 2.10, 2.07, 1.99 eV) but the same pump fluence (28 uJ/cm^2). We display the spectra in the range of 1.80-1.96 eV, where the coherent effect is more pronounced and less contaminated by the pump scattering. For the σ^- probe **(Fig 5.4a)**, the spectral shape is similar to that in **Fig 5.2a**, indicating a redshift of the exciton level at the same (K) valley. As the pump photon energy approaches the resonance from 2.10 to 1.99 eV, the magnitude increases considerably, indicating an increasing redshift of the exciton level. This observation complements the previous studies, which reported a blueshift under red-detuned optical driving. In contrast, the $\Delta\alpha$ spectra at the opposite (K') valley exhibit a distinct form, as revealed by the σ^+ probe **(Fig 5.4b)**. Its value is negative in the range of 1.80 – 1.90 eV, with a waveform similar to that in **Fig 5.2b**. This indicates a blueshift of the exciton level at the K' valley, which becomes more substantial as the pump approaches the resonance (see Supplementary Section 5.6.3 for more discussions on both blue- and red-detuned pumping).

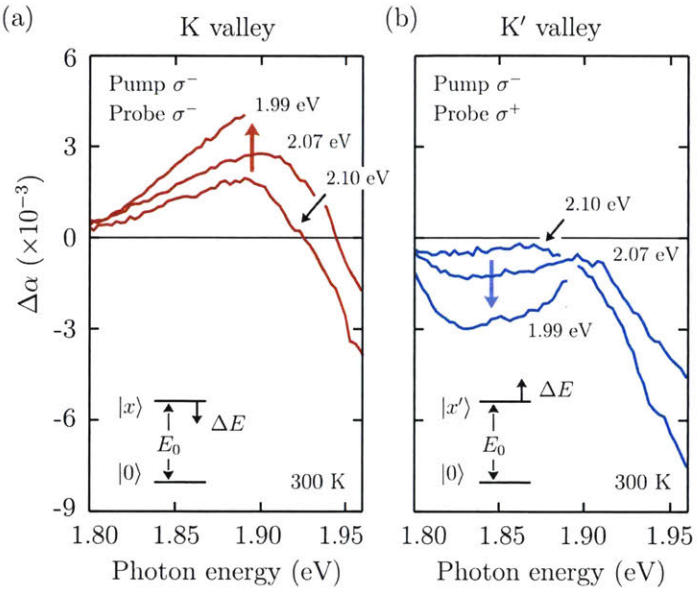

Figure 5.4: (a, b) Valley-specific $\Delta\alpha$ spectra induced by σ^- pump pulses ($h\nu$ = 1.99, 2.07, 2.10 eV) and monitored by using σ^- (K) and σ^+ (K') broadband probe pulses at pump-probe time delay $\Delta t = 0$. The increasing $\Delta\alpha$ at K valley indicates a pump-induced redshift of exciton energy. On the other hand, the decreasing $\Delta\alpha$ at K' valley, though unexpected, indicates a pump-induced blueshift of exciton energy.

The observed spectra include both the coherent signals from the optical Stark effect and the incoherent signals from the exciton population that is unavoidably generated by the above-resonance optical pumping [26, 37, 72, 82-88]. The coherent signals are known to appear only within the pump pulse duration, whereas the incoherent signals remain after the pulsed excitation. Their different time dependences allow us to separate them by monitoring the temporal evolution of $\Delta\alpha$. **Figure 5.5a-b** shows the time traces after the excitation with 200 fs laser pulses at photon energy $h\nu$ = 2.03 eV. At pump-probe delay $\Delta t > 1$ ps, $\Delta\alpha$ is similar for both valleys, with positive value at the probe energy of 1.84 eV but negative value at 1.95 eV. These features correspond to the exciton population effects, where the slow rise in **Fig 5.5a** shares the same timescale with the intervalley scattering. This suggests that the initial population-induced dynamics arises from the same scattering mechanism, which can be mediated by defects and electron-phonon interactions. At zero

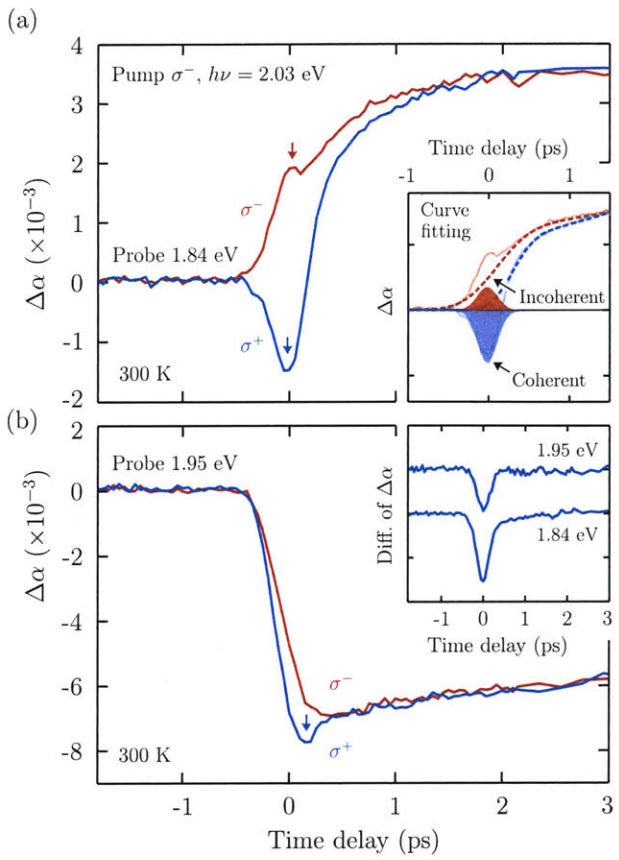

Figure 5.5: (a, b) Time traces of $\Delta\alpha$ induced by σ^- pump pulses ($h\nu$ = 2.03 eV) and monitored at probe energy of 1.84 and 1.95 eV with different helicities. The top inset shows the curve fitting decomposition of the coherent and incoherent signals. The bottom inset shows the valley contrast of the signals, $\Delta\alpha(\sigma^+) - \Delta\alpha(\sigma^-)$, where the two curves are offset for clarity.

pump-probe delay, however, the two valleys exhibit significantly different response. The difference can be attributed to the optical Stark effect, a coherent process that follows the pump pulse intensity profile. At probe energy 1.84 eV, the coherent contribution is particularly prominent and can be readily separated from the incoherent background by direct extrapolation (Insets of **Fig 5.5a-b** and **Fig 5.10** in the Supplementary Section 5.6.2).

We have extracted the coherent component of $-\Delta\alpha$ at 1.84 eV and plot the values as a function of pump fluence **(Fig 5.6)**. The associated energy shift ΔE can be estimated from the differential form $\Delta\alpha(\omega, \Delta E) = -(d\alpha/d\omega)\Delta E$. Given the measured $-\Delta\alpha$ and the slope at 1.84 eV, we have evaluated such energy shift (the right vertical axis of **Fig 5.6**). Our result shows that the exciton level at K and K' valleys respectively downshifts (-4 meV) and upshifts (9 meV) under the σ^- blue-detuned optical driving. The magnitude of both shifts

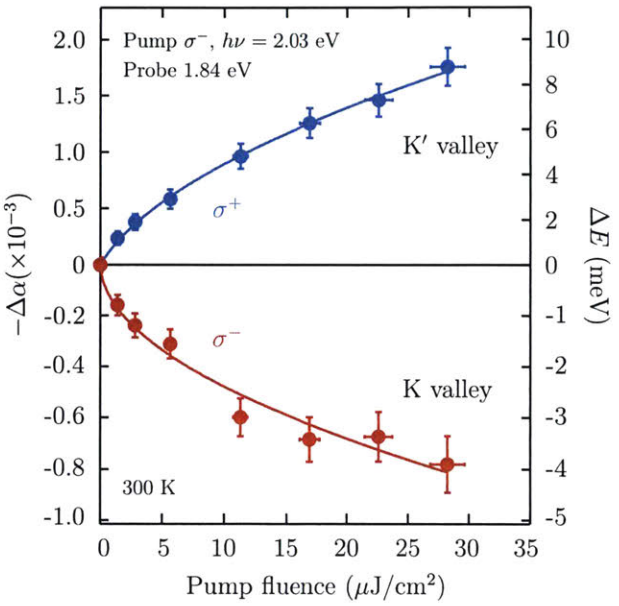

Figure 5.6: Fluence dependence of the blue-detuned optical Stark shift. The measured data of $-\Delta\alpha(\propto \Delta E)$ are plotted at increasing pump fluence (σ^-, $h\nu = 2.03$ eV), measured valley-selectively at probe energy of 1.84 eV. The energy scale on the right axis is estimated based on the measured absorption slope of 0.2/eV at 1.84 eV. Note that the energy scaling is different between the two valleys. The fitting curves show that the K and K' valleys exhibit square-root fluence dependences, as discussed in the main text.

increases sublinearly with pump fluence, in contrast to the linear fluence dependence in prior red-detuned experiments.

5.4. Intervalley biexcitonic optical Stark effect

The upshift of exciton level at the K' valley is anomalous. First, according to the well-known selection rules in monolayer WS_2, the K' valley is not accessible by the σ^- (K valley) optical driving. The observed optical Stark effect at K' valley apparently violates this selection rule. Secondly, even if the access to the K' valley is allowed, a blue-detuned optical driving is expected to downshift the exciton level, as in the case of the K valley. The energy upshift at the K' valley apparently defies this common knowledge of optical Stark effect, hence it must arise from a different mechanism, one that is beyond the framework of interaction between light and single excitons.

We attribute this phenomenon to the optical Stark effect that is mediated by intervalley biexcitons. Recent research has revealed significant interactions between individual excitons in monolayer TMDs. In particular, two excitons at different valleys can be bound to form an excitonic molecule, the intervalley biexciton, with unusually large binding energies (Δ_b = 40–70 meV) [26, 37, 43, 89, 90]. These intervalley biexcitons offer an effective channel to couple the two valleys, with selection rules different from those of single excitons. In view of such strong biexcitonic effect, we can account for our observations within a four-level scheme, which includes the ground state $|0\rangle$, the two valley exciton states $|x\rangle$ and $|x'\rangle$, and the intervalley biexciton state $|xx'\rangle$ (**Fig 5.7**). In this scheme, the optical pumping creates two types of photon-dressed (Floquet) states – one from the ground state $|0 + h\nu\rangle$ and the other from the biexciton state $|xx' - h\nu\rangle$. The former can interact with the exciton state $|x\rangle$ at the K valley. Since $|0 + h\nu\rangle$ lies above $|x\rangle$ in a blue-detuned experiment, repulsion between the two states causes $|x\rangle$ to downshift. This is responsible for the ordinary optical Stark effect at the K valley (red dots in **Fig 5.6**). In contrast, the biexciton Floquet state $|xx' - h\nu\rangle$ can interact with the exciton state $|x'\rangle$ at the opposite (K') valley according to different selection rules for the intervalley biexciton. Since $|xx' - h\nu\rangle$ lies below $|x'\rangle$, repulsion between the two will cause $|x'\rangle$ to upshift. This is responsible for the anomalous optical Stark effect at the K' valley (blue dots in **Fig 5.6**). It is evident that the intervalley biexciton plays a unique role in coupling the two valleys, and the effect can be utilized for enhanced control of valley degree of freedom [91].

5.4.1. Four-level Jaynes-Cummings model

In order to investigate the photoinduced coupling between these states, we consider a four-level Jaynes-Cummings model, with a procedure similar to but extended from our previous work [29, 57]. Such a model has been successfully applied to describe the light-dressed states in many semiconductor systems, and can readily be adopted to describe the exciton-biexciton system [29, 63, 67, 78, 92, 93]. By virtue of the unique valley selection rules in this system, the originally 4x4 Hamiltonian matrix can be simplified into two *decoupled* 2x2 Hamiltonian matrices

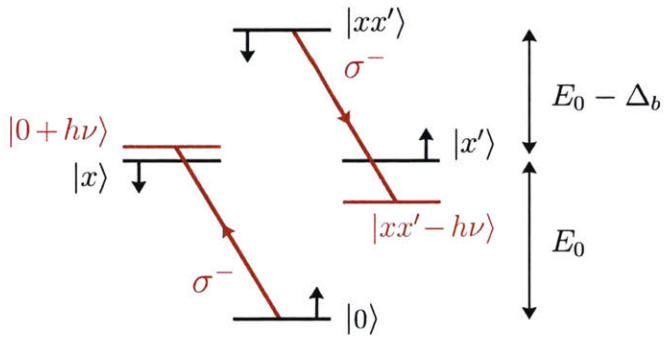

Figure 5.7: Energy level diagram of the intervalley biexcitonic optical Stark effect. Here the σ^- pump pulse is blue-detuned above the energy resonance between the ground state $|0\rangle$ and the exciton state $|x\rangle$. Coherent absorption from $|0\rangle$ results in a photon-dressed state $|0 + h\nu\rangle$, while coherent emission from the intervalley biexciton state $|xx'\rangle$ results in a photon-dressed state $|xx' - h\nu\rangle$. Additional states $|x - h\nu\rangle$ and $|x' + h\nu\rangle$ also arise in this situation, but we omit them from this figure for the sake of clarity.

$$\hat{H}_K = \frac{1}{2}E_0\hat{\sigma}_z + h\nu\hat{a}^+\hat{a} + \frac{1}{2}g(\hat{\sigma}^+\hat{a} + \hat{\sigma}^-\hat{a}^+) \tag{5.1}$$

$$\hat{H}_{K'} = \frac{1}{2}(E_0 - \Delta_b)\hat{\sigma}_z + h\nu\hat{a}^+\hat{a} + \frac{1}{2}g'(\hat{\sigma}^+\hat{a} + \hat{\sigma}^-\hat{a}^+) \tag{5.2}$$

The three terms from left to right in each Hamiltonian correspond to the two-level system, the photon reservoir, and the exciton-photon interactions, respectively. Possible contribution from real exciton population is neglected in this model. Here, g and g' are the exciton-photon coupling strengths, $\hat{\sigma}$'s are the Pauli matrices, $\hat{a}$ and $\hat{a}^+$ are the photon ladder operators, and Δ_b is the biexciton binding energy. The Hamiltonian $\hat{H}_K$ couples states $|0, n+1\rangle$ and $|x, n\rangle$, while $\hat{H}_{K'}$ couples states $|x', n\rangle$ and $|xx', n-1\rangle$, where n is the number of photons. By using these states as the basis, we can express the Hamiltonians as the following matrices

$$H_K = \frac{1}{2}\begin{pmatrix} h\nu - E_0 & g\sqrt{n+1} \\ g\sqrt{n+1} & -(h\nu - E_0) \end{pmatrix} \tag{5.3}$$

$$H_{K'} = \frac{1}{2}\begin{pmatrix} h\nu - E_0 + \Delta_b & g'\sqrt{n} \\ g'\sqrt{n} & -(h\nu - E_0 + \Delta_b) \end{pmatrix} \tag{5.4}$$

Here we omit the energy offsets $h\nu(n \pm \frac{1}{2})$ of the photon reservoir. Diagonalization of the Hamiltonian matrices gives the eigenenergies of the photon-dressed states $E_K = \pm\frac{1}{2}\sqrt{(h\nu - E_0)^2 + g^2(n+1)}$ and $E_{K'} = \pm\frac{1}{2}\sqrt{(h\nu - E_0 + \Delta_b)^2 + g'^2(n)}$, where $g\sqrt{n+1} = \mathcal{M}\mathcal{E}_0$ and $g'\sqrt{n} = \mathcal{M}'\mathcal{E}_0$ are the Rabi frequencies. Here $\mathcal{M}$ and $\mathcal{M}'$ are the moments for $|0\rangle \rightarrow |x\rangle$ and $|x'\rangle \rightarrow |xx'\rangle$ transitions, respectively, and $\mathcal{E}_0$ is the electric field amplitude of the light. From these expressions, we can finally obtain the optical Stark shifts of the exciton states

$$\Delta E_K = -\frac{1}{2}\left(\sqrt{(h\nu - E_0)^2 + \mathcal{M}^2\mathcal{E}_0^2} - (h\nu - E_0)\right) \tag{5.5}$$

$$\Delta E_{K'} = +\frac{1}{2}\left(\sqrt{(h\nu - E_0 + \Delta_b)^2 + \mathcal{M}'^2\mathcal{E}_0^2} - (h\nu - E_0 + \Delta_b)\right) \tag{5.6}$$

Despite much similarity, the two optical Stark effects are quantitatively different, because the transition moments are generally different and the biexciton photon-dressed state is offset by Δ_b. In the large detuning limit $h\nu - E_0 \gg \mathcal{M}\mathcal{E}_0$, we retrieve the well-known expression $\Delta E_K = -\mathcal{M}^2\mathcal{E}_0^2/4(h\nu - E_0)$ with a linear fluence dependence, as observed in the previous red-detuned experiment. Conversely, in the small detuning limit $h\nu - E_0 \ll \mathcal{M}\mathcal{E}_0$, we obtain $\Delta E_K = -\frac{1}{2}\sqrt{\mathcal{M}^2\mathcal{E}_0^2}$ with a square-root fluence dependence. The observed sublinear fluence dependence in **Fig 5.6** indicates that the small-detuning limit is reached for both valleys in our experiment. Our fluence dependence data can be fitted with this model **(Fig 5.6)**, with transition moments and effective detunings as adjustable parameters (Supporting Information). The good agreement between the experiment and the model strongly supports that this optical Stark effect is mediated by intervalley biexcitons. We note that trion states can in principle also exhibit an optical Stark effect. However, given the small charge background with no trion absorption feature in our samples **(Fig 5.3b)**, we do not expect the trion states to play a significant role in our observation.

In summary, we have observed an exciton energy downshift at the excitation (K) valley and an energy upshift at the opposite (K') valley, under the blue-detuned optical

driving in monolayer WS_2. While the energy downshift arises from the single-exciton optical Stark effect, the anomalous energy upshift is attributed to the intervalley biexciton optical Stark effect because it exhibits three characteristics: (i) It emerges only within the pump pulse duration, (ii) it has a square-root dependence on the pump fluence, and (iii) it obeys the biexcitonic valley selection rule for opposite circularly polarized light, consistent with our model. Our results show that the intervalley biexciton is not only a rare and interesting quasiparticle by itself, but it also plays an active role to channel a coherent and valley-controllable light-matter interaction.

5.5. Perspective: Zeeman-type optical Stark effect

Apart from slight quantitative difference the two types of optical Stark effects exhibit beautiful contrast and symmetry with the valley indices (K, K') and the direction of the energy shift (down and up shifts). The optical Stark effect at K valley arises from *intravalley* exciton-exciton interaction through statistical Pauli repulsion, whereas the effect at K' valley arises from *intervalley* exciton-exciton interaction through biexcitonic Coulomb attraction. Altogether, the two effects induce opposite energy shift at the two valleys, in contrast to the prior red-detuned optical Stark effect that occurs at only one valley [29, 30]. This behavior is analogous to the Zeeman effect, which splits *antisymmetrically* the electronic valleys under applied magnetic field [94-97]. We may therefore call this new phenomenon a *Zeeman-type optical Stark effect*, in which the circularly polarized light plays the role of the magnetic field that breaks time-reversal symmetry and lifts the valley degeneracy **(Fig 5.8)**. This new finding offers much insight into coherent light-matter interactions in TMD materials, and may find important applications in the design of TMD-based photonic and valleytronic devices.

5.6. Supplementary

5.6.1. Coherent & incoherent optical signals

Unlike in the red-detuned experiments [29, 30], the incoherent signals in our blue-detuned experiments are unavoidable and quite significant, because a large population of

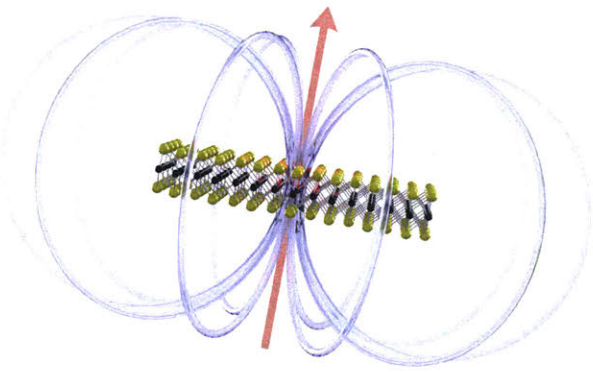

Figure 5.8: Zeeman-type optical Stark effect illustration. The red arrow represents a circularly polarized light that breaks time-reversal symmetry and acts like an applied magnetic field. Coherent interaction between the light and monolayer WS_2 results in a virtual creation of magnetic field lines (blue).

excitons is generated by the optical pumping at above-resonance energy ($h\nu > E_0$). It is therefore important to distinguish the coherent features of the optical Stark effect from the incoherent background due to the photoexcited excitons. Such incoherent signal corresponds to the exciton bleaching, biexciton absorption, and band renormalization, as shown by earlier studies [26, 37, 72, 82-88]. These photoexcited excitons do not contribute to the optical Stark effect, and just add common background signals contributing to the final profiles of the $\Delta\alpha$ spectra in both valleys.

We can exclude other incoherent processes as the responsible mechanism for the observed valley contrastive energy shifts at time-zero. The population-induced biexciton absorption, Pauli blocking and renormalization of band structure should not be responsible, because they normally persist as long as the exciton recombination time (>1 ps). The exciton population imbalance between the K and K' valleys lasts for ~1 ps, still longer than the pulse duration of our pump laser (~200 fs). But it may contribute to the slow rise (~1 ps) of valley contrastive signal in **Fig 5.5a**, possibly due to a small renormalization of band structure. In respect to a possible exciton-exciton interaction, excitons in the same (different) valley are expected to repel (attract) one another and cause a blue (red) shift of the exciton energy, in analogy to the spin-dependent interactions of excitons in semiconductor quantum wells [98, 99]. These predicted valley-dependent

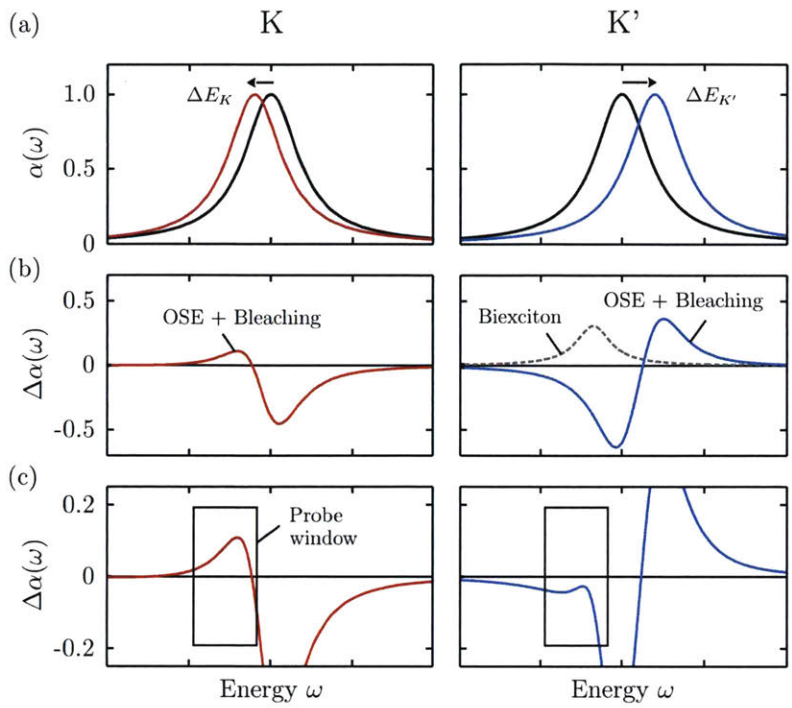

Figure 5.9: A simple illustration for different contributions to the optical signals. Note that this is not an attempt to fit the experimental data, which otherwise requires additional details beyond the present study. **(a)** Simulated absorption spectra $\alpha(\omega)$ that are shifted by ΔE to lower (K) and higher energies (K'). We used ΔE at K' valley twice that of the K valley, to be consistent with the obtained ΔE in our experiments. **(b)** Contributions to $\Delta\alpha(\omega)$ from the optical Stark effect (OSE), exciton bleaching, and biexciton absorption. Note that the biexciton absorption should in principle occur only for cross-polarized pump-probe at K' valley. In situation where intervalley scattering happens during the pump pulse duration, the biexciton absorption can also appear at the K valley. **(c)** Total $\Delta\alpha(\omega)$, where the boxed region corresponds to the probe window in our experiment. Note that here we do not include the large contaminating signal from the pump scattering.

energy shifts are, however, opposite to the energy shifts in our experiment. We can therefore conclude that the valley contrastive energy shift is a coherent phenomenon.

The different contributions to the optical signals are illustrated in **Fig 5.9a-c**. Note that this is not an attempt to fit the experimental data, which otherwise requires additional details beyond the present study. Here, the energy shift (OSE) contribution results from the absorption difference between the shifted and the original absorption spectrum. The bleaching contribution accounts for the population-induced Pauli blocking effect such that the material becomes less absorptive. In this illustration, we use an example where 40% of

the absorption peak is Pauli blocked. Here we assume that the electron population has not rearranged themselves to occupy the shifted absorption peak, so that the bleaching profile is simply derived from the original absorption peak. So, the OSE and the bleaching effects are considered as higher-order perturbations, and their contributions can be treated separately for the purpose of illustration. We also considered a situation where the electron population has quickly rearranged themselves to occupy the shifted absorption peak, and this would still result in a very similar spectral profile. The biexciton contribution is simply taken as a copy of the original absorption peak (here 30%) that is shifted towards lower energy by the amount of biexciton binding energy. The resulting $\Delta\alpha$ spectral profiles can be easily reproduced with a wide range of variation from individual contributions, which are consistent with our measurements within the probe windows **(Fig 5.4)**.

We also want to note that contributions from imperfections or defects can be ruled out in our experiments. Imperfections in monolayer TMDs are well known to have extremely small optical absorption compared to the excitons, even under the excitation of ultrafast pulses. According to other photoluminescence experiments, their contribution is significant only at very low temperature when the trapping is efficient, not at room temperature that we performed our experiment. In addition, their contributions, if there were any, would lack the valley and coherent characteristics shown in our experiment.

5.6.2. Time-trace fitting decomposition analysis

The coherent and incoherent responses can be separated by their distinct dependences on the pump-probe delay. The incoherent processes evolve with the population of excitons, which accumulates during the pump pulse duration and remains afterwards. On the other hand, the coherent processes follow instantaneously the pump pulse intensity profile. **Figure 5.10a** shows the experimentally measured $\Delta\alpha$ spectra as a function of time delay. Here, we used σ^- pump pulses at $h\nu = 1.99$ eV, fluence of 28 uJ/cm^2, and duration of 200 fs. The spectra at K' valley shows a clear coherent effect at $\Delta t = 0$ that persists only as long as the pump pulse duration. Meanwhile the coherent effect at K valley is comparable with the incoherent effects, because photoexcitation is most effective at this valley due to the selection rules. **Figure 5.10b** shows the time cuts of $\Delta\alpha$ spectra at -0.4, 0,

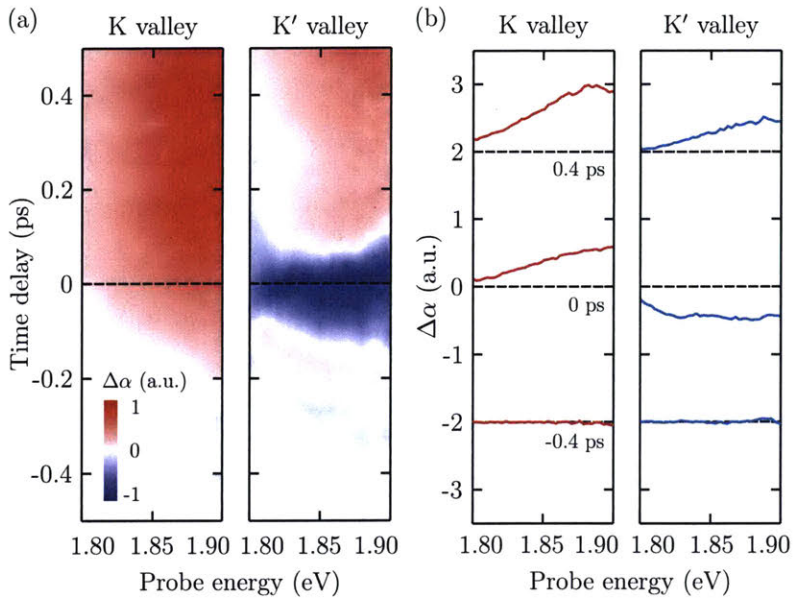

Figure 5.10: (a) Valley-specific $\Delta\alpha(\omega, t)$ spectra induced by σ^- pump pulses at $h\nu = 1.99$ eV, and measured using probe pulses of σ^- (K) and σ^+ (K') helicities at 300 K. It shows a clear coherent signal at K' valley ($\Delta t = 0$ fs) and incoherent signals from the photoexcited excitons afterwards. **(b)** Time cut $\Delta\alpha$ spectra at -0.4, 0, 0.4 ps.

and 0.4 ps, which shows that the spectra exhibit a strong valley contrast at 0 ps due to the coherent process. At longer time delays, the coherent process vanishes and followed by the incoherent process that will have similar magnitudes at both valleys due to the intervalley scattering of excitons.

Figure 5.11a shows $\Delta\alpha$ time traces that are induced by $h\nu = 2.03$ eV (σ^-) and valley-selectively measured with probe energy of 1.84 eV. Consistent with the above description, we find that the time traces exhibit a strong valley contrast at $\Delta t = 0$ ($\Delta\alpha(\sigma^-\sigma^-) - \Delta\alpha(\sigma^-\sigma^+)$, see **Fig 5.11b**) where the coherent signal is expected, and followed by a slow dynamics with diminishing valley contrast where the incoherent signal remains. We performed curve-fitting decomposition in order to separate the Gaussian-like coherent signal (y_1) from the slowly building-up incoherent signal (y_2) as a function of time delay (x), which can be expressed as

$$y_1 = A_1 \exp\left(-\frac{(x - x_0)^2}{t_1^2}\right) \tag{5.7}$$

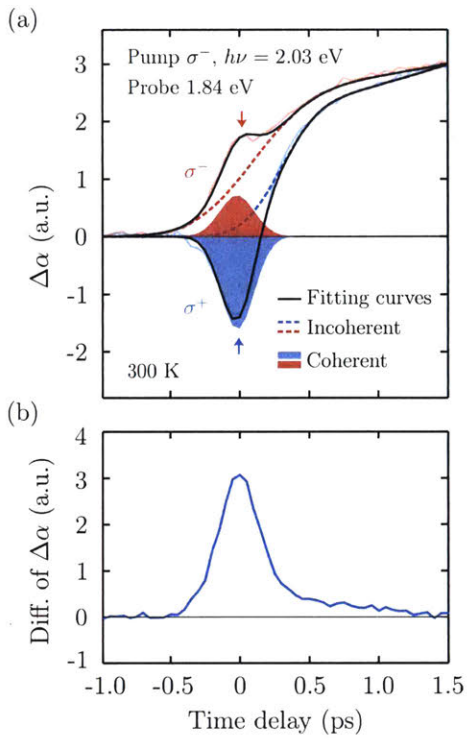

Figure 5.11: (a) Time traces of $\Delta\alpha$ induced by σ^- pump pulses ($h\nu = 2.03$ eV) and monitored at probe energy of 1.84 eV with different helicities. Curve-fitting decomposition shows the Gaussian-like coherent signals (color shaded) and the slow buildup of incoherent signals (dashed lines). **(b)** The difference, $\Delta\alpha(\sigma^-) - \Delta\alpha(\sigma^+)$, shows that the valley-contrast is dominated by the coherent signal at $\Delta t = 0$.

$$y_2 = A_2 \exp\left(-\frac{x - x_0}{t_2}\right)\left(1 - \mathrm{erf}\left(\frac{-4(x - x_0)t_2 + s^2}{2\sqrt{2}st_2}\right)\right) \tag{5.8}$$

where A_1 and A_2 are the amplitudes, x_0 is the time zero, t_1 is the Gaussian pulse width, t_2 is the decay time constant, and s is the Gaussian buildup time. By using these fitting parameters, we can fit the time traces at K and K' valleys, and obtain the amplitudes A_1 and A_2. As described earlier, the amplitude A_2 corresponds to the incoherent processes from the photoexcited excitons, which is determined by the total number of created excitons and proportional to the fluence. By subtracting out this component from the data points taken at different fluences, the coherent components can be extracted and plotted as a function of pump fluence **(Fig 5.6)**.

5.6.3. Possible effects under red-detuned pumping

We remark on a possible observation of biexcitonic optical Stark effect under red-detuned optical driving. In the biexcitonic scheme **(Fig 5.7)**, the K'-valley is expected to upshift (downshift) if the red-detuning energy is smaller (larger) than the biexciton binding energy Δ_b. In our experiment, however, we could not reveal these complementary biexcitonic features due to multiple technical difficulties. According to our observation in the blue-detuned configuration, the biexcitonic optical Stark effect emerges only when the detuning energy is smaller than Δ_b. In the red-detuned configuration with such a small detuning energy, however, the scattering background from our pump pulses (spectral width ~35 meV) becomes rather significant and precludes us from detecting any signals of the optical Stark effect. Further research is merited to overcome these difficulties and reveal more details of the biexcitonic optical Stark effect in monolayer WS_2.

5.6.4. Fitting analysis

The sublinear dependence in **Fig 5.6** suggests that the small detuning limit has been reached in both valleys. In order to verify this, we performed fitting analysis for both valleys. Note that the optical transition between the ground state and the exciton states are affected by the shifts of the three states $|0\rangle$, $|x\rangle$ and $|x'\rangle$, as can be seen in **Fig 5.7**. Hence, the fluence dependences of the two valleys must be treated separately. At K valley, the $|0\rangle$ and $|x\rangle$ states are shifted symmetrically toward each other, leading to a *redshift* of the optical transition. At K' valley, the $|0\rangle$ and $|x'\rangle$ states are both shifted to a higher energy, but the magnitude of the $|0\rangle$ shift is observed to be much smaller than that of the $|x'\rangle$, hence can be neglected, leading to a *blueshift* of the optical transition.

The resulting shifts of the optical transitions can be expressed as $y_1 = -\left(\sqrt{a_1^2 + b_1 x} - a_1\right)$ for K valley, and $y_2 = \frac{1}{2}\left(\sqrt{a_2^2 + b_2 x} - a_2\right)$ for K' valley, where a_1, a_2 and b_1, b_2 are fitting parameters that represent the effective detunings and the transition matrix elements, respectively, and x is the pump fluence. Fitting curves using these expressions show excellent agreements with the fluence dependence data in **Fig 5.6**. The normalized and dimensionless fitting results give $a_1 \sim 0$, $b_1 = 0.038\ (\pm 0.006)$ for K

valley, and $a_2 = 0.48\ (\pm 0.21)$, $b_2 = 0.202\ (\pm 0.036)$ for K' valley. Note that these fitting parameters are obtained from data in Fig S4 that are normalized at each valley. Hence, their absolute values have only limited use. Nevertheless, we can still make meaningful comparison on their relative values within each valley, e.g. a_1 vs b_1, and a_2 vs b_2.

These fitting results have two important implications. First, it suggests that the detuning at K valley is effectively zero although the nominal detuning is 30 meV, resulting in a perfect square-root dependence with fluence. This seeming discrepancy is reasonable because, unlike in atomic systems, the energy levels in solids form a band of resonance. Here the pump pulse has a finite bandwidth of 35 meV and its center pump energy is located within the exciton linewidth of about 60 meV, hence a quasi-resonant condition may have already occurred. Secondly, the effective detuning at K' valley is found to be larger than that of the K valley. Nevertheless, the detuning term is still significantly smaller than the Rabi frequency term ($a_2^2 \ll b_2 x$), resulting in a majorly square-root fluence dependence. In this way, the intervalley biexciton is found to play significant roles in increasing the effective detuning by Δ_b and in enhancing the effective Rabi frequency. In fact, the effective moments can be roughly estimated from the fitting results, yielding $\mathcal{M} \sim 6$ Debye and $\mathcal{M}' \sim 140$ Debye, which shows that the effective Rabi frequency at K' valley is indeed much enhanced due to the intervalley biexcitons. This could be attributed to the effective self-consistent local field (described below).

These findings display a rare and fascinating interplay in the coherent light-matter interaction where now Coulomb interactions play a significant role. Previously, the optical Stark effect has been conveniently interpreted in terms of the well-established dressed-atom picture. This approach is proven suitable for excitons in monolayer TMDs at large detuning below resonance where contribution from Coulomb interaction is negligible [29, 30]. Despite the broad resemblance as it may seem, however, excitons are not atoms and their differences are most pronounced at small detuning limit, in the scale of biexciton binding energy [100], where many-body interactions in solids due to Coulomb interaction cannot be ignored. As pointed out in ref. [101], in addition to the applied field, the molecular field associated with the other excitons can combine to give an effective self-consistent local field. Therefore, it can be expected that the contribution of this molecular

field is significant when the pump photon energy is close to exciton resonance ($h\nu \sim E_0$). This gives rise to an optical Stark effect that is enhanced through the renormalized Rabi frequency, consistent with the observed effect at K' valley in our experiments. The situation is different from the far red-detuned experiment in previous works [29, 30] which give rise to a valley-selective optical Stark effect.

Chapter 6

Large, valley-exclusive Bloch-Siegert shift in monolayer WS_2

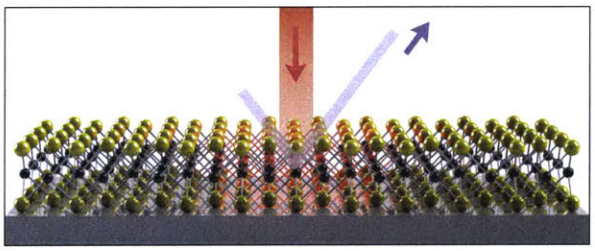

Contents[4]

[4] The work presented in this chapter is published in the following journal:
Edbert J. Sie, Chun Hung Lui, Yi-Hsien Lee, Liang Fu, Jing Kong, Nuh Gedik
***Science* 355**, 1066-1069 (2017)

Coherent interaction with off-resonance light can be used to shift the energy levels of atoms, molecules and solids. The dominant effect is the optical Stark shift, but there is an additional contribution from the so-called Bloch-Siegert shift that has eluded direct and exclusive observation so far, particularly in solids. We observe an exceptionally large Bloch-Siegert shift in monolayer WS_2 under infrared optical driving [102]. By controlling the light helicity, we can confine the Bloch-Siegert shift to occur only at one valley, and the optical Stark shift at the other valley, because the two effects are found to obey opposite selection rules at different valleys. Such a large and valley-exclusive Bloch-Siegert shift allows for enhanced control over the valleytronic properties of two-dimensional materials.

6.1. Bloch-Siegert shift

The fundamental interaction between light and matter can be understood within the framework of a two-level system with an energy splitting E_0 [52, 103]. Driving the system by off-resonance light of frequency $\hbar\omega < E_0$ produces a series of photon-dressed states (Floquet states) that are evenly spaced by $\hbar\omega$, where $\hbar$ is the reduced Planck's constant. In the first order, there are two pairs of photon-dressed states – one pair between the two original states **(Fig 6.1a)** and the other pair outside the original states **(Fig 6.1b)**. Interactions between the original states and these photon-dressed states can be understood in terms of state repulsion. The former case leads to a shift of transition energy called the optical Stark (OS) shift, which increases linearly with the light intensity ($\mathcal{E}_0^2$) and inversely with the detuning energy, $\Delta E_{\mathrm{OS}} \propto \mathcal{E}_0^2/(E_0 - \hbar\omega)$ [53]. The latter case also leads to a shift, called the Bloch-Siegert (BS) shift, which has a different energy dependence, $\Delta E_{\mathrm{BS}} \propto \mathcal{E}_0^2/(E_0 + \hbar\omega)$ [104]. Although the Bloch-Siegert shift is negligible at small detuning, at large detuning it can become comparable to the optical Stark shift.

The Bloch-Siegert shift has played an important role in atomic physics, notably for its manifestation as the Lamb shift in quantum electrodynamics [105, 106] and its contribution to the trapping potential for cold atoms [107]. In condensed matter physics, however, the Bloch-Siegert shift is a very rare finding because of its typically small magnitude (<1 μeV); so far it has been revealed only indirectly in artificial atoms by subtracting the dominant optical Stark shift using sophisticated modeling [108-110]. To

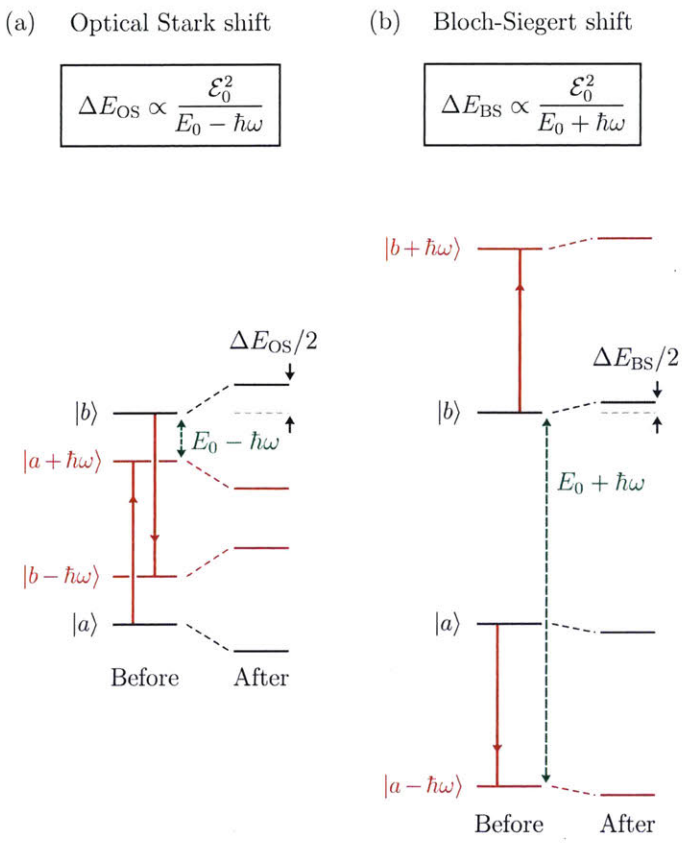

Figure 6.1: Comparison of the optical Stark shift and the Bloch-Siegert shift in a two-level system. **(a)** Energy diagram for optical Stark (OS) shift. $|a\rangle$ and $|b\rangle$ denote the two original states with resonance energy E_0 before they are optically driven. $|a + \hbar\omega\rangle$ and $|b - \hbar\omega\rangle$ are photon-dressed (Floquet) states driven by the co-rotating optical field. Hybridization between these Floquet and original states causes the resonance energy to blueshift by ΔE_{OS}, which is proportional to the light intensity ($\mathcal{E}_0^2$) and inversely proportional to ($E_0 - \hbar\omega$). **(b)** Energy diagram for Bloch-Siegert (BS) shift. $|a - \hbar\omega\rangle$ and $|b + \hbar\omega\rangle$ are two different Floquet states driven by the counter-rotating optical field. Hybridization between these Floquet and original states causes the Bloch-Siegert shift, with magnitude ΔE_{BS} inversely proportional to ($E_0 + \hbar\omega$).

elucidate the detailed characteristic of Bloch-Siegert shift, it is necessary to separate the two effects. Given that they are time-reversed partners of each other – the optical Stark shift arises from co-rotating field and the Bloch-Siegert shift from counter-rotating field – it is theoretically possible to separate them under stimulation that breaks time-reversal symmetry.

6.1.1. Semi-classical description

The energy shift that is induced by an off-resonance pump pulse can be obtained from the time-dependent perturbation theory, from which the optical Stark (OS) shift and the Bloch-Siegert (BS) shift usually appear together. In a small detuning case, the OS shift dominates and the BS shift only comes as a very small correction term that is often neglected. In a large detuning case, however, the BS shift can become comparable and it must be taken into account. Here, we derive the contribution of the BS shift at large detuning case and, by properly considering the matrix elements, we show that the BS shift also follows a selection rule but with helicity opposite to that of the OS shift. First, we will express the left-circularly polarized light (pump) in terms of the co-rotating and counter-rotating fields. Second, we consider the dipole approximation for the perturbation Hamiltonian and obtain the respective matrix elements at the K and K' valleys. Finally, we use the time-dependent perturbation theory to obtain the respective energy shift at the K and K' valleys

A left-circularly polarized light can be expressed as

$$\begin{aligned}\vec{\mathcal{E}}_{LCP} &= \mathcal{E}_0(\cos(kz-\omega t)\,\hat{x} + \sin(kz-\omega t)\,\hat{y}) \\ &= \mathcal{E}_0\left(\frac{1}{2}\left(e^{i\omega t}+e^{-i\omega t}\right)\hat{x} - \frac{1}{2i}\left(e^{i\omega t}-e^{-i\omega t}\right)\hat{y}\right) \\ &= \mathcal{E}_0\frac{1}{2}\left((\hat{x}-i\hat{y})e^{-i\omega t} + (\hat{x}+i\hat{y})e^{i\omega t}\right)\end{aligned} \tag{6.1}$$

where $\mathcal{E}_0$ and ω are the electric field amplitude and the angular frequency of the light. We have used $(z = 0)$ for monolayer material, and used the Euler's formula to obtain the final expression. The perturbation Hamiltonian that is induced by $\vec{\mathcal{E}}_{LCP}$ yields

$$H_{ab} = \langle b|e\vec{r}\cdot\vec{\mathcal{E}}_{LCP}|a\rangle = \frac{1}{2}e\mathcal{E}_0\langle b|(\vec{x}-i\vec{y})e^{-i\omega t} + (\vec{x}+i\vec{y})e^{i\omega t}|a\rangle \tag{6.2}$$

The outcome of this perturbation depends on the particular states $|a\rangle$ and $|b\rangle$. In monolayer WS_2, there are two optical transitions we can consider, one at the K valley $(\Delta m = -1)$ and one at the K' valley $(\Delta m = +1)$, and each of them obeys an opposite

selection rule with different helicities. At K valley, the non-zero matrix element is given by only the first term in the bracket $H_{ab}(K) = \frac{1}{2}e\mathcal{E}_0\langle b, K|(\vec{x} - i\vec{y})|a, K\rangle e^{-i\omega t}$. At K' valley, the non-zero matrix element is given by only the second term in the bracket $H_{ab}(K') = \frac{1}{2}e\mathcal{E}_0\langle b, K'|(\vec{x} + i\vec{y})|a, K'\rangle e^{i\omega t}$.

$$H_{ab}(K) = e^{-i\omega t}\mu_K\mathcal{E}_0/2 \tag{6.3}$$

$$H_{ab}(K') = e^{i\omega t}\mu_{K'}\mathcal{E}_0/2 \tag{6.4}$$

where $\mu_K = e\langle b, K|(\vec{x} - i\vec{y})|a, K\rangle$ and $\mu_{K'} = e\langle b, K'|(\vec{x} + i\vec{y})|a, K'\rangle$ are the dipole matrix elements at the two valleys, and they have equivalent magnitudes $|\mu_K| = |\mu_{K'}|$.

By using the resulting perturbation Hamiltonians, we can evaluate the induced energy shift of state $|a\rangle$ at the K valley through the standard time-dependent perturbation theory [56]

$$\begin{aligned}
\Delta E_a(t) &= H^*_{ba}(t)e^{-i\omega_0 t}\frac{1}{i\hbar}\int_0^t H_{ab}(t')e^{i\omega_0 t'}dt' \\
&= \left(e^{i\omega t}\mu_K\mathcal{E}_0/2\right)e^{-i\omega_0 t}\frac{1}{i\hbar}\int_0^t \left(e^{-i\omega t'}\mu^*_K\mathcal{E}_0/2\right)e^{i\omega_0 t'}dt' \\
&= \frac{1}{4}|\mu_K|^2{\mathcal{E}_0}^2e^{-i(\omega_0-\omega)t}\frac{1}{i\hbar}\int_0^t e^{i(\omega_0-\omega)t'}dt' \\
&= \frac{1}{4}|\mu_K|^2{\mathcal{E}_0}^2e^{-i(\omega_0-\omega)t}\frac{1}{i\hbar}\left[\frac{e^{i(\omega_0-\omega)t}-1}{i(\omega_0-\omega)}\right] \\
&= -\frac{|\mu_K|^2{\mathcal{E}_0}^2}{4\hbar}\left[\frac{1-e^{-i(\omega_0-\omega)t}}{(\omega_0-\omega)}\right]
\end{aligned} \tag{6.5}$$

where $\hbar\omega_0$ $(= E_0)$ is the energy gap. As it appears, the energy shift is time-dependent which oscillates at frequency $(\omega_0 - \omega)$. In practice, the energy shift should saturate at its mean value, which can be obtained from averaging through time $T \to \infty$, as follows

$$\begin{aligned}
\overline{\Delta E_a} &= \lim_{T\to\infty}\frac{1}{T}\int_0^T \Delta E_a(t)dt \\
&= -\frac{|\mu_K|^2{\mathcal{E}_0}^2}{4\hbar(\omega_0-\omega)}\lim_{T\to\infty}\frac{1}{T}\left[T - \left(\frac{e^{-i(\omega_0-\omega)T}-1}{-i(\omega_0-\omega)}\right)\right]
\end{aligned} \tag{6.6}$$

where the second term in the square bracket is oscillating around finite values, but this term eventually vanishes after it is divided by $T \to \infty$. Similar expression can be obtained for state $|b\rangle$ but with an opposite sign, $\overline{\Delta E}_b = -\overline{\Delta E}_a$. Hence, the gap between the two states at K valley becomes wider by an energy shift of

$$\overline{\Delta E}_K = \frac{|\mu_K|^2 {\mathcal{E}_0}^2}{4\hbar} \frac{1}{\omega_0 - \omega} \tag{6.7}$$

Similarly, we can also evaluate the induced energy shift at the K' valley

$$\begin{aligned}
\Delta E_a(t) &= H^*_{ba}(t) e^{-i\omega_0 t} \frac{1}{i\hbar} \int_0^t H_{ab}(t') e^{i\omega_0 t'} dt' \\
&= \left(e^{-i\omega t} \mu_{K'} \mathcal{E}_0/2\right) e^{-i\omega_0 t} \frac{1}{i\hbar} \int_0^t \left(e^{i\omega t'} \mu^*_{K'} \mathcal{E}_0/2\right) e^{i\omega_0 t'} dt' \\
&= \frac{1}{4} |\mu_{K'}|^2 {\mathcal{E}_0}^2 e^{-i(\omega_0+\omega)t} \frac{1}{i\hbar} \int_0^t e^{i(\omega_0+\omega)t'} dt' \\
&= \frac{1}{4} |\mu_{K'}|^2 {\mathcal{E}_0}^2 e^{-i(\omega_0+\omega)t} \frac{1}{i\hbar} \left[\frac{e^{i(\omega_0+\omega)t} - 1}{i(\omega_0 + \omega)}\right] \\
&= -\frac{|\mu_{K'}|^2 {\mathcal{E}_0}^2}{4\hbar} \left[\frac{1 - e^{-i(\omega_0+\omega)t}}{(\omega_0 + \omega)}\right]
\end{aligned} \tag{6.8}$$

The energy shift should also saturate at its mean value that can be obtained by a similar procedure earlier. Finally, the gap between the two states at K' valley becomes wider by an energy shift of

$$\overline{\Delta E}_{K'} = \frac{|\mu_{K'}|^2 {\mathcal{E}_0}^2}{4\hbar} \frac{1}{\omega_0 + \omega} \tag{6.9}$$

Note that the energy shifts at both valleys have a similar expression, but with different energy denominator, $(\omega_0 - \omega)$ at K valley and $(\omega_0 + \omega)$ at K' valley. The former energy shift corresponds to the ordinary optical Stark shift, while the latter energy shift corresponds to the Bloch-Siegert shift. By virtue of the valley selection rules, these two processes occur valley-exclusively at opposite valleys when induced by left-circularly polarize light (pump). That is, an ordinary optical Stark shift at K valley, and a Bloch-Siegert shift at K' valley.

6.1.2. Quantum-mechanical description

The interaction between a two-level system and light can be described by the interaction Hamiltonian $H_{int} = \boldsymbol{d} \cdot \boldsymbol{\mathcal{E}} = \frac{1}{2}\hbar g(\sigma^+ + \sigma^-)(a + a^\dagger)$, where g is the coupling constant. The total Hamiltonian yields

$$H = \frac{1}{2}\hbar\omega_0\sigma_z + \hbar\omega a^\dagger a + \frac{1}{2}\hbar g(\sigma^+ a + \sigma^- a^\dagger + \sigma^+ a^\dagger + \sigma^- a) \tag{6.10}$$

where the first term corresponds to the two-level system and the second term to the photon reservoir. In the interaction term, we have a combination of operators that involves an excitation (σ^+) or deexcitation (σ^-) of the two-level system, and an annihilation (a) or creation ($a^\dagger$) of photon. Among these, the first two terms conserve energy, ($\sigma^+ a + \sigma^- a^\dagger$), whereas the last two terms do not conserve energy, ($\sigma^+ a^\dagger + \sigma^- a$). These are the two processes that give rise to the "ordinary" optical Stark shift and the Bloch-Siegert shift of the energy resonance, respectively. In a two-level system that obeys the $\Delta m = 0$ selection rule and interacts with linearly polarized light, such as this one, the two processes cannot be separated. Thus, the two contributions should be considered together to obtain an accurate shift of the resonance, regardless of the choice of light polarization. At small detuning, the non-energy conserving term is negligible and therefore neglected in the so-called rotating wave approximation (RWA). This results in the original formulation of the Jaynes-Cummings model (JCM) that can be solved exactly [57]

$$H_{JCM} = \frac{1}{2}\hbar\omega_0\sigma_z + \hbar\omega a^\dagger a + \frac{1}{2}\hbar g(\sigma^+ a + \sigma^- a^\dagger) \tag{6.11}$$

Due to the interaction term, this Hamiltonian only couples states $|a, n+1\rangle$ and $|b, n\rangle$, which we can use as the basis for the Hamiltonian matrix

$$H_{JCM} = \hbar\omega\left(n + \frac{1}{2}\right)\begin{pmatrix} 1 & 0 \\ 0 & 1 \end{pmatrix} + \frac{\hbar}{2}\begin{pmatrix} \omega_0 - \omega & g\sqrt{n+1} \\ g\sqrt{n+1} & -(\omega_0 - \omega) \end{pmatrix} \tag{6.12}$$

This Hamiltonian matrix can be diagonalized to give the energies

$$E_{n,\pm} = \hbar\omega\left(n + \frac{1}{2}\right) \pm \frac{\hbar}{2}\sqrt{(\omega_0 - \omega)^2 + g^2(n+1)} \tag{6.13}$$

As can be seen, the energy level exhibits a shift, called the optical Stark shift. The shift of the $|a\rangle \rightarrow |b\rangle$ optical transition can also be evaluated, after taking a weak field approximation in which $g\sqrt{n+1} \ll \omega_0 - \omega$, giving

$$\Delta E_{JCM} = \frac{\hbar}{2}\frac{g^2(n+1)}{\omega_0 - \omega} \tag{6.14}$$

where $(n+1)$ is proportional to the light intensity $\langle \mathcal{E}^2 \rangle$, which means that the energy shift increases *linearly* with pump fluence at low fluence regime. The shift is inversely proportional to $\omega_0 - \omega$, and becomes very effective at small detuning.

In a two-level system that obeys the $\Delta m = \pm 1$ selection rules (monolayer WS_2), however, the choice of light polarization must be considered because it has distinct contributions [111]. This allows us to obtain exact solutions without the need to consider the RWA. The more general Hamiltonian can be expressed in terms of the canonical momentum $(\boldsymbol{p} - e\boldsymbol{A})$, where $\boldsymbol{A}$ is the vector potential, and this yields an interaction Hamiltonian

$$H_{int} = (e/2m)(\boldsymbol{A}\cdot\boldsymbol{p} + \boldsymbol{p}\cdot\boldsymbol{A}) + (e^2/2m)\boldsymbol{A}^2 \tag{6.15}$$

where we keep the first term and ignore the second (diamagnetic $\boldsymbol{A}^2$) term. The momentum operator $\boldsymbol{p}$ can be written in terms of Pauli matrices ($\sigma^{\pm}$), and evaluated for transition $\Delta m = \pm 1$ (at K or K' valley) using the usual Cartesian-to-spherical coordinates transformation, yielding

$$\boldsymbol{p}_{-1} = p(\hat{x} + i\hat{y})\sigma^+ + p^*(\hat{x} - i\hat{y})\sigma^- \tag{6.16}$$

$$\boldsymbol{p}_{+1} = p(\hat{x} - i\hat{y})\sigma^+ + p^*(\hat{x} + i\hat{y})\sigma^- \tag{6.17}$$

where $\hat{x}$ and $\hat{y}$ are unit vectors, and $p = \langle b|p_x|a\rangle$ is the dipole matrix element between the ground state $|a\rangle$ and the excited state $|b\rangle$. In our experiments, we use pump light with left-handed circular polarization that has the form of $\boldsymbol{A} \sim [(\hat{x} - i\hat{y})a_- + (\hat{x} - i\hat{y})^* a_-^\dagger]$, where a_-

and $a_{-}^{\dagger}$ are the annihilation and creation operators for left-handed photon. Hence, we can evaluate the interaction Hamiltonian at K ($\Delta m = -1$) and K' ($\Delta m = +1$) valleys separately

$$H_{int}(K) = (e/m)\boldsymbol{A} \cdot \boldsymbol{p}_{-1} = \hbar g(\sigma^{+}a_{-} + \sigma^{-}a_{-}^{\dagger})/2 \tag{6.18}$$

$$H_{int}(K') = (e/m)\boldsymbol{A} \cdot \boldsymbol{p}_{+1} = \hbar g(\sigma^{+}a_{-}^{\dagger} + \sigma^{-}a_{-})/2 \tag{6.19}$$

The total Hamiltonian at respective valleys can then be written

$$H(K) = \frac{1}{2}\hbar\omega_0\sigma_z + \hbar\omega a_{-}^{\dagger}a_{-} + \frac{1}{2}\hbar g(\sigma^{+}a_{-} + \sigma^{-}a_{-}^{\dagger}) \tag{6.20}$$

$$H(K') = \frac{1}{2}\hbar\omega_0\sigma_z + \hbar\omega a_{-}^{\dagger}a_{-} + \frac{1}{2}\hbar g(\sigma^{+}a_{-}^{\dagger} + \sigma^{-}a_{-}) \tag{6.21}$$

where the energy-conserving interaction term now appears at K valley, while the non energy-conserving term appears at K' valley. The Hamiltonian at K valley has the same form with the exactly solvable JCM, and it gives rise to the "ordinary" optical Stark shift of the energy resonance as shown earlier. Meanwhile, the Hamiltonian at K' valley can also be solved exactly. This Hamiltonian only couples states $|a, n-1\rangle$ and $|b, n\rangle$, where $|n\rangle$ is the number of left-handed photons, and we can use these two states as the basis for the Hamiltonian matrix

$$H_{K'} = \hbar\omega\left(n - \frac{1}{2}\right)\begin{pmatrix}1 & 0\\ 0 & 1\end{pmatrix} + \frac{\hbar}{2}\begin{pmatrix}\omega_0 + \omega & g\sqrt{n}\\ g\sqrt{n} & -(\omega_0 + \omega)\end{pmatrix} \tag{6.22}$$

This Hamiltonian matrix can be diagonalized to obtain a set of dressed states with energies

$$E_{n,\pm} = \hbar\omega\left(n - \frac{1}{2}\right) \pm \frac{\hbar}{2}\sqrt{(\omega_0 + \omega)^2 + g^2 n} \tag{6.23}$$

At low pump fluence, the shift of the energy gap can be evaluated in a simpler form after taking a weak field approximation, $g\sqrt{n} \ll \omega_0 + \omega$, yielding

$$\Delta E_{K'} = \frac{\hbar}{2}\frac{g^2 n}{\omega_0 + \omega} \tag{6.24}$$

where n is proportional to the light intensity $\langle \mathcal{E}^2 \rangle$. This is the Bloch-Siegert shift, and there are three factors that govern the magnitude. First, the coupling constant g contains a dipole matrix element that requires an angular momentum change of $\Delta m = +1$. Second, the photon number $n \propto \langle \mathcal{E}^2 \rangle$ means that the energy shift increases *linearly* with pump fluence at low fluence regime. Third, the shift is inversely proportional to $\omega_0 + \omega$, and becomes more effective at pumping with lower photon energies. This is the reason why this shift can be observed more clearly using intense pump fluence at the infrared.

6.2. Experimental methods

In our experiment, we investigate high-quality WS_2 monolayers grown by chemical vapor deposition (CVD) on sapphire substrates [10, 11]. We employ femtosecond pump-probe absorption spectroscopy at ambient conditions. To reveal the Bloch-Siegert shift, we pump the samples with strong infrared pulses at $\hbar\omega = 0.59 - 0.98$ eV, far below the exciton resonance ($E_0 = 2.0$ eV). The induced exciton shift is probed by the reflection of synchronized broadband pulses in the visible range (1.83 – 2.17 eV), from which we can extract the absorption change. A blueshift of the exciton absorption peak (α) is manifested as a differential curve in the absorption change $\Delta\alpha$ **(Fig 6.2c)**. From this, we can deduce the magnitude of the energy shift. In our experiment, we used pump fluence of up to 800 μJ/cm^2 with pulsewidth of 160 fs. This gives the peak intensity of I = fluence/pulsewidth $= \epsilon_0 c \mathcal{E}_0^2/2$, from which we can determine the peak intensity to be $I = 5$ GW/cm^2 and the electric field strength to be $\mathcal{E}_0 = 2$ MV/cm.

6.3. Observation of the Bloch-Siegert shift

We report on the observation of a large Bloch-Siegert shift ($\Delta E_{\mathrm{BS}} \sim 10$ meV), which can be entirely separated from the optical Stark shift. Such a large and exclusive Bloch-Siegert shift is realized in a monolayer of transition-metal dichalcogenide (TMD) tungsten disulfide (WS_2). This is possible because this material system possesses two distinctive features. First, it exhibits strong light-exciton interaction at the two time-reversed valleys (K, K') in the Brillouin zone **(Fig 6.2, a-c)** [6, 13, 71]. Secondly, the two valleys possess finite and opposite Berry curvature owing to the lack of inversion symmetry, giving rise to

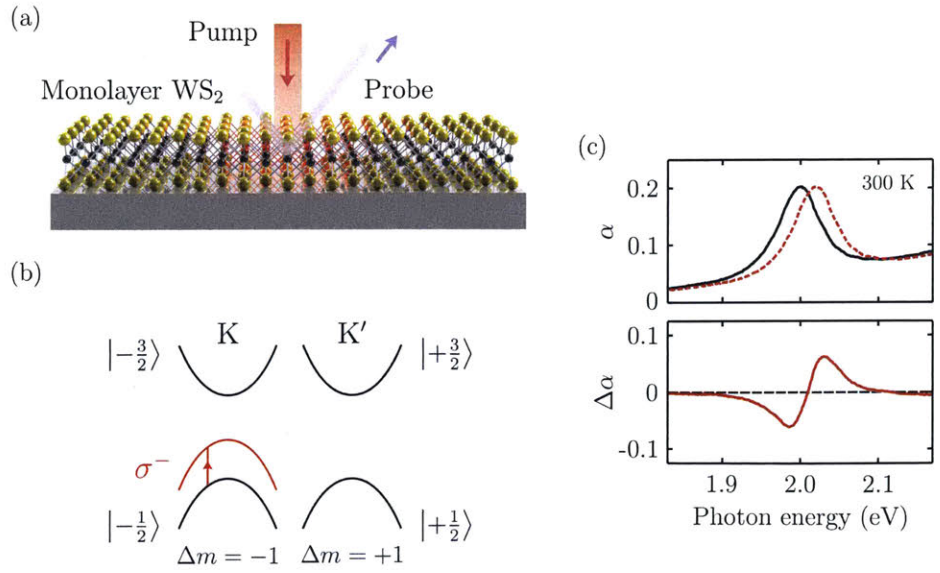

Figure 6.2: Observation of valley-exclusive Bloch-Siegert shift in monolayer WS_2. **(a)** Illustration of the pump-probe experiment. We pump the monolayer WS_2 sample with strong infrared pulses, and measure the pump-induced change of reflection with broadband probe pulses. **(b)** The K and K' valleys in monolayer WS_2. Optical pumping with left-handed circular polarization (σ^-) couples only to the K valley, and not the K' valley, unless the counter-rotating field is taken into account. **(c)** Measured A exciton absorption spectrum (α, black curve in the top panel) of monolayer WS_2 in equilibrium. The dashed curve represents the shifted resonance (simulated) under red-detuned optical pumping. This shift produces a differential curve in the absorption change ($\Delta\alpha$, red curve in the bottom panel).

distinct optical selection rules and related valleytronic properties [15, 18-20, 27, 28, 91, 112, 113]. That is, the optical transition at the K (K') valley is coupled exclusively to left-handed σ^- (right-handed σ^+) circularly polarized light. Such a unique material platform allows us to separate the Bloch-Siegert shift from the optical Stark shift by using circularly polarized light.

We employ femtosecond pump-probe absorption spectroscopy in our experiment **(Fig 6.2a)**. All measurements were carried out at room temperature. We pump a monolayer of WS_2 with intense σ^- infrared light pulses and probe the energy shift at the K (K') valley with σ^- (σ^+) visible light pulses. A blueshift of the exciton absorption peak (α) is manifested as a differential curve in the absorption change $\Delta\alpha$ **(Fig 6.2c)**. From this, we can deduce the magnitude of the energy shift at both valleys. Previously, transient absorption

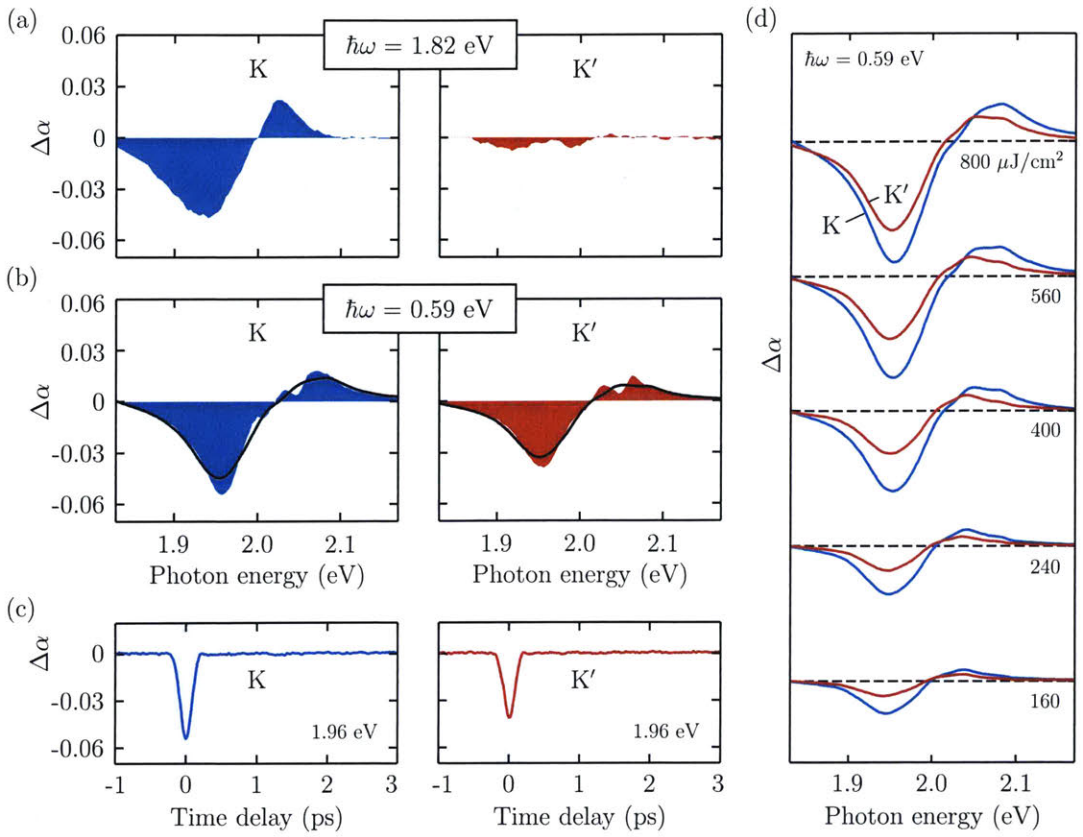

Figure 6.3: (a-b) The $\Delta\alpha$ spectra under zero-delay optical pumping at pump photon energy 1.82 and 0.59 eV. By using probe pulses with σ^- (σ^+) polarization, we can selectively measure $\Delta\alpha$ at the K (K') valley, as shown in the left (right) column. The black curves in (E) are smoothened curves to average out the modulations, see text. **(c)** Time trace of $\Delta\alpha$ spectra in (E) measured at probe energy of 1.96 eV and pump energy of 0.59 eV. The induced energy shift is observed only at zero time delay. **(d)** The zero-delay $\Delta\alpha$ spectra of the K valley (blue curves) and K' valley (red curves) under different incident pump fluence ($\mathcal{F}$ = 160 – 800 μJ/cm²). The pump photon energy is 0.59 eV. The spectra are vertically displaced for clarity.

with visible pumping has been used to study the optical Stark effect in monolayer TMDs [29, 30]. Here, by pumping with infrared light, we reveal the Bloch-Siegert shift in WS_2.

Figure 6.3, a-d display our results at the K valley (blue curve) and K' valley (red curve). For comparison, we first show the $\Delta\alpha$ spectra under zero-delay pumping at $\hbar\omega$ = 1.82 eV **(Fig 6.3a)**. For this small detuning energy, only the K valley shows an appreciable $\Delta\alpha$ signal. This signal arises from the optical Stark shift, which occurs exclusively at the K valley [29, 30]. The K' valley exhibits only very weak (but observable) signal. However, as we lower the pumping photon energy to 0.59 eV, the signal at the K' valley becomes comparable to the signal at the K valley **(Fig 6.3b)**. This observation indicates a

pronounced energy blueshift at the K' valley, a phenomenon that apparently violates the well-established valley selection rules in monolayer TMDs. Some modulations also appear in the $\Delta\alpha$ spectrum. These minor features are possibly induced by electron-phonon coupling and warrant further investigation; here we average out these modulations by smoothening the curves (black lines). We have further examined the signals at different pump-probe time delays. The $\Delta\alpha$ signals at both valleys emerge only at zero time delay, with very similar temporal profiles to the 160 fs duration of the pump pulses **(Fig 6.3c)**. These results indicate the coherent nature of the energy shift, and also exclude the influence of intervalley scattering of possible excited carriers that typically occurs on the picosecond time scale [26, 37, 72].

6.4. Fluence & detuning dependences

To investigate the underlying mechanism of the anomalous energy shift at K' valley, we have measured the zero-delay $\Delta\alpha$ spectra for both valleys at various pump photon energies ($\hbar\omega$ = 0.59, 0.69, 0.89, 0.98 eV) and different pump fluences ($\mathcal{F}$ = 30 – 800 μJ/cm^2). Here we display the fluence-dependent spectra for pump photon energy $\hbar\omega$ = 0.59 eV **(Fig 6.3d)**. The $\Delta\alpha$ spectra at both valleys are found to grow with increasing pump fluence. For a more quantitative analysis, we have extracted the energy shift from each spectrum, and plotted it as a function of $\mathcal{F}/(E_0 - \hbar\omega)$ **(Fig 6.4a)**. The shift at K valley exhibits an excellent linear dependence regardless of the different pump photon energies (closed symbols), indicating that it arises from the optical Stark effect. The shift at K' valley, however, spreads out with no rigorous linear dependence (open symbols). Such a contrasting behavior indicates that the K'-valley shift does not arise from the optical Stark effect. In **Figure 6.4b**, we replot the K'-valley shift as a function of $\mathcal{F}/(E_0 + \hbar\omega)$ with the same axes scales; the data now exhibit an excellent linear dependence. Moreover, the slope of the K'-valley shift in this new plot is identical to the slope of the K-valley shift in **(Fig 6.4a)**. This observation strongly suggests that the K'-valley shift arises from the Bloch-Siegert effect.

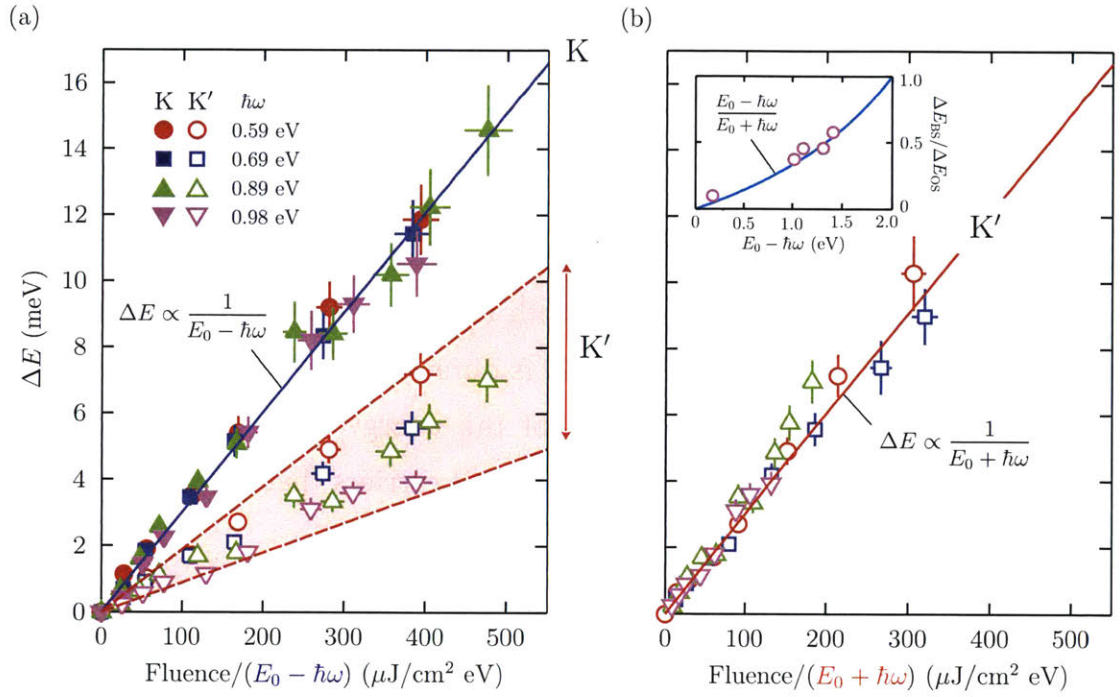

Figure 6.4: Fluence and detuning dependences of the Bloch-Siegert shift. **(a)** Energy shifts at the K and K' valleys (closed and open symbols) as a function of Fluence/$(E_0 - \hbar\omega)$. The data are extracted from the $\Delta\alpha$ spectra in Fig 6.3. The K-valley shift exhibits a rigorous linear dependence (solid blue line), but the K'-valley shift spreads out (red region). **(b)** Energy shift at K' valley as in (A), but plotted as a function of Fluence/$(E_0 + \hbar\omega)$. The linear dependence becomes obvious. The top-left inset shows the predicted ratio $\Delta E_{BS}/\Delta E_{OS}$ (blue line) when the detuning energy $(E_0 - \hbar\omega)$ increases from zero to the resonant energy ($E_0 = 2$ eV for monolayer WS_2). The open circles are our averaged experimental data obtained from Fig 6.3.

6.5. Valley-exclusive Optical Stark shift & Bloch-Siegert shift

Our finding can be verified quantitatively by using either a semi-classical theory or a fully quantum-mechanical theory [111] (Section 6.1). As we probe only the lowest-energy exciton state (1s), which shows similar properties as those of hydrogen atoms, it is appropriate and sufficient to use a simple two-level framework, as shown in earlier studies [6, 18, 29, 30]. In our semi-classical analysis, we treat the ground state and the 1s exciton state as the two-level system ($|a\rangle$ and $|b\rangle$) with a resonance energy E_0, driven by a classical electromagnetic wave with amplitude $\mathcal{E}_0$ and frequency ω. We use a left-circularly polarized pump beam $\vec{\mathcal{E}}(t) = \mathcal{E}_0(\cos(kz - \omega t)\,\hat{x} + \sin(kz - \omega t)\,\hat{y})$, polarized along the xy-plane of the monolayer sample ($z = 0$), which can also be expressed as:

$$\vec{\mathcal{E}}(t) = \frac{1}{2}\mathcal{E}_0\left[(\hat{x} - i\hat{y})e^{-i\omega t} + (\hat{x} + i\hat{y})e^{i\omega t}\right] \tag{6.25}$$

where the field is decomposed into two terms based on their time-evolution. The interaction Hamiltonian can then be expressed as

$$H_{ab} = \langle b|e\vec{\mathcal{E}} \cdot \vec{r}|a\rangle = \frac{1}{2}e\mathcal{E}_0\langle b|(\vec{x} - i\vec{y})e^{-i\omega t} + (\vec{x} + i\vec{y})e^{i\omega t}|a\rangle \tag{6.26}$$

Here the first term $(\vec{x} - i\vec{y})e^{-i\omega t}$ induces a transition with $\Delta m = -1$ (co-rotating field), and the second term $(\vec{x} + i\vec{y})e^{i\omega t}$ induces a transition with $\Delta m = +1$ (counter-rotating field). Owing to the unique valley selection rules in monolayer WS_2, these two terms are thus coupled exclusively to the K ($\Delta m = -1$) and K' ($\Delta m = +1$) valleys, respectively **(Fig 6.5, a and b)**, with their valley-specific interactions as:

$$H_{ab}(K) = e^{-i\omega t}\mu_K\mathcal{E}_0/2 \tag{6.27}$$

$$H_{ab}(K') = e^{i\omega t}\mu_{K'}\mathcal{E}_0/2 \tag{6.28}$$

Here μ_K and $\mu_{K'}$ are the dipole matrix elements at the K and K' valley, respectively, and they have equal magnitudes $\mu = |\mu_K| = |\mu_{K'}|$. However, they are associated with opposite time-evolution factors, which leads to a more general theory of valley selection rules in monolayer TMDs. Under resonant absorption condition ($\hbar\omega = E_0$), the left-circularly polarized light couples only to the K-valley. But under off-resonance condition ($\hbar\omega < E_0$), the coupling to the K'-valley can become appreciable through the time-reversed process, giving rise to noticeable energy shift. The induced energy shifts at the respective valleys can be evaluated by the time-dependent perturbation theory as:

$$\Delta E_K = \frac{\mu^2\mathcal{E}_0^2}{2}\frac{1}{E_0 - \hbar\omega} \tag{6.29}$$

$$\Delta E_{K'} = \frac{\mu^2\mathcal{E}_0^2}{2}\frac{1}{E_0 + \hbar\omega} \tag{6.30}$$

The two energy shifts have different energy dependence, from which we can readily identify ΔE_K to be the optical Stark shift and $\Delta E_{K'}$ the Bloch-Siegert shift. When plotted as a function of their respective energy denominator ($E_0 - \hbar\omega$, or $E_0 + \hbar\omega$), both shifts exhibit

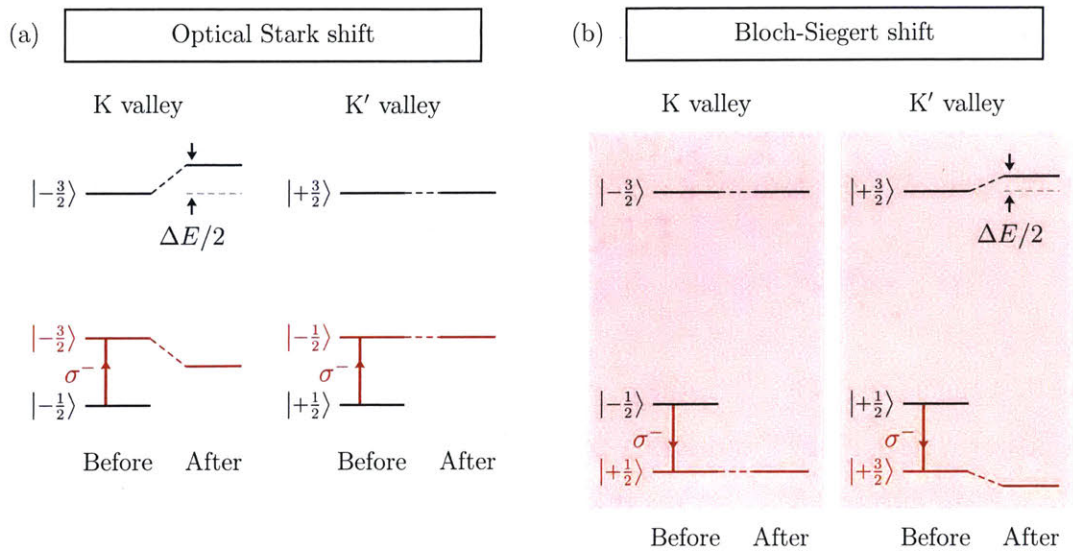

Figure 6.5: (a) Energy diagram before and after optical pumping for the optical Stark shift, which occurs only at the K valley. **(b)** Energy diagram for the Bloch-Siegert shift, which occurs only at the K′ valley.

an identical slope. The prediction of common slope and opposite valley indices agrees well with our experimental observation **(Fig 6.4, a-b)**. From our data, we can deduce the dipole matrix elements to be μ = 55 Debye, in excellent agreement with previous measurements [29]. In addition, the ratio between $\Delta E_{K'}$ and ΔE_K is predicted to be $(E_0 - \hbar\omega)/(E_0 + \hbar\omega)$, the same as $\Delta E_{\mathrm{BS}}/\Delta E_{\mathrm{OS}}$ for a two-level system with no valley degree of freedom that we discussed earlier. By plotting the average shift ratio measured for each pump photon energy, we find a good agreement between our experiment and theory **(Fig 6.4b, inset)**.

The physics of this valley-exclusive energy shift can be illustrated in the energy diagrams shown in **Fig 6.5, a-b**. The co-rotating field generates a Floquet state $\hbar\omega$ above the ground state in both valleys, with energy separation $E_0 - \hbar\omega$ from the excited state. Due to the matching condition of angular momentum, repulsion between the Floquet state and the excited state only occurs at the K valley, giving rise to the ordinary optical Stark shift **(Fig 6.5a)**. On the other hand, the counter-rotating field generates a Floquet state $\hbar\omega$ below the ground state, with energy separation $E_0 + \hbar\omega$ from the excited state **(Fig 6.5b)**. The matching condition of angular momentum forbids the level repulsion at the K valley but allows it at the K′ valley. This gives rise to the Bloch-Siegert shift at the opposite (K′)

valley. In other words, the left-circularly polarized light can be understood as stimulating the σ^- absorption ($\Delta m = -1$) and σ^- emission ($\Delta m = +1$) processes at the K and K' valleys, respectively. This makes it possible for the circularly polarized light with a given helicity to couple to both valleys in a distinct manner, thus enriching the valley selection rules.

6.6. Conclusions

The Bloch-Siegert shift we observed exhibits the opposite valley selection rules from the ordinary optical Stark effect, which allows us to completely separate the two effects. This is possible because, as time-reversed partners, the two effects share similar relationship with the two time-reversed valleys in monolayer WS_2, which can be disentangled under circularly polarized light that breaks the time-reversal symmetry. Our finding reveals more general valley selection rules and promises enhanced control over the valleytronic properties of Dirac materials, such as graphene, TMDs, as well as Weyl semimetals. Furthermore, by using higher pump intensity or lower pump photon energy with selective light helicity, we expect to reveal higher-order coherent effects that could produce polarized valley current in transport experiments [114].

Chapter 7

Lennard-Jones-like potential of 2D excitons in monolayer WS_2

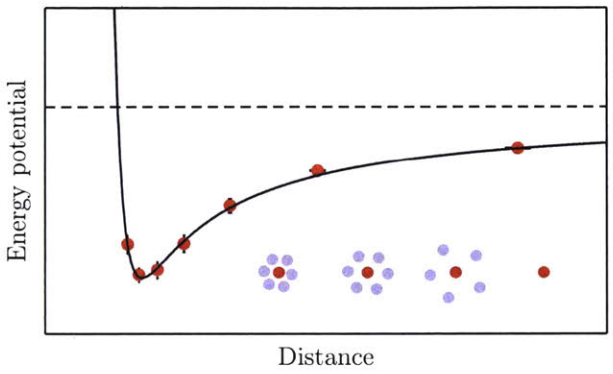

Contents[5]

[5] The work presented in this chapter is currently under review:
E. J. Sie, A. Steinhoff, C. Gies, C. H. Lui, Q. Ma, M. Rösner, G. Schönhoff, F. Jahnke, T. O. Wehling, Y.-H. Lee, J. Kong, P. Jarillo-Herrero, N. Gedik

In this chapter, we report a rare atom-like interaction between excitons in monolayer WS_2, measured using ultrafast absorption spectroscopy. At increasing excitation density, the exciton resonance energy exhibits a pronounced redshift followed by an anomalous blueshift. Using both material-realistic computation and phenomenological modeling, we attribute this observation to plasma effects and an attraction-repulsion crossover of the exciton-exciton interaction that mimics the Lennard-Jones potential between atoms. Our experiment demonstrates a strong analogy between excitons and atoms with respect to inter-particle interaction, which holds promise to pursue the predicted liquid and crystalline phases of excitons in two-dimensional materials.

7.1. Many-body interactions in 2D TMDs

Excitons in semiconductors are often perceived as the solid-state analogs to hydrogen atoms. This analogy helps us to understand the basic features of excitons, notably their internal energy states. However, this analogy breaks down as we consider the inter-particle interactions because of some fundamental differences between atoms and excitons. Atoms are stable particles with large ionization energy (~10 eV). They exhibit long-range van der Waals attraction and short-range Pauli repulsion, which form the so-called Lennard-Jones potential as a function of interatomic separation [115, 116]. In contrast, excitons are transient quasiparticles with much smaller binding energy and extremely short lifetime. They can dissociate into an electron-hole plasma, whose relative concentration is governed by the law of mass action [117, 118]. Hence, interactions in semiconductors are somewhat different from those in real gases, because the effects from plasma [88] and excitons [119] must be considered. The relative importance of exciton and plasma effects depends on the regime of excitation density. In conventional III-V and II-VI semiconductors, such complex many-body effects preclude the demonstration of atom-like interactions between excitons, particularly in the regime of high excitation density where excitons become unstable.

Recent advances in two-dimensional (2D) semiconductors, particularly monolayer transition-metal dichalcogenides (TMDs), offer a unique platform to investigate excitonic interactions. These materials possess strong Coulomb interactions due to quantum

confinement and reduced dielectric screening [13], leading to the formation of excitons with exceptionally large binding energies ~300 meV [6, 31, 32, 120]. The enhanced stability of excitons in these materials provides good opportunities to reexamine the role of plasma effects and excitonic interactions over a broad range of excitation density. Although the exciton physics in photoexcited TMDs has been much studied [26, 37, 87, 121-123], a complete picture of excitonic interactions in these materials is still lacking.

Here we investigate systematically the many-particle interactions in monolayer WS_2. We combine ultrafast absorption spectroscopy, microscopic many-body theory and an analytic approach that maps the measured exciton-exciton interactions onto an effective atomic model. In particular, we measure the absorption spectrum of the A exciton under femtosecond optical excitation. As we increase the excitation density, we observe a pronounced redshift (73 meV) of the exciton resonance energy at low density, followed by an unusual blueshift (10 meV) at high density. We attribute the two different energy shifts to two distinct interaction regimes. At high density, the exciton blueshift is well described by assuming a repulsive exciton-exciton interaction similar to the short-range Lennard-Jones interaction between atoms [115, 116]. At low density, the Lennard-Jones potential further contains a long-range contribution due to an attractive exciton-exciton interaction. However, in contrast to the atomic case, the exciton redshift in this regime is found to follow a strongly modified exponent, indicating that not all carriers are bound excitons but a fraction exists as electron-hole plasma. Insight from microscopic theory reveals that the redshift observed at low excitation density mainly arises from plasma-induced bandgap renormalization and screening of the exciton binding energy. We note that the observed energy shift is much larger than those reported in conventional semiconductors such as GaAs quantum wells (~0.1 meV) [124-128] as a consequence of the much enhanced many-body interactions in the 2D material. Our model is further supported by the temperature dependent exciton energy shift observed in the time-resolved absorption measurements.

7.2. Experimental methods

The sample consists of high-quality monolayers of WS_2 that were grown on sapphire substrates by chemical vapor deposition (CVD) [10, 11]. All measurements in this study

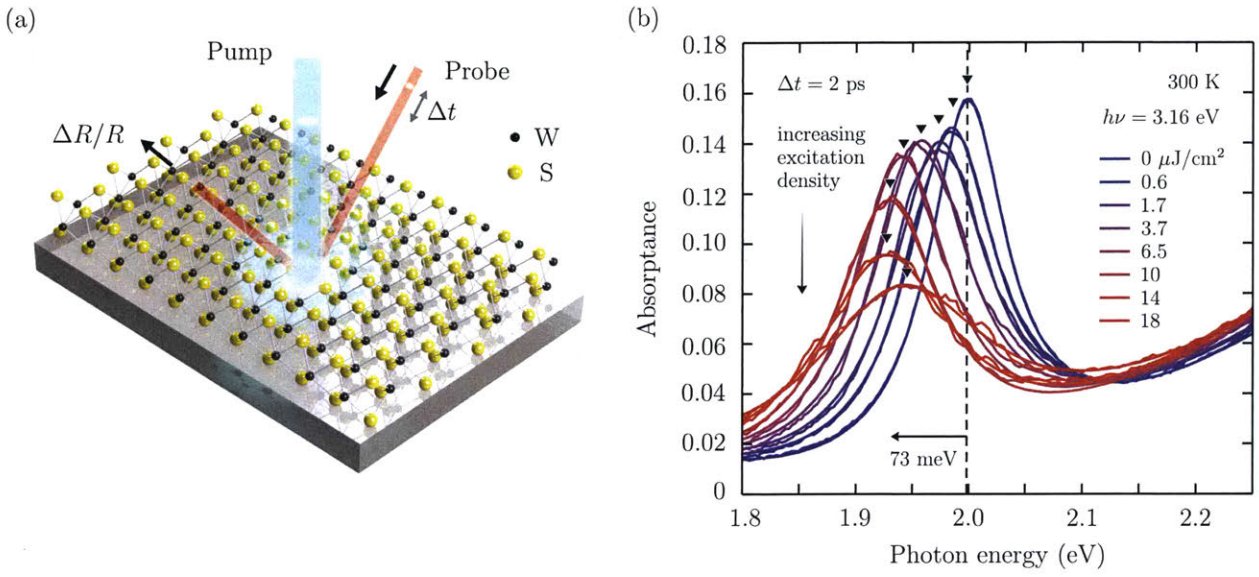

Figure 7.1: (a) Schematic of transient absorption spectroscopy setup. **(b)** Absorption peak of A exciton in monolayer WS_2 at increasing excitation densities.

were conducted at ambient condition (300 K, 1 atm). In our experiments, we used a Ti:sapphire amplifier producing laser pulses with duration of 50 fs and at 30 kHz repetition rate. Each pulse was split into two arms. For the pump arm, the pulses were sent to a second-harmonic nonlinear crystal, while for the probe arm the pulses were sent through a delay stage and a white-light continuum generator ($h\nu$ = 1.78-2.48 eV, chirp-corrected). The two beams were focused at the sample, and the probe beam was reflected to a monochromator and a photodiode for lock-in detection [26, 29]. By scanning the grating and the delay stage, we were able to measure $\Delta R/R$ (and hence α, [26]) as a function of energy and time delay.

In our pump-probe experiment, we generate carriers by femtosecond pump pulses with photon energy $h\nu$ = 3.16 eV, which is above the quasiparticle bandgap at around 2.3 eV at room temperature [6]. The resulting A exciton resonance near E_A = 2.0 eV is monitored through the reflection spectrum of broadband probe pulses with controlled time delay at room temperature **(Fig 7.1a)**. For a monolayer sample on a transparent substrate, the absorption spectrum can be extracted from the reflection spectrum using thin-film approximation (see Chapter 2, Section 2.2). We estimate the excitation density n from the

measured incident pump fluence and absorbance of the sample at the excitation wavelength [81].

7.3. Optical signature of many-body effects

Figure 7.1b shows the absorption spectra of the A exciton at increasing pump fluence up to 18 μJ/cm^2 ($n = 5.3\times10^{12}$ cm^{-2}). The spectra were taken at a pump-probe delay of 2 ps, a time after which the excitons are expected to have reached thermal equilibrium with one another and with the lattice but not yet recombined [129, 130]. All the spectra can be fitted well with a Lorentzian function plus a second-order polynomial function (smooth lines over the data curves), which represent the exciton peak and the background slope respectively:

$$\alpha(\omega) = I_0\left(\frac{g_0}{\pi((\omega-\omega_0)^2+g_0^2)}\right) + (A + B(\omega-\omega_1) + C(\omega-\omega_1)^2) \qquad (7.1)$$

Here, I_0, ω_0 and g_0 are the absorption peak intensity, energy and linewidth respectively, while A, B, C and ω_1 are the background constants and energy reference respectively. We first use this expression to fit the *equilibrium* absorption spectrum and record the fitting parameters. The obtained background parameters are fixed for subsequent fitting procedures in fluence-dependent and time-dependent spectra, and only the Lorentzian function parameters (I_0, ω_0 and g_0) are allowed to vary. We note that the B exciton is well separated from the A exciton by 400 meV in monolayer WS_2 [81], and therefore does not affect our analysis. From the fitting, we extract the exciton peak energy (E_A), linewidth (Γ), peak intensity (I) and spectral weight (S, i.e. the integrated area), and plot their changes in **Fig 7.2a-c**. While the spectral weight remains unchanged at all excitation densities, the other quantities vary significantly with the density.

7.3.1. Exciton redshift-blueshift crossover

These quantities exhibit two distinct behaviors at low and high excitation densities. At low density, the peak energy redshifts gradually for ~70 meV as the density increases, while the linewidth and peak intensity remain almost constant. The energy shift cannot be explained using the pump-induced lattice heating because the estimated lattice

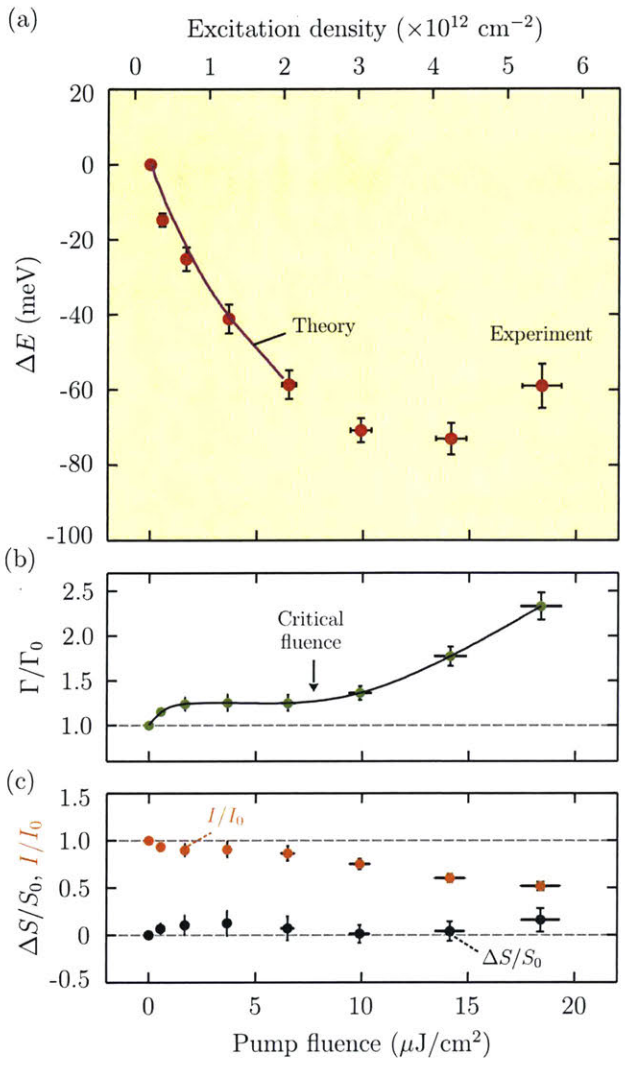

Figure 7.2: (a) Exciton energy shift (ΔE) as a function of pump fluence obtained from the experiment (red) and calculation (purple). **(b)** Linewidth broadening ($\Delta\Gamma/\Gamma_0$), **(c)** peak height (I/I_0) and spectral weight change ($\Delta S/S_0$).

temperature increase is ~20 K, which corresponds to merely ~4 meV of temperature dependent gap narrowing [131]. In contrast, with further increase of density $n > 2.0\times10^{12}$ cm^{-2}, the rate of exciton redshift diminishes and eventually turns into a blueshift of ~10 meV from the lowest energy point. Notably, the redshift-blueshift crossover is accompanied by a large spectral broadening, with the linewidth increasing to more than twice of the initial width **(Fig 2b)**. Correspondingly, the peak intensity drops to one half of the initial intensity to maintain the total spectral weight of the A exciton **(Fig 2c)**. These two distinct

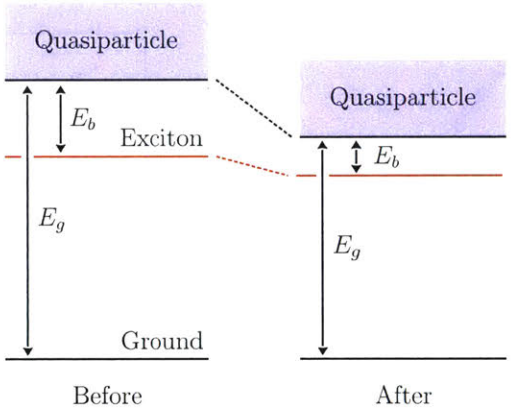

Figure 7.3: Schematic band diagram showing that the ΔE results from an incomplete compensation between the gap narrowing and the exciton binding energy reduction.

energy shifts correspond to two different interaction regimes as we will discuss in the following.

7.3.2. At low density: plasma contribution

We first discuss the redshift at low density. According to prior studies in monolayer TMDs [88], the exciton redshift can be ascribed to a combination of bandgap renormalization and plasma screening of the exciton binding energy due to the excited unbound carriers **(Fig 7.3)**. We have obtained the quasiparticle band structure and Coulomb matrix elements of monolayer WS_2 by first-principle G_0W_0 calculations. Screening from the substrate is additionally incorporated in the Coulomb matrix elements [132]. The exciton shift due to the excited carriers is calculated with microscopic semiconductor Bloch equations in a screened-exchange Coulomb-hole approximation (SXCH) – see Section 7.7.1. With increasing excitation density, both the quasiparticle band gap (E_g) and the exciton binding energy (E_b) are found to decrease **(Fig 7.4a)**. Since E_g decreases faster than E_b, the resulting exciton resonance energy ($E_A = E_g - E_b$) shifts to lower energies **(Fig 7.4b)**.

Our calculations reproduce the measured redshift at low density (**Fig 7.2a**, purple curve). The overall agreement is remarkable, given that we do not use any fitting parameter in our theory. We note that the SXCH calculation predicts a Mott transition at $n = 2\times10^{12}$ cm^{-2}. Approximately at this density, the experimental data reveals a crossover

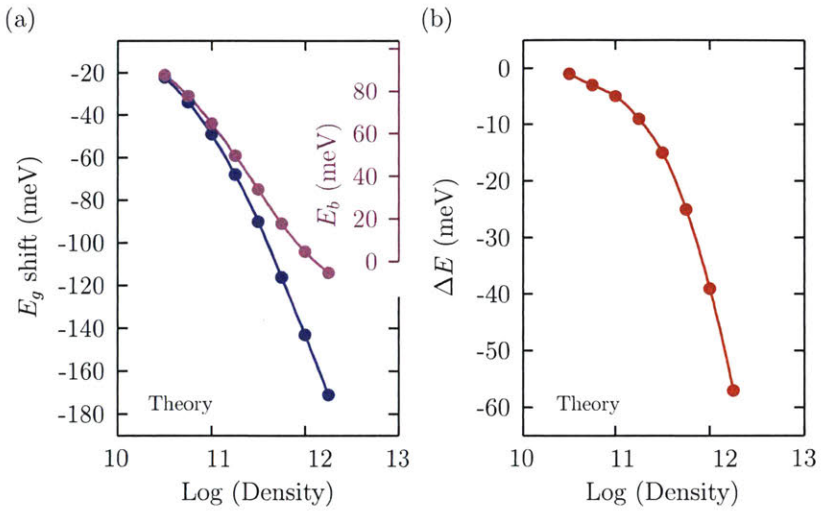

Figure 7.4: (a) Theoretical results on the gap narrowing (ΔE_g) and the exciton binding energy (E_b) at increasing exciton density (logscale). **(b)** Resulting exciton shift ΔE at increasing density (logscale).

into an anomalous blueshift **(Fig 7.2a)**, which we attribute to exciton-exciton interaction that is facilitated by the increasing fraction of carriers bound into excitons and which marks the limit in carrier density to which a plasma picture applies. Although the observed redshift at low density is dominated by plasma contribution, in a purely excitonic picture a redshift can also result from exciton-exciton attraction similar to atoms. Mutual attraction can reduce the energy cost to create an extra exciton (E_A) by a magnitude as much as the negative inter-exciton potential energy.

7.3.3. At high density: exciton contribution

In light of the purely excitonic picture, we interpret the blueshift at high density > 8 uJ/cm^2 ($n > 2.0\times10^{12}$ cm^{-2}), where a large fraction of carriers form bound excitons, as arising from an exciton-exciton *repulsion*. Indeed, the blueshift is not captured by our numerical approach, and therefore suggests a new contribution other than the plasma effects. The simultaneous broadening of the absorption peak indicates that this new interaction strongly perturbs the excitons and shortens their lifetime **(Fig 7.2b)**. In this scenario, high-density excitons tend to repel each other due to the Pauli exclusion of overlapping electron orbitals, giving rise to positive inter-exciton potential energy. As a

consequence, the energy cost to create an extra exciton increases, leading to a blueshift of the resonance energy.

7.4. Lennard-Jones-like potential as an effective model

The above interpretation has inspired us to quantify the excitonic contributions to the energy shift in the entire density range through a simple phenomenological model with two power laws in analogy to the well-known Lennard-Jones potential between atoms (for which $k = 6$):

$$\Delta E = \varepsilon \left[\left(\frac{r_0}{r_s}\right)^8 - \left(\frac{r_0}{r_s}\right)^k \right] \tag{7.2}$$

Here r_s is the radius of disk occupied by an exciton ($n\pi r_s^2 = 1$), while ε, r_0 and k are the fitting parameters, which can be interpreted in a similar way as in the usual '12-6' power-law potential between atoms. The first term describes the exciton blueshift caused by the short-range Pauli repulsion. We use the r_s^{-8} functional form for better fitting of the Pauli repulsion in this system instead of the usual r_s^{-12} typically chosen in atomic system for convenience due to the relative computing efficiency (r_s^{-12} is the square of r_s^{-6}). The second term models the exciton redshift caused by the long-range van der Waals attraction of excitons behaving as fluctuating dipoles in the presence of plasma in this material. In general, the functional form of this attraction potential can differ from the usual London dispersion force r_s^{-6}, hence we parameterize it as r_s^{-k}. By fitting the ΔE–r_s data through the least squares method with $\varepsilon = 128 \pm 10$ meV, $r_0 = 2.6 \pm 0.1$ nm and $k = 1.4 \pm 0.2$, our simple model matches precisely the density dependence of exciton energy shift **(Fig. 7.5a)**. Note that exciton-exciton annihilation can be present in highly excited monolayer TMDs [129, 130, 133, 134]. The x-axis in **Fig 7.5a** shows the r_s from estimated density that is already corrected after considering the annihilation effect at 2 ps (Section 7.7.2). We note that the exponent k differs (down to one fifth) from the exponent in the Lennard-Jones potential due to the presence of plasma effects in semiconductors, which are not captured by the atomic model. The obtained r_0 = 2.6 nm represents the exciton Bohr radius in monolayer WS_2. This value agrees well with our calculated exciton radius (2.3 nm) [87] and the estimated radius (1–3 nm) in other studies [6, 75, 135].

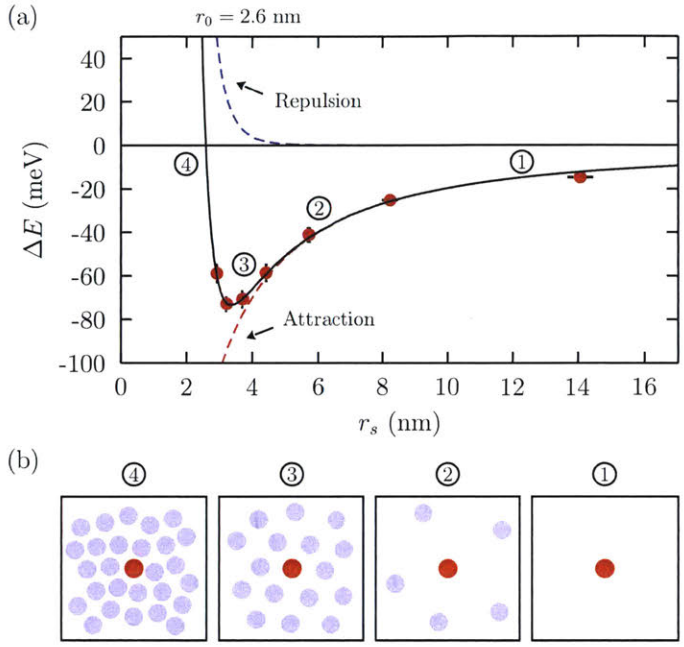

Figure 7.5: (a) Exciton energy shift (ΔE) as a function of average radius (r_s) occupied by an exciton in the exciton gas. The red dots are experimental data from Figure 7.2a. The solid black line is the best fit of our phenomenological model (Eq. 7.2). The dashed lines are the repulsion and attraction components of the inter-exciton potential. $r_0 = 2.6$ nm is the extracted exciton radius. **(b)** Schematic configuration of a probe exciton (red) among the pump-generated excitons (purple) at different interaction regimes (1-4) as denoted in panel (a).

Excitons have been perceived as the solid-state counterpart of atoms, but the analogy is usually drawn only for their similar internal structure and molecular structures. The latter is apparent from the formation of trions [33-35] and biexcitons [26, 37, 43, 89] with binding energies 20-60 meV in monolayer TMDs that are analogous to the hydrogen anion and hydrogen molecules. Here, the good agreement between the modified Lennard-Jones model and our experiments reveals further that they also share similar mutual interaction behavior at long and short distances. This finding is remarkable because high-density excitons are usually unstable against the electron-hole plasma formation and other annihilation processes. These competing processes can easily destroy the exciton resonance features and hinder the observation of inter-exciton repulsion. Monolayer WS_2 is, however, an exceptional material, which hosts tightly-bound excitons with radius approaching the atomic limit. The robustness of these excitons helps maintain their resonance features even at very high density. We can therefore observe an effective

attraction-repulsion crossover of excitonic interactions, a phenomenon that was predicted early [136] but remained unobserved experimentally until now.

Although the observed shift mimics the Lennard-Jones potential, there are three features distinct from atoms that deserve more careful attention. First, in addition to excitons, plasma can be present simultaneously with a relative density governed by the law of mass action. The interparticle separation r_s is derived from their combined densities. Second, plasma contribution to the shift at low density dominates the exciton contribution. The observed $\sim 1/r_s$ dependence, instead of $1/r_s^6$, indicates a negligible contribution from exciton van der Waals attraction. This is not surprising because excitons in monolayer TMDs are tightly bound. Third, a possible formation of biexcitons at short distance is not explicitly captured in this model. This is a similar situation faced by Lennard-Jones potential because it does not explicitly represent chemical bonding between atoms, but it can explain why a cluster of atoms can form at the minimum potential. Although biexciton formation may occur at the minimum potential **(Fig 7.5a)**, the strong plasma screening precludes such occurrence. This is evidenced from the much reduced exciton binding energy at such a high excitation density **(Fig 7.4a)**. This means biexciton binding energy should also be reduced to a value much smaller than the reported values, or completely screened, and thus unlikely to form.

7.5. Chronological signature of interactions in time-resolved spectra

We can further test our model (Eq. 7.2) through its temperature-dependent behavior. Two effects arise when the exciton temperature is high. First, such highly energetic excitons will be in constant motion and dynamically average out their short-range and long-range interactions amongst each other. Secondly, the excitons will have higher probability to reach their internal excited states. These effects will reduce the effective potential energy and increase their Bohr radius. As a consequence, the energy potential well between the excitons will become *shallower* and the inter-exciton distance at the potential minimum will become *wider* (inset of **Fig 7.7a**). In other words, when the

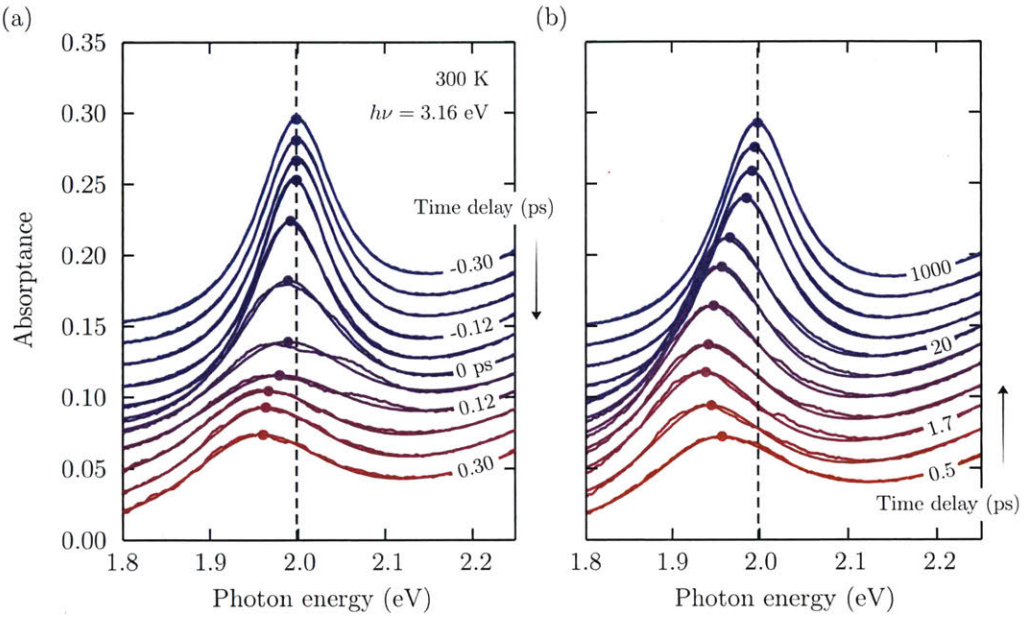

Figure 7.6: (a, b) Exciton absorption peak at increasing time delays from -0.30 to 0.48 ps (a) and from 0.5 to 1000 ps (b), where only the subset of the data is shown for clarity.

excitons cool from very high to low temperature, we predict a significant redshift of their energy. As we discuss below, our model captures the complex cooling dynamics and offers a simple interpretation based on such exciton picture, although rigorous contribution from plasma effects could be included for a more accurate model.

This prediction can be conveniently explored in the cooling dynamics of excitons after pump excitation at high density regime, where exciton-exciton interaction dominates and the exciton picture is particularly appropriate. As we pump monolayer WS_2 using 3.16 eV photons ($h\nu > E_A$), we create free electron-hole pairs that immediately form excitons within the excitation pulse duration [137, 138]. This is due to the strong Coulomb attraction in monolayer WS_2 that leads to a very rapid exciton formation. The large excess energy will bring the excitons to a high temperature ($T_e > 1000$ K). Subsequently, we can follow the time evolution of the exciton resonance as they cool down. **Figures 7.6a-b** show a time series of the exciton absorption spectra up to 1 ns ($F = 11$ uJ/cm^2), from which we extract their peak parameters **(Fig 7.7a-b)**. By examining these parameters, the exciton dynamics can be described roughly in three stages.

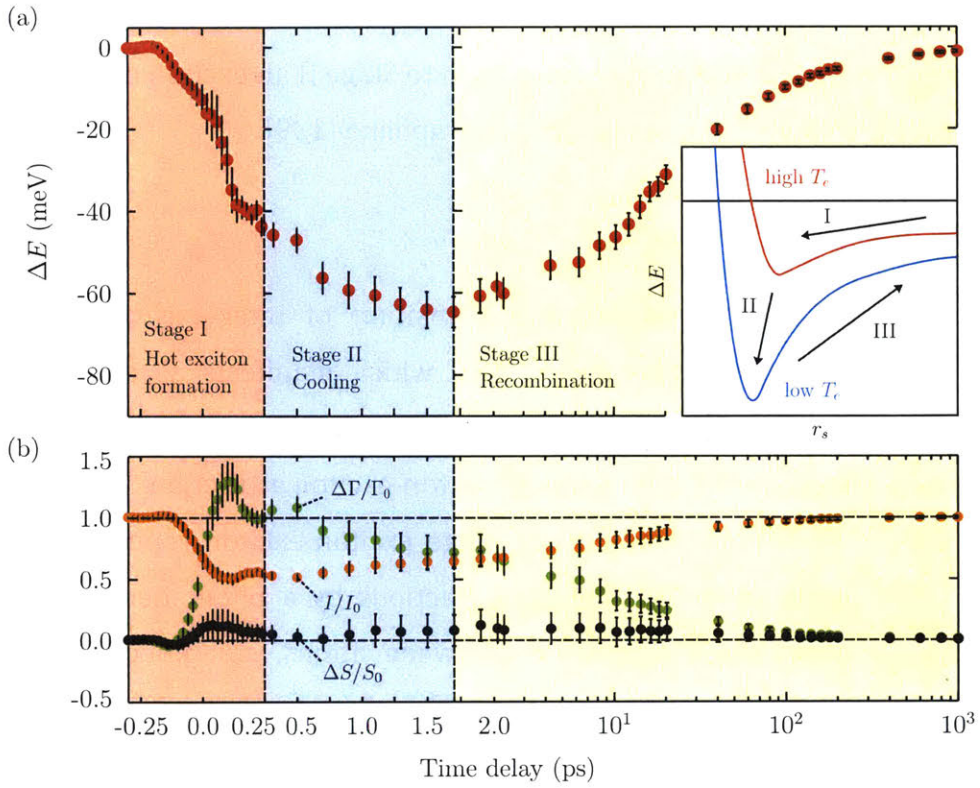

Figure 7.7: (a) Exciton energy shift (ΔE), as well as **(b)** peak height (I/I_0), linewidth broadening ($\Delta\Gamma/\Gamma_0$), and spectral weight change ($\Delta S/S_0$). Inset in (a) shows the stages of relaxation dynamics through the ΔE vs r_s curve at high and low temperatures.

In Stage I (red region), the hot excitons are formed with rapidly decreasing inter-exciton distance, accompanied by a dramatic energy redshift and spectral broadening. In Stage II (blue), the hot excitons cool to the lattice temperature via phonon emission. In Stage III (yellow), the excitons recombine gradually with increasing inter-exciton distance leading to a blueshift. In the framework of our model, such exciton dynamics can be adequately described by the trajectory (I→II→III) between the hot and cold potential energy curves, as illustrated in the inset of **Fig 7.7a**. We exclude possible contribution from lattice cooling in Stage III because the estimated temperature-dependent energy shift is merely ~4 meV (20 K), far too small than the observed shift ~70 meV (Section 7.7.3). It is particularly noteworthy to examine the dynamics in Stage II, where the excitons cool down from $T_e > 1000$ K to ~300 K but the density should remain unchanged. As depicted by arrow II in the inset of **Fig 7.7a**, the exciton energy decreases when the high-temperature potential curve (red) evolves into the low-temperature curve (blue). During this process,

the exciton energy is found to redshift for about 20 meV, accompanied by a decrease of linewidth. With this interpretation, we can assign to Stage II an exciton cooling time of 2 ps, comparable with the cooling time measured in graphene [139].

7.6. Summary

In summary, we have observed a transition of inter-excitonic interaction at increasing exciton density in monolayer WS_2, which manifests as a redshift-blueshift crossover of the exciton resonance energy. At low density, the exciton redshift arises from plasma screening effects and the long-range exciton-exciton attraction. At high density, the exciton blueshift is attributed to the short-range exciton-exciton repulsion. We describe this density dependence of the excitonic interactions by a phenomenological model, in analogy to the Lennard-Jones interaction between atoms, combined with a material-realistic computation of plasma effects. Interpreting the time dependence of energy shifts shortly after the carrier excitation in terms of our model, we extract an exciton cooling time of about 2 ps. Similar results are also observed in monolayer MoS_2, implying that this behavior is ubiquitous in monolayer TMD semiconductors [26]. The close analogy between the excitons and atoms, as shown in our experiment, suggests that the liquid and crystal phases of excitons [140-142] can be realized in 2D materials.

7.7. Supplementary

7.7.1. Microscopic many-body computation

To calculate linear optical properties of monolayer WS_2 on a substrate under the influence of excited carriers, we combine first-principle G_0W_0 calculations with the solution of the semiconductor Bloch equations in screened-exchange-Coulomb-hole (SXCH) approximation for the two highest valence bands and the two lowest conduction bands as described in detail and applied to freestanding monolayer MoS_2 in Ref. [88]. In the following, we describe in detail how the previously used theory has to be augmented to properly take the substrate into account. We assume that the substrate mainly affects the internal Coulomb interaction and neglect its influence on the band structure, as we are only

U		ε		T			
U_2	0.712 eV	ε_2	2.979		d_{z^2}	d_{xy}	$d_{x^2-y^2}$
U_3	0.354 eV	ε_3	2.494	T_1	+0.577	+0.577	+0.577
γ	2.130 Å	a	3.989 Å^{-2}	T_2	+0.816	-0.408	-0.408
δ	0.720 Å^2	b	30.19	T_3	0	-0.707	+0.707
A	2.939 Å^2	c	5.447 Å				
		h	1.564 Å				
		e	4.506				

Table 7.1: Fitting parameters to describe the diagonal bare interaction U, the corresponding eigenbasis T and the diagonal dielectric function ε.

interested in relative shifts of the exciton resonance energy. Therefore, we derive the bare $U_{\alpha\beta}(q)$ and screened $V_{\alpha\beta}(q)$ Coulomb interaction *matrices* in the Wannier-orbital basis (with $\alpha, \beta \in [d_{z^2}, d_{xy}, d_{x^2-y^2}]$) for a freestanding WS_2 slab using the FLEUR and SPEX codes [131, 143]. As discussed in [132], macroscopic screening effects (like those arising from substrates) are described by the *leading* or *macroscopic* eigenvalue of the dielectric matrix. To access this quantity, we transform the full matrices $U_{\alpha\beta}(q)$ and $V_{\alpha\beta}(q)$ to their diagonal representations $U_d(q) = TU(q)T^*$ and $V_d(q) = TV(q)T^*$ using the eigenbasis T of the bare interaction and define the diagonal dielectric function via $\varepsilon_d(q) = U_d(q)/V_d(q)$. Now each diagonal matrix is defined by its three eigenvalues. We fit the leading eigenvalues $U_1(q)$ and $\varepsilon_1(q)$ via

$$U_1(q) = \frac{e^2}{2\varepsilon_0 A} \frac{1}{q(1 + \gamma q + \delta q^2)} \tag{7.3}$$

$$\varepsilon_1(q) = \varepsilon_\infty(q) \frac{1 - \beta_1\beta_2 e^{-2qh}}{1 + (\beta_1 + \beta_2)e^{-qh} + \beta_1\beta_2 e^{-2qh}} \tag{7.4}$$

while all other elements (U_2, U_3, ε_2 and ε_3) are approximated by constant values given in **Table 7.1.**

In Equation (7.3), e is the elementary charge, ε_0 the vacuum permittivity, A the unit cell area per orbital and γ and δ are used to obtain optimal fits to the vacuum extrapolated ab initio data. In Equation (7.3) we introduced the parameters β_i which are given by

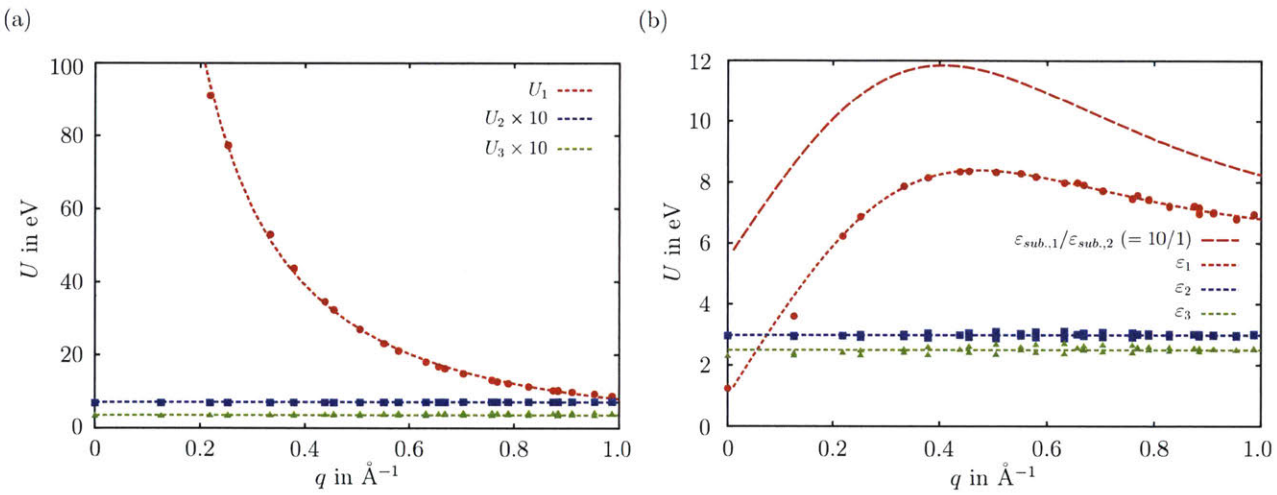

Figure 7.8: (a) Bare Coulomb matrix elements in its eigenbasis. Red dots, blue squares and green triangles correspond to the leading, second and third eigenvalue of $U(q)$ as obtained from ab initio calculations. Dashed lines show the corresponding fits using Equation (7.3) and Table 7.1. **(b)** Eigenvectors of the bare Coulomb matrix (from left to right corresponding to the leading, second and third eigenvalue). The corresponding vector elements of the d_{z^2} (red), d_{xy} (green) and $d_{x^2-y^2}$ (blue) orbitals are shown. Dashed lines indicate constant fits as given in Table 7.1.

$$\beta_i = \frac{\varepsilon_\infty(q) - \varepsilon_{sub.,i}}{\varepsilon_\infty(q) + \varepsilon_{sub.,i}} \tag{7.5}$$

Here, the dielectric constants of the substrate $(i = 1)$ and superstrate $(i = 2)$ are introduced. In order to describe the original ab initio data as close as possible we fit $\varepsilon_\infty(q)$ using

$$\varepsilon_\infty(q) = \frac{a + q^2}{\frac{a \sin qc}{qbc} + q^2} + e \tag{7.6}$$

and set $\varepsilon_{sub.,1} = \varepsilon_{sub.,2} = 1$. As soon as all fitting parameters are obtained (see Table 1) the screening of a dielectric environment can be included by choosing $\varepsilon_{sub.,1}$ or $\varepsilon_{sub.,2}$ correspondingly. In this paper, we use $\varepsilon_{sub.,1} = 10$ ($\varepsilon_{sub.,2} = 1$) which models the screening of the sapphire substrate. In **Figures 7.8 & 7.9**, we present the original ab initio data in combination with the resulting fits in the diagonal basis. In **Figure 7.9**, we additionally show how the dielectric environment modulates the leading eigenvalue of the screening matrix. Using the latter, we can readily derive the fully screened Coulomb interaction $V_d(q) = U_d(q)/\varepsilon_d(q)$ including the screening effects of the dielectric environment. Finally,

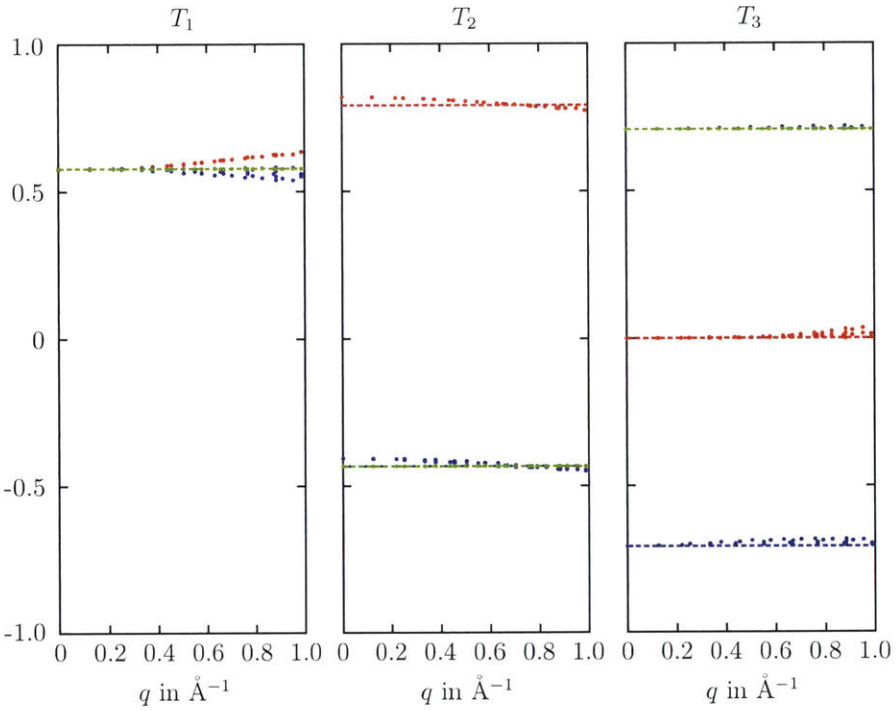

Figure 7.9: Matrix elements of the diagonal dielectric function. Markers indicate ab initio results and dashed lines show the fits using Equation (7.4) and Table 7.1. Next to the freestanding results we plot the leading eigenvalue of the dielectric matrix under the influence of a dielectric substrate with $\varepsilon_{sub,1} = 10$ (long dashes).

we make use of the transformation matrix T to obtain the screened Coulomb interaction matrix in the orbital basis $V(q) = T^* V_d(q) T$.

Besides the analytical description of the screened Coulomb matrix elements we make use of a Wannier-based tight-binding model to describe the electronic band structure (as obtained from G_0W_0 calculations) of the WS_2 slab. To this end, we utilize the same Wannier-orbital basis as described before and derive a minimal three-band model describing the highest valence and two lowest conduction bands using the Wannier90 package [144]. Thereby we solely disentangle our target bands from the rest without performing a maximal localization in order to preserve the original W d-orbital characters. The latter is crucial for the subsequent addition of first and second order Rashba spin-orbit coupling following Ref. [2], which takes into account the large spin-orbit splitting in the conduction and the valence band K valleys. By using this computation approach, we can

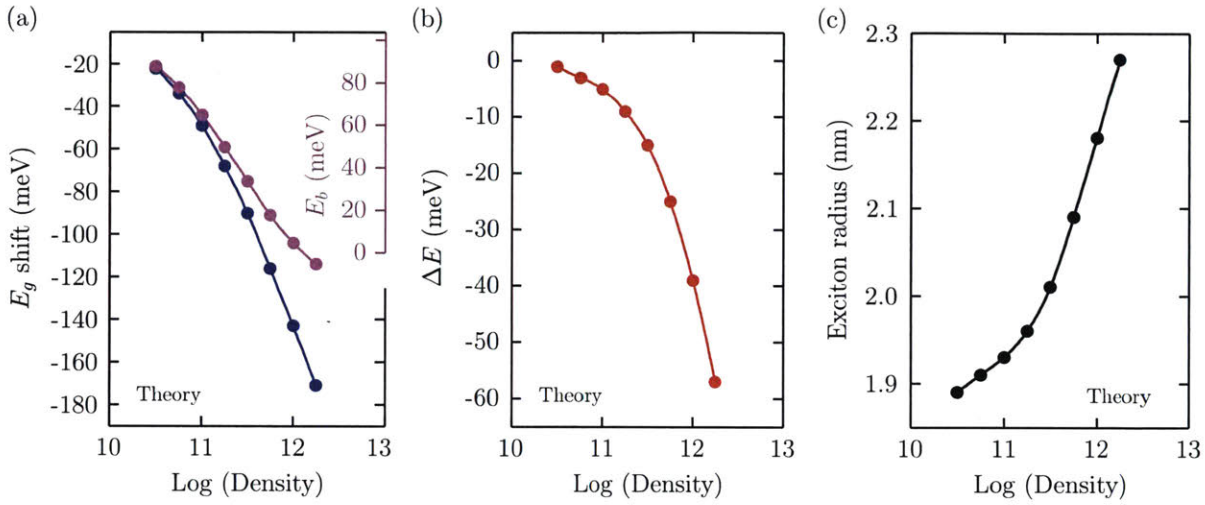

Figure 7.10: Computational results at increasing excitation density on the **(a)** gap narrowing ΔE_g and exciton binding energy E_b, **(b)** exciton shift ΔE, and **(c)** exciton Bohr radius.

obtain the density dependence of gap shift, exciton binding energy, exciton peak shift and Bohr radius along the lines of Ref. [88] **(Fig 7.10)**.

7.7.2. Exciton-exciton annihilation effect

Note that at time delay of 2 ps the actual exciton density will be slightly smaller than the excitation density due to exciton-exciton annihilation [130, 133]. In order to estimate the dissipation rate, we studied the exciton bleaching decay upon photoexcitation with 3.16 eV pump pulse. **Fig 7.11** shows two time-traces of $-\Delta\alpha$ at the A exciton absorption peak with pump fluences of 14.6 μJ/cm^2 and 4.4 μJ/cm^2, where the measured data is shown by the open circles. These pump fluences correspond to excitation densities of $n_0 = 4.3\text{x}10^{12}$ cm^{-2} and $1.3\text{x}10^{12}$ cm^{-2}. Exciton-exciton annihilation can be described by differential equation

$$\frac{dn}{dt} = -kn^2 \tag{7.7}$$

where n is the exciton density at time t, and k is the annihilation rate. This differential equation has a solution

$$n(t) = \frac{n_0}{1 + kn_0 t} \tag{7.8}$$

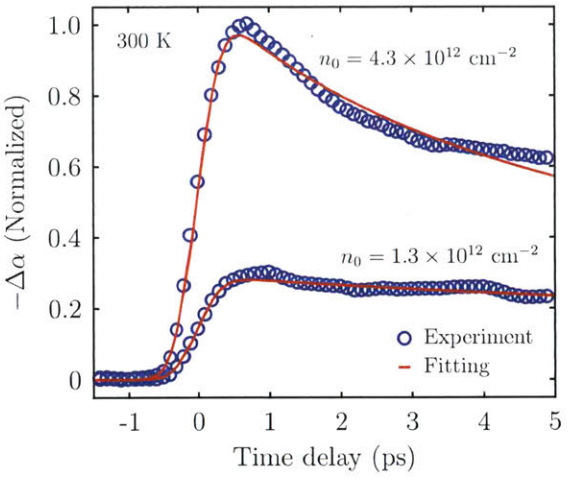

Figure 7.11: Time-traces at different pump fluences to study the exciton annihilation effect on the density. The upper and lower curves correspond to pump fluences of 14.6 μJ/cm² and 4.4 μJ/cm² (open circles are measured data points, red curves are fitting lines). These pump fluences correspond to excitation densities of n_0 = 4.3x10^{12} cm^{-2} and 1.3x10^{12} cm^{-2}.

where n_0 is the initial excitation density. Through global fitting of the two time-traces we obtain an annihilation rate $k = 0.04 \pm 0.01$ cm²/s, where the red curves show the fitting lines. The obtained value is consistent with those reported for CVD-grown monolayer WS_2 of 0.08-0.10 cm²/s [129, 134], at least within an order of magnitude. The uncertainty in the fitting curve at high fluence is a common observation due to the 3.16 eV above-gap excitation and attributed to the fast cooling process [134]. Note that the annihilation rate is dependent on particular substrate used and on the as-grown sample quality. Exfoliated monolayer WS_2 shows greater annihilation rate [133], which is also discussed in Reference [134]. By using the obtained annihilation rate, we renormalize the density on **Fig 7.5a**. At the max fluence we used, the actual density reaches 70% at 2 ps, while at half the max fluence the actual density reaches 83% at 2 ps.

7.7.2 Heat capacity and estimated temperature

In the later parts of our experiments that involve variations in time delays and pump fluence, we used pump photon energy of 3.16 eV which is much higher than the lowest excitation energy (A exciton) of 2.00 eV. This means that, for every e-h pair excited in the pumping process, there will be about 1.16 eV of excess energy after relaxation into the A exciton. In monolayer WS_2, as is also the case for most materials, the relaxation processes are dominated by electron-electron (e-e) and electron-phonon (e-ph)

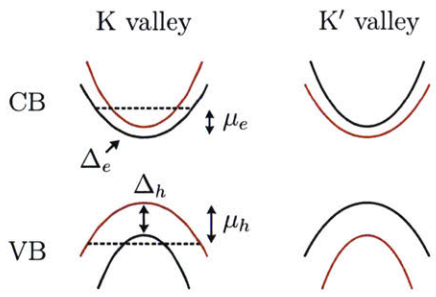

Figure 7.12: Schematic electronic band structure (one-particle picture) of monolayer WS_2 at the K and K' valleys. The CB consists of two electron bands at each valley separated by a spin-splitting gap of $\Delta_e \sim 30$ meV, and the VB consists of two hole bands at each valley separated by a spin-splitting gap of $\Delta_h \sim 400$ meV [4, 5]. The chemical potentials (μ_e and μ_h) of the photoexcited sample are measured from the tip of the relevant bands.

scatterings. Typically, the timescale of e-e thermalization is about 10–100 fs, while the e-ph thermalization is about 1 ps. This means, the excess energy will be first distributed among the electrons to form a hot exciton gas, followed by heat transfer into the lattice. Here, we want to estimate the electronic temperature T_e and the lattice temperature T_l by calculating the corresponding heat capacities. Note that these temperatures will be the upper limits of what we expect from the system because the heat transfer to the substrate is known to be very effective in 2D systems, with a timescale of about 2 ps [139].

The electronic heat capacity C_e (per area) can be expressed as

$$C_e(T) = \int \frac{\partial f(\varepsilon, \mu)}{\partial T} \varepsilon D(\varepsilon) d\varepsilon \tag{7.9}$$

where f is the occupation number of states, μ is the chemical potential, and $D(\varepsilon)$ is the density of states (per area) in the range of energy ε and $\varepsilon + d\varepsilon$. The low-energy excitations in monolayer WS_2 constitute of excitons with various spin combinations in the two valleys **(Fig 7.12)**.

Here, we will consider the contributions of the electrons and holes to the electronic heat capacity separately. In this way, we can account for the spin-valley degeneracy by assuming parabolic energy dispersion for each band as $\varepsilon_n = \hbar^2 k^2 / 2m_n + \Delta_n$, where m_n and Δ_n are the effective mass and the gap of band n (with specific spin-valley index). The density of states can then be expressed as $D(\varepsilon) = \sum_n \theta(\varepsilon - \Delta_n) m_n / 2\pi\hbar^2$, while the

occupation number is $f(\varepsilon,\mu) = [\exp((\varepsilon-\mu)/kT)+1]^{-1}$. The chemical potential, which depends on excitation density n and temperature, has an important role to keep the number of electrons and holes equal ($n_e = n_h = n$). In this quasi-equilibrium condition, where we have intentionally photo-injected the carriers into the system, the chemical potentials μ_e and μ_h are measured from the bottom of the conduction band (CB) and the top of the valence band (VB), respectively, as are also the case for the kinetic energies ε_n. Variations of these chemical potentials with temperature can be followed from the conservation of particle's number density $n = \int f(\varepsilon,\mu)D(\varepsilon)d\varepsilon$. In the case of electrons, this gives

$$n_e/n_T = \ln\left[\left(1+e^{\mu_e/kT}\right)^2\left(1+e^{(\mu_e-\Delta_e)/kT}\right)^2\right] \tag{7.10}$$

and the holes,

$$n_h/n_T = \ln\left[\left(1+e^{\mu_h/kT}\right)^2\left(1+e^{(\mu_h-\Delta_h)/kT}\right)^2\right] \tag{7.11}$$

where $n_T = \langle m_n\rangle kT/2\pi\hbar^2$ is called the thermal quantum density. Hence, for a given excitation density, we can compute the chemical potentials as a function of temperature. Finally, by using the above equation, we can calculate the electronic heat capacity as a function of temperature **(Fig 7.13a)**. The actual electronic heat capacity is expected to be larger than this because of the higher-lying bands which we have ignored in the present calculations.

As shown in **Fig 7.13a**, C_e increases rapidly at low temperatures and saturates at higher temperatures. Note that heat capacity is proportional to the number of electrons that can store the thermal energy. At low temperatures (quantum regime), only the electrons around the Fermi level can contribute to C_e. At higher temperatures (classical regime), electrons are more sparsely distributed across different energies, hence more electrons can contribute to C_e until it reaches a saturation value where all of the electrons are involved. The transition between quantum and classical regimes should happen at temperature reaching the electron-hole chemical potential, $k_bT \sim \mu_{e,h}$. This is also consistent with the fact that in classical regime C_e is proportional to the excitation density n.

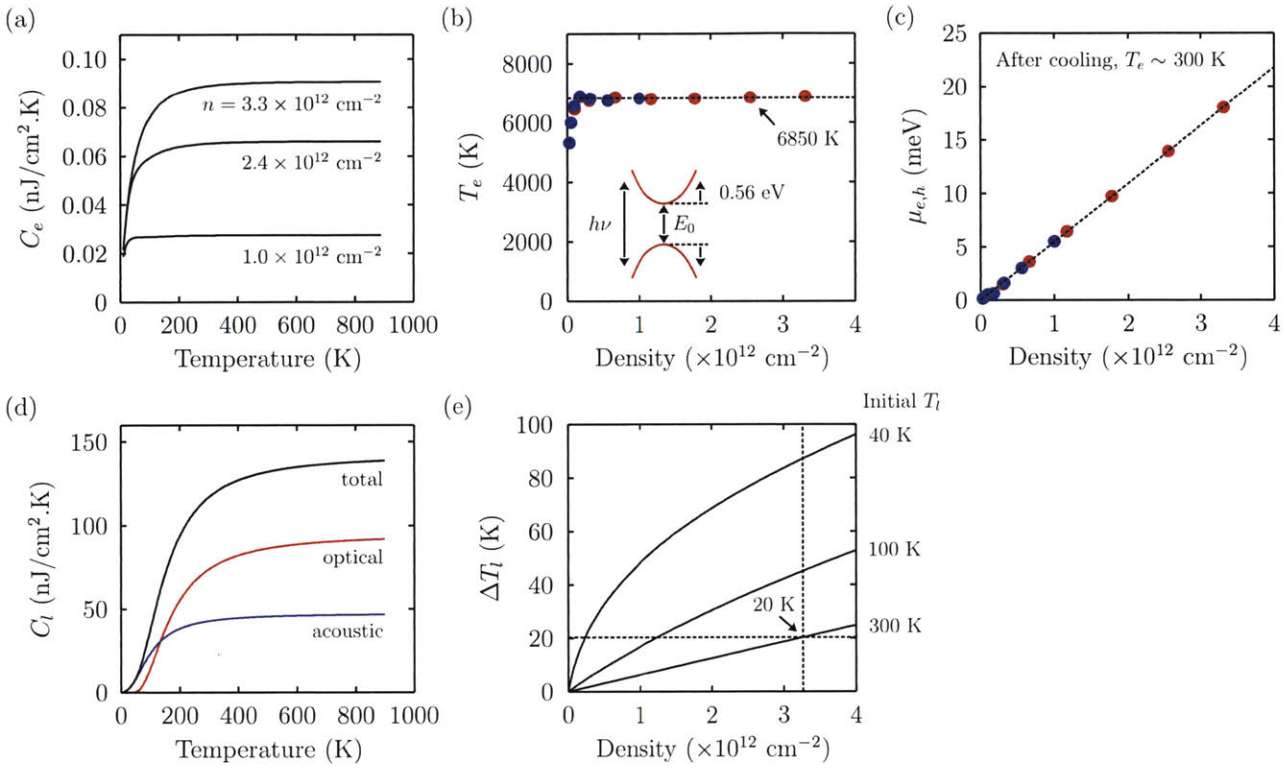

Figure 7.13: Estimating the electronic and lattice temperatures after photoexcitation by calculating the heat capacities and the absorbed excess energy. **(a)** Electronic heat capacity $C_e(T)$ of monolayer WS_2 by considering the lowest e-h excitations at K,K' valleys. **(b)** T_e vs n. **(c)** $\mu_{e,h}$ vs n. **(d)** Lattice heat capacity $C_l(T)$ by considering three acoustic and six optical phonon modes. **(e)** ΔT_l vs n. Here, the electrons and lattice are treated separately.

We can now estimate the rise of temperature upon photoexcitation in monolayer WS_2 by using

$$\Delta Q = n\Delta E = \int C(T)dT \tag{7.12}$$

where ΔQ is the absorbed energy density, n is the photoexcited pair density and ΔE is the excess energy per pair (1.13 eV). Note that in monolayer WS_2, the usual (singlet) A exciton is slightly higher by $\Delta_e = 30$ meV as compared to the (triplet) A exciton. In the first few hundreds of femtoseconds after photoexcitation, most of the excess energy is redistributed among the electrons. By using the obtained $C_e(T)$ and ΔQ, we can calculate T_e for a given excitation density as shown in **Fig 7.13b**. The results show that, except at very low densities, the electronic system reaches a constant $T_e = 6850$ K at all densities. In fact, this

result can be understood if we assume that every photoexcited charge carrier (electron or hole) carries an excess photon energy of $(h\nu - E_0)/2 = 0.56$ eV, which will be stored as their thermal energy $k_b T_e$. This will amount to $T_e \sim 6500$ K regardless of the density, and this is consistent with the above results. So, if we were to use higher photon energy, T_e would increase correspondingly. Therefore, in ideal condition, the electronic system at short timescale should correspond to the same temperature of 6850 K at all fluences. However, in reality the transient electronic temperature is usually much smaller (typically $T_e > 1000$ K) due to rapid thermalization with phonons that we discuss below.

In short timescale, the thermal energy will be distributed to the lattice (~1 ps) or substrate (~10-1000 ps), and T_e will decrease back to 300 K. In this situation, we can estimate the chemical potential $\mu_{e,h}$ of the charge carriers for a given excitation density. **Figure 7.13c** shows that $\mu_{e,h}$ increases linearly with density, and the chemical potentials are the same for electrons and holes because they have similar effective mass in monolayer WS_2 ($m_e = m_h = 0.44\, m_0$, [145]). Such a linear increase in $\mu(n)$ is quite expected due to the constant density of states $D(\varepsilon)$ in an ideal 2D system. Note that, at the excitation density that we used in the experiment, $\mu_{e,h}$ is still lower than the spin-splitting of the two bands ($\Delta_e = 30$ meV, $\Delta_h = 400$ meV). So, for much higher excitation densities, we would expect the $\mu_{e,h}$ vs n slope to be lowered into half as it approaches $\mu_{e,h} \sim 30$ meV.

For the lattice heat capacity C_l, we calculated separately the contribution from the acoustic and optical phonon modes. Monolayer WS_2 has three atoms in the unit cell, with three acoustic and six optical modes. By taking the average optical phonon energy as $\hbar\omega_0 = 45$ meV [146], we can estimate its contribution to C_l per unit cell as

$$C_{op}(T) = \frac{\partial}{\partial T}\left(\frac{6\hbar\omega_0}{e^{\hbar\omega_0/kT} - 1}\right) \tag{7.13}$$

For the acoustic phonon contributions (per unit cell), we can use the 2D Debye model which gives

$$C_{ac}(T) = 6k_b\left(\frac{T}{\Theta}\right)^2 \int_0^{x_D} \frac{x^3 e^x}{(e^x - 1)^2} \tag{7.14}$$

where the Debye temperature is defined as $\Theta = (\hbar v/k_b)\sqrt{4\pi/A_{cell}}$ and the Debye cutoff is $x_D(T) = \Theta/T$. We calculated the Debye temperature ($\Theta = 460$ K) by using an average sound velocity v of about 5×10^3 m/s [146], and an area per unit cell A_{cell} of 8.46×10^{-16} cm^2 with a lattice constant of $a = 3.13$ Å [146]. Finally, the total lattice heat capacity can be calculated, which is shown in **Fig 7.13d**.

Figure 7.13d shows that $C_l(T)$ increases rapidly at low temperatures and saturates to its Dulong-Petit value at higher temperatures. Note that C_l is about 1000 times larger than C_e, and this means for a given n the temperature increase ΔT_l would be much smaller than ΔT_e. **Figure 7.13e** shows ΔT_l as a function of n for different initial lattice temperatures T_l. Since in our time-dependent experiment we used $n = 3.3\times10^{12}$ cm^{-2} at $T_l = 300$ K **(Fig 7.7)**, ΔT_l increases by only about 20 K. Unlike the electronic system where the excess photon energy is redistributed evenly to the charge carriers that results in a constant $C_e(n)$, the lattice will absorb the total excess energy from all of the charge carriers. Hence, C_l increases with n.

Now, if we allow a strong e-ph coupling to direct the absorbed energy into the lattice, we can merely use the total lattice heat capacity to estimate the temperature of the system. This is because $C_l \gg C_e$. As we can see from **Fig 7.13b&e**, with excitation density of 3.3×10^{12} cm^{-2} **(Fig 7.7)**, the electronic temperature could reach $T_e > 1000$ K for a short while until it cools down to share a common temperature with the lattice to about 320 K. In fact, we must also consider the heat transfer to the thick substrate, which effectively plays a role as the thermal reservoir at 300 K. As a result, the actual temperatures should be much lower than what we have estimated in this analysis, similar to what have been observed in suspended vs supported graphene [139].

Chapter 8

XUV based Time-resolved ARPES

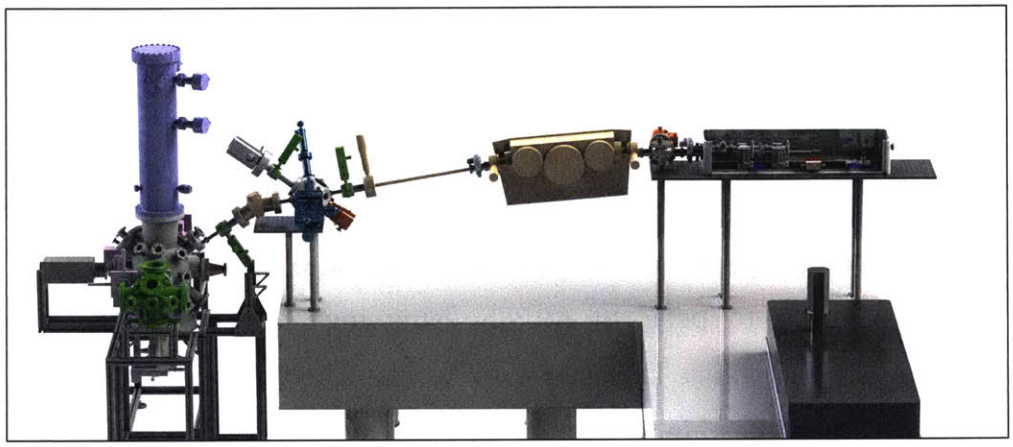

Contents

8.1. Building a high-resolution XUV light source for TR-ARPES

8.1.1. Overview

Angle resolved photoemission spectroscopy (ARPES) has the unique ability to resolve the electronic band structure of materials in momentum space. In this technique, photons of energy higher than the work function are used to eject electrons. By measuring the energy and momentum of these photo-ejected electrons, one can obtain the energy-momentum dispersion relation inside the material. ARPES has made a tremendous impact in condensed matter physics by helping to understand the physics of materials including topological insulators, strongly correlated materials, and two-dimensional materials such as graphene and TMDs.

Traditionally, these experiments are performed at synchrotrons, which can provide tunable high-energy photons. With the advent of femtosecond lasers, it has recently become possible to perform ARPES using high harmonics of lasers. Initially, fourth harmonic of Ti:sapphire lasers at 6 eV were used as the light source. Using lasers as the light source provides higher energy and momentum resolutions yielding in much sharper spectra compared with the synchrotron ARPES. Our laboratory at MIT has pioneered the use of time-of-flight based energy analyzers in laser ARPES experiments [147], which provide 3D dispersion (energy and two components of momentum) as opposed to 2D dispersion that can be obtained at synchrotrons without needing to rotate the sample [148, 149]. Laser ARPES has also made it possible to add time resolution to these experiments by using pump-probe method to record a femtosecond movie of electronic band structure after photo-excitation by another laser pulse [150]. With these advantages, time-resolved laser based ARPES has the potential to make another huge impact in condensed matter physics.

Although this technique has great potential, it also has several challenges that need to be resolved. Initial laser based ARPES experiments were limited to 6 eV. This seriously restricts the range of accessible momentum values in k-space

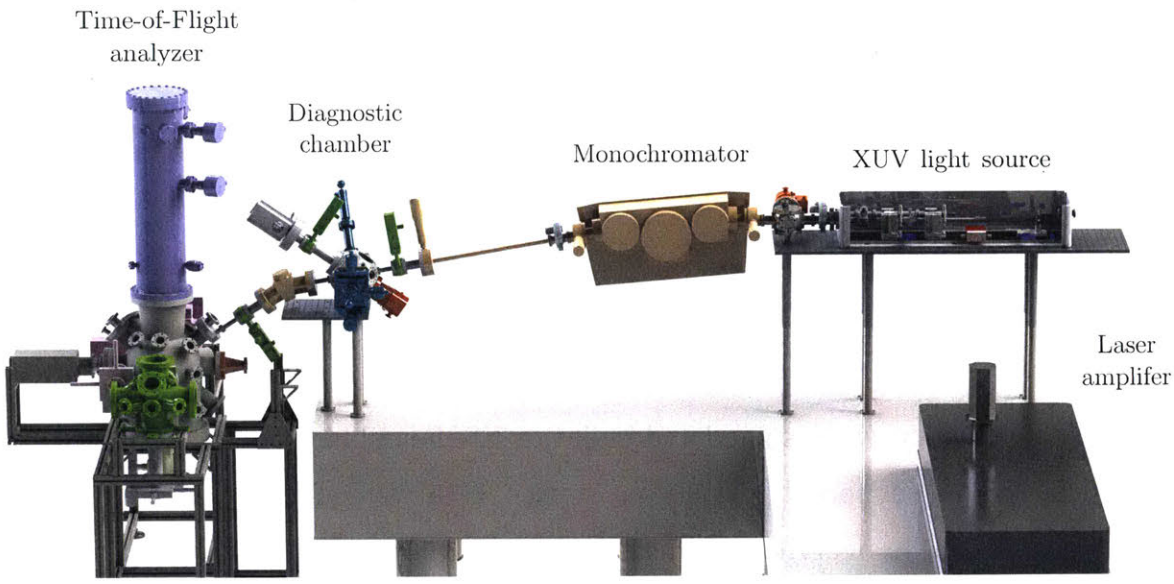

Figure 8.1: Overview of the XUV beamline for ARPES setup.

$$\hbar k_{\parallel} = \sqrt{2m(h\nu - \phi)}\sin\theta \tag{8.1}$$

where $k_{\parallel}$ is the in-plane momentum of the electron, m is the free electron's mass, $h\nu$ is the photon energy, ϕ is the work function, and θ is the propagation angle from normal. For a number of problems, dynamics of interest are near the edge of the Brillouin zone (BZ) inaccessible to this method. The cross section for scattering is also very low at these energies for several material systems. Furthermore, in order to obtain the dispersion in the direction normal to the sample surface, one needs to vary the energy of the light source. For these reasons, there has been a great need in the ARPES community for high harmonic generation based light sources that can reach to high energies (up to 500 eV).

In order to overcome this limitation, we developed a new technique that integrates the Time-of-Flight (ToF) electron analyzer with a new light source from high harmonic generation (HHG). This HHG light source is capable to generate high-energy photons in the extreme UV (XUV) regime with short pulsewidth, which is combined with the high-repetition rate ToF electron analyzer. XUV based TR-ARPES should enable bandstructure mapping in the entire range of the Brillouin zone and provides insight into the entire non-equilibrium dynamics of electrons and their interactions in solids.

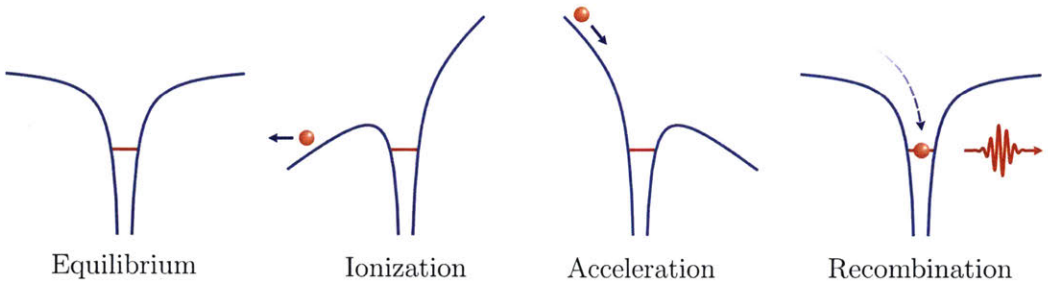

Figure 8.2: Three-step model of high harmonic generation.

In our laboratory, we designed and built the XUV beamline for our ARPES setup in a series of three major sections: 1) XUV light source, 2) XUV monochromator, and 3) XUV diagnostic chamber. The overview of this setup is shown in **Fig 8.1**. Each section plays a crucial role, which we will discuss in more details in later sections, and briefly described as follows. In the XUV light source section, the output from a fundamental laser amplifier is used to drive a HHG process inside a hollow fiber filled with krypton gas. The XUV monochromator is used to pick one harmonic and narrow down the energy resolution of the HHG beam, while preserving a good time resolution. The XUV diagnostic chamber is used to characterize the HHG beam properties such as the photon energy, intensity and spot size. Our setup can produce 30 eV XUV photons at 36 meV energy resolution, which is a very high energy resolution for XUV based TR-ARPES.

8.1.2. XUV light source

High harmonic generation is (HHG) is a nonlinear technique for producing coherent light pulses at frequencies many harmonics higher than the fundamental frequency. Typically, intense laser pulses at near infrared (NIR) are targeted on noble gases producing laser pulses at extreme ultraviolet (XUV) between 10-100 eV [151, 152]. The physics of HHG process can be explained semi-classically using a three-step model [153], followed by a full quantum mechanical description [154, 155]. **Figure 8.2** illustrates the electron potential energy around an ion. In equilibrium, the Coulomb potential ensures that the electron is trapped around the ion. On the first step upon laser pulse incidence, the electron tunnel ionizes from the parent ion due to Coulomb potential tilting by the strong electric field from the laser. Here, the electron can be assumed to be completely ionized in vacuum

with zero initial velocity. On the second step, the electron is subsequently accelerated away by the laser pulse electric field during the first half cycle of the optical field. During the second half cycle, the electron is accelerated toward the parent ion where it accumulates a large kinetic energy. On the third step, the electron recombines with the parent ion and returns to its ground state while emitting the accumulated energy into radiation at high photon energy. This HHG description is also known as the recollisional model of HHG. The emitted photon energy is given by

$$\hbar\omega = I_p + E_k \tag{8.2}$$

where I_p is the ionization potential and E_k is the accumulated kinetic energy. Since the tunnel ionization process can occur at any phase ϕ of the optical field, the accumulated kinetic energy prior to recombination therefore depends on this phase, $E_k(\phi)$. The phase for maximum kinetic energy is calculated to be 18°, giving a kinetic energy of $3.17\times U_p$ with a ponderomotive energy of $U_p = e^2E^2/4m_e\omega^2$. This leads to a maximum photon energy that can be obtained through HHG process that is also called the cut-off energy, $\hbar\omega_{cut-off} = I_p + 3.17U_p$. This cut-off energy has been used as the important experimental signature to search for accurate theoretical description of the HHG process. From this we can make better predictions to achieve efficient HHG output at a particular photon energy regime.

The noble gas that we use to produce XUV photons can also reabsorb the produced photons. Thus, we cannot simply use a bulky gas container and shoot an intense laser beam towards it because it would not be effective. In order to minimize this reabsorption process, the gas must be confined in a small region of space where it only interacts with the incident laser beam during the generation process and not further downstream the XUV beamline. There are two methods commonly implemented to introduce the gas in HHG experiments: 1) gas jet and 2) hollow fiber **(Fig 8.3a-c)**. In the first method, the beam is focused onto a gas jet directed perpendicular to the beam propagation. In the second method, the beam is tightly focused into a hollow fiber and it propagates by total internal reflection inside the hollow fiber. The gas is injected through a separate opening in the middle of the fiber and let out through the two opposite ends. These two methods

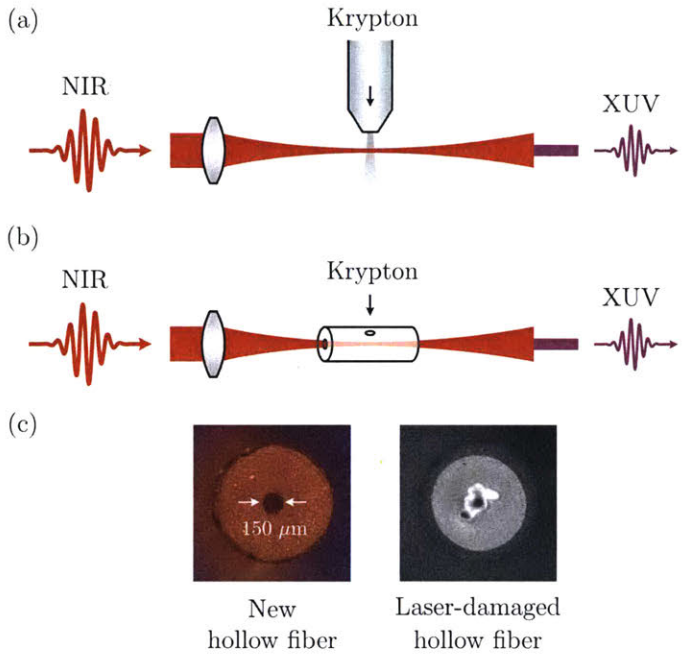

Figure 8.3: Experiment layout for HHG process using **(a)** gas jet and **(b)** hollow fiber. **(c)** Cross-sections of the new and laser-damaged hollow fibers seen under microscope.

contribute differently to the phase matching condition between the fundamental and harmonic frequencies

$$\Delta k = k_{neutral} + k_{plasma} + k_{geometric} \tag{8.3}$$

where the three terms are contributions from the dispersion in neutral gas ($k > 0$), the ionized gas or electrons ($k < 0$), and the free space ($k > 0$) or fiber-guided beam propagation ($k < 0$), respectively. The phase matching condition is achieved by tuning the gas pressure and the laser intensity. Additional discussion on this can be found in the dissertation by T. Rohwer [156].

In our laboratory, we use the hollow fiber method where the gas is injected by a gas flow controller from MKS Instruments [157]. The overview of this HHG setup is shown in **Fig 8.4**. This instrument is available commercially as XUUS from KM Labs. We use krypton or xenon gas owing to its higher HHG conversion efficiency at low-order harmonics as compared to its cheaper alternative, the Ar gas [158, 159]. Balcou et. al. have shown that higher conversion efficiency for low-order harmonics process can be achieved by using heavier noble gas like Xe [158]. This is in connection with its higher polarizability as

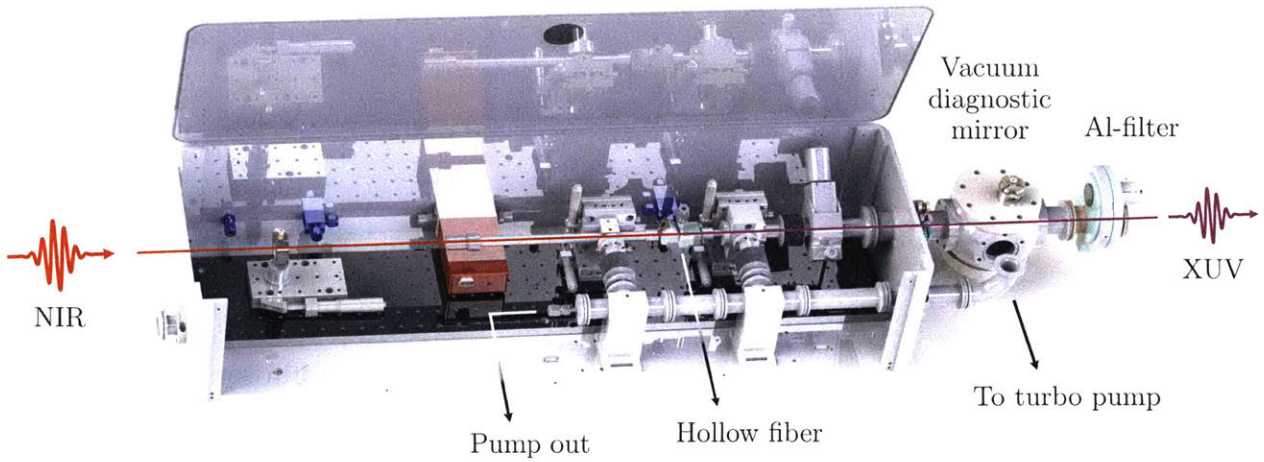

Figure 8.4: Overview of the XUV light source in our setup (XUUS from KM Labs). Only the main components are shown here. Solidworks drawing courtesy of Xiaoshi Zhang and Wilhelm Estrada, KM Labs.

compared to the other noble gases. Furthermore, a combination of lower ionization energy and higher incident photon energy can in principle increase the conversion efficiency for low-order harmonics even further [158, 160]. The HHG process is driven by a Ti:sapphire laser amplifier (Wyvern 500, KM Labs) with photon energy 1.59 eV (780 nm), pulse duration 50 fs, and typical pulse energy >250 mJ at 30 kHz repetition rate. The generated XUV light contains a number of different harmonics that propagates as one beam.

8.1.3. XUV monochromator

The energy resolution for an ARPES measurement is determined largely by the photon energy linewidth, apart from other significant factors such as the sample quality, energy analyzer setting, and geometric alignment. For this reason, we must first pick a particular harmonic from the generated XUV beam. Each harmonic produced by 50 fs laser pulse at 780 nm in a hollow fiber can have a typical linewidth in the order of 100 meV, which is still too large to see any clear feature from the bandstructure. Hence, it is crucial to narrow down the linewidth further; and we do this by using an XUV monochromator.

We take special efforts in designing the XUV monochromator because it plays an especially significant role in the overall performance of time-resolved ARPES in our laboratory to achieve 1) a high fluence throughput, 2) narrow energy linewidth, and 3)

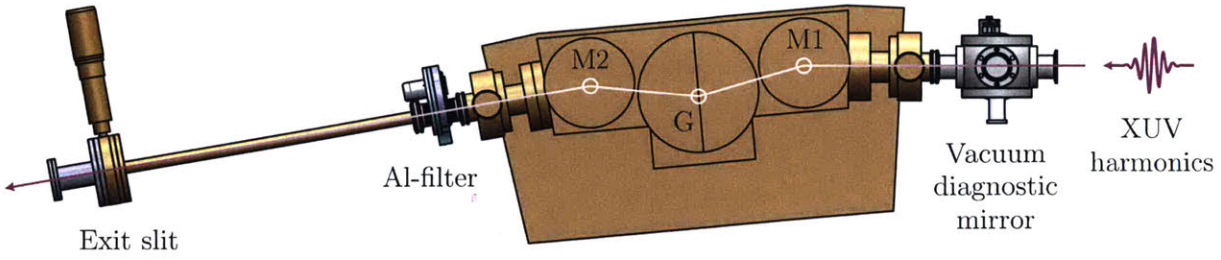

Figure 8.5: Overview of XUV monochromator in our setup.

short pulsewidth. The first parameter must ensure sufficiently high photon fluence at the sample for fast data acquisition, typically 10^9 photons/sec or higher. The last two parameters have their minimum values determined by the uncertainty relation, for a transform limited pulse. In practice, this is expressed by the time-bandwidth product: $\Delta\tau\,\Delta\nu = 0.441$ for a gaussian pulse, where $\Delta\tau$ is the pulsewidth (sec) and $\Delta\nu$ the frequency (Hz). By converting the units, we can obtain a more relevant expression for TR-ARPES

$$\Delta\tau(fs)\,\Delta E(eV) = 1.823 \tag{8.4}$$

where now the pulsewidth is in femtosecond unit while the energy linewidth is in electron-volt unit. For example, our fundamental laser has a pulse width of 50 fs that must be supported by a minimum energy bandwidth of 36 meV. The above three parameters – fluence, energy linewidth, and pulsewidth – serve as the guiding lines for designing the XUV monochromator.

Note that there is a drastic pressure difference between the XUV light source at 10-100 Torr (noble gas) and the ARPES measurement chamber at 10^{-11} Torr. All of the optical components of this XUV beamline are housed in vacuum chamber, including the XUV monochromator. In order to maintain the ultra high vacuum condition at the ARPES chamber, we installed two 100 nm thick aluminum filters (from Lebow Company) that suppress a major flow of the noble gas, as well as three turbo pumps in consecutive stages of differential pumping – one right after the XUUS light source, one at the XUV monochromator, and one at the (next) XUV diagnostic chamber.

The overview of our XUV monochromator is shown in **Fig 8.5**, which is manufactured by McPherson. The main chamber of the monochromator comprises two

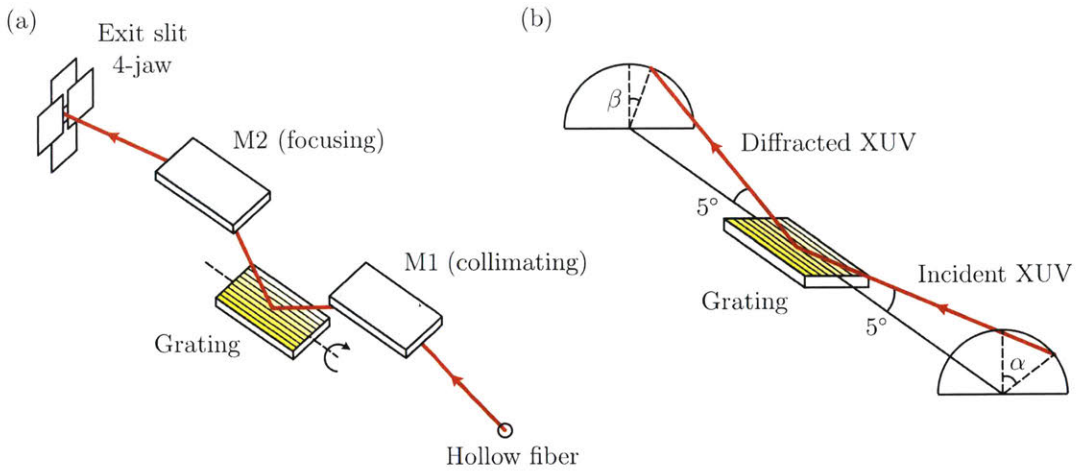

Figure 8.6: (a) Optical layout inside our XUV monochromator. **(b)** Light diffraction by an off-plane mounted grating that forms cones with half angle 5°.

toroidal mirrors (M1, M2) and a stack of three gratings (G1, G2, G3), all optics are gold-coated and mounted at 5° grazing angle configuration. We implemented the X-ray Czerny-Turner (XCT) design that has a symmetric optical layout with respect to the grating. There are two arms – one between the light source and M1, the other one between the exit slit and M2 – each has a nominal focal length of 800 mm. M1 and M2 are reversed identical whose toroidal surfaces are curved such that the XUV light gets collimated toward the grating. To operate the monochromator at three different photon energies and resolutions, we selected three gratings with different blaze angle and groove density. The three gratings are mounted in parallel on a sliding track for an easy switch inside the vacuum. In this experiment, the grating is mounted such that the groove lines are parallel to the plane of incidence. This is called an off-plane mounted (OPM) grating configuration, and the resulting conical spectral dispersion forms an arc perpendicular to the plane of incidence **(Fig 8.6a-b)**. This is different from the conventional in-plane grating, because the OPM provides a better intensity throughput at grazing incidence. The active grating is mounted on a motorized stage where the rotation axis coincides with the surface of the grating oriented along the plane of incidence. The energy linewidth of the outgoing beam can be suppressed further by narrowing the exit slit horizontally.

The reflectivity of XUV light is very sensitive to the incidence angle, photon energy and polarization, which can be theoretically estimated through calculations using the

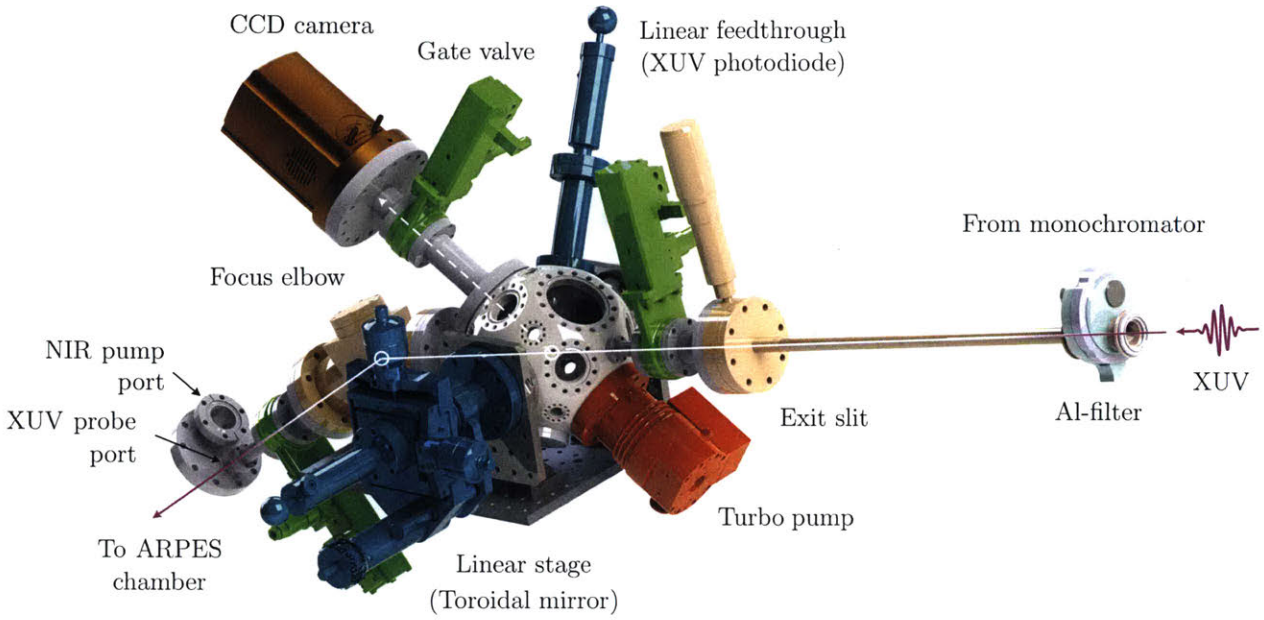

Figure 8.7: Overview of the XUV diagnostic chamber in our setup.

Fresnel equations [161, 162]. Here, the incidence angle is measured relative to the surface and not to the surface normal. For example, at 45° incidence angle, 30 eV photon energy and photon polarization parallel to the surface, the estimated reflectivity of a gold-coated mirror is 22%; meanwhile, at 5° grazing incidence angle, the reflectivity is 85%. We decided to set the XUV monochromator at 5° grazing incidence angle and 800 mm focal length for detailed reasons that eventually determines the fluence throughput, energy resolution and time resolution.

8.1.4. XUV diagnostic chamber

The XUV diagnostic chamber hosts a CCD camera and an XUV photodiode, which we use to measure the XUV photon energy, fluence, and spot size, and to monitor the HHG efficiency while optimizing the HHG fiber alignment **(Fig 8.7)**. The main chamber is purchased from Kimball Physics. A toroidal mirror can be inserted in and out of the beam path using a manual linear stage that is attached to the main chamber. When the toroidal mirror is inserted at the center of the chamber, the XUV beam gets reflected and focused into the CCD camera. The camera consists of a back illuminated CCD with pixel size 13.5 μm

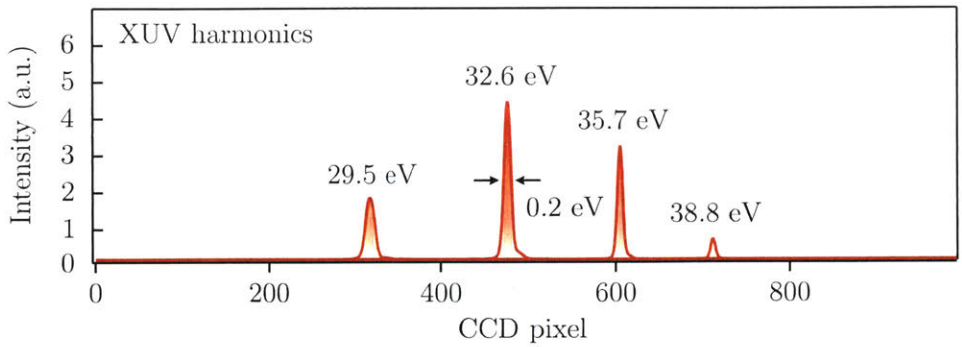

Figure 8.8: XUV harmonics as imaged from CCD camera in the diagnostic chamber.

(Newton SO DO940P-BN from ANDOR). The XUV light that is spectrally dispersed by the grating can be imaged at this camera when the exit slit is fully open, displaying a series of XUV harmonics **(Fig 8.8)**. This figure shows the XUV harmonics at 29.5 eV (19th), 32.6 eV (21st), 35.7 eV (23rd) and 38.8 eV (25th), driven by fundamental laser pulses tuned at 800 nm using krypton gas at the hollow fiber. When the toroidal mirror is removed from the beam path, we can insert an XUV photodiode to measure the fluence. The photodiode is wired to a UHV electrical feedthrough and connected to a lock-in amplifier. The XUV light will be absorbed at the photodiode and create electron-hole pairs that will register into an electric current from which we can determine the photon flux. For instance, the conversion efficiency of the photodiode is 0.26 A/W at photon energy of 30 eV. Hence, a measured current of 5 nA corresponds to 4×10^9 photons/sec. Note that the pressure at this chamber is always below 5×10^{-9} Torr (the pressure gauge lower limit) during operation mode.

During ARPES measurements, the movable toroidal mirror and the XUV photodiode are parked away from the beam path so that the XUV light can pass through the chamber and enter the last section – the focus elbow. A toroidal mirror is mounted at this focus elbow so that the diverging XUV light from the exit slit is refocused into the sample symmetrically. The toroidal mirror is curves for a 1-to-1 imaging ratio between the exit slit and the sample position. The resulting spot size at the sample is therefore adjustable by the exit slit down to 100 μm.

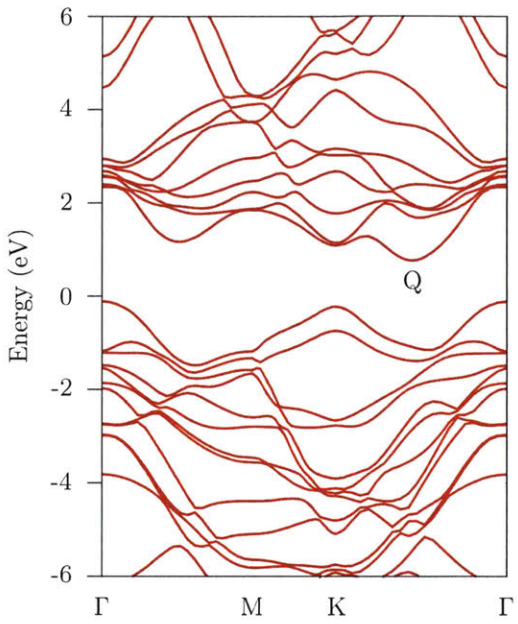

Figure 8.9: Calculated electronic bandstructure of bulk WSe_2. Figure is obtained from Reference [3].

8.2. Measuring TMDs using 30 eV XUV TR-ARPES

Our HHG setup is optimized to produce XUV photons at 30 eV (19th harmonic) with flux 4×10^9 photons/sec per harmonic. Here, we used fundamental laser pulses with pulse duration of 50 fs, power 10 W at 30 kHz to drive the HHG process. During ARPES measurements, we further narrow the exit slit in order to achieve a better energy resolution of 36 meV. We used this system to measure the electronic bandstructure of various TMDs including semiconductors WSe_2 & WS2, and semimetal WTe_2. In this section, we display the measured bandstructures to show the great capability of this XUV based ARPES.

8.2.1. WSe_2 semiconductors

The bandstructure of bulk WSe_2 is calculated in Reference [3] and shown in **Fig 8.9**. In general, it has a similar structure to that of monolayer WSe_2 except that the conduction band minimum has shifted from K point halfway toward the Γ point, resulting in an indirect gap semiconductor. In **Figure 8.10**, we map the Brillouin zone of WSe_2 at slightly below the valence band maximum using 30 eV laser ARPES at 30 K. In this measurement, we tilt the

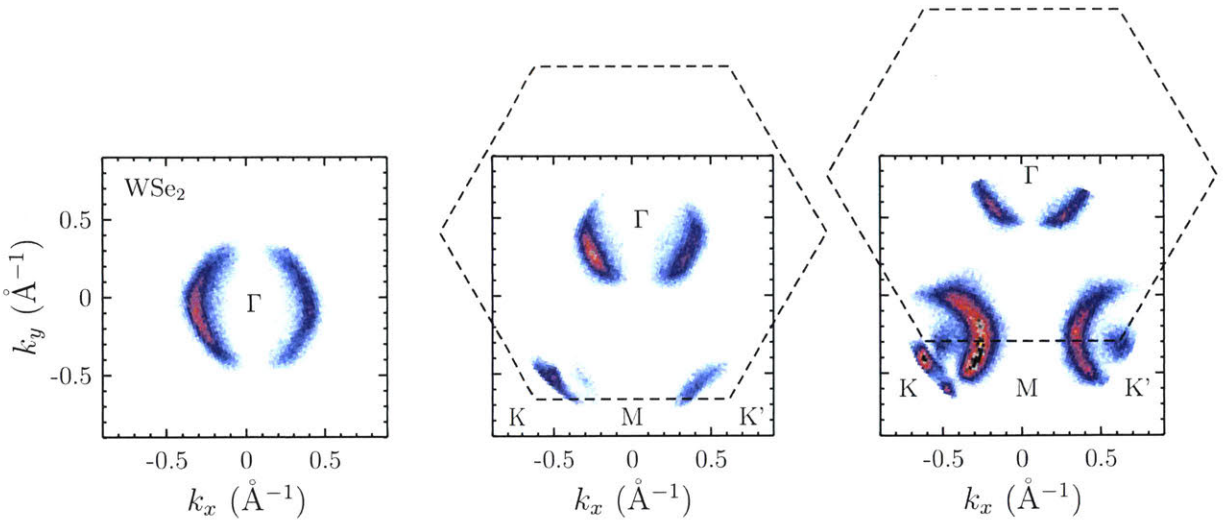

Figure 8.10: ARPES measurement of bulk WSe_2, constant energy surface at slightly below the valence band top. Subsequent panels from left to right are obtained by tilting the sample to reach the K and K' valleys in the Brillouin zone. The right panel shows the A and B valence bands at the K and K' valleys. Photoemission is performed using 30 eV XUV at sample's temperature of 30 K.

sample until around 45° in order to map the K and K' valleys. The 30 eV photon that we use to photoemit the electrons enables us to reach the K and K' points in the Brillouin zone, which cannot be achieved using 6 eV laser ARPES. It also allows us to probe into deeper binding energies.

Time-of-Flight detection allows us to obtain 3D dispersion (E, k_x, k_y) without continuously tilting the sample. **Figure 8.11a-b** shows the energy dispersion along the (a) K-M-K' line in the Brillouin zone and the (b) linecut perpendicular to it (raw data). We can identify the two valence bands that are split by 540 meV due to the strong spin-orbit coupling in this material. Unlike in monolayer WSe_2, each of these valence bands corresponds to the up-spin and down-spin states altogether, originating from every two adjacent layers of WSe_2. This is allowed by the non-centrosymmetric crystalline structure in bulk WSe_2 unlike in monolayer WSe_2. Furthermore, the high energy-resolution of our setup enables a clear observation of band repulsion fine structures at binding energy $E_b = 3$ eV.

Photoexcitation can promote electrons from the valence bands to occupy the higher lying conduction bands using pump pulse of 1.59 eV, which is larger than both direct

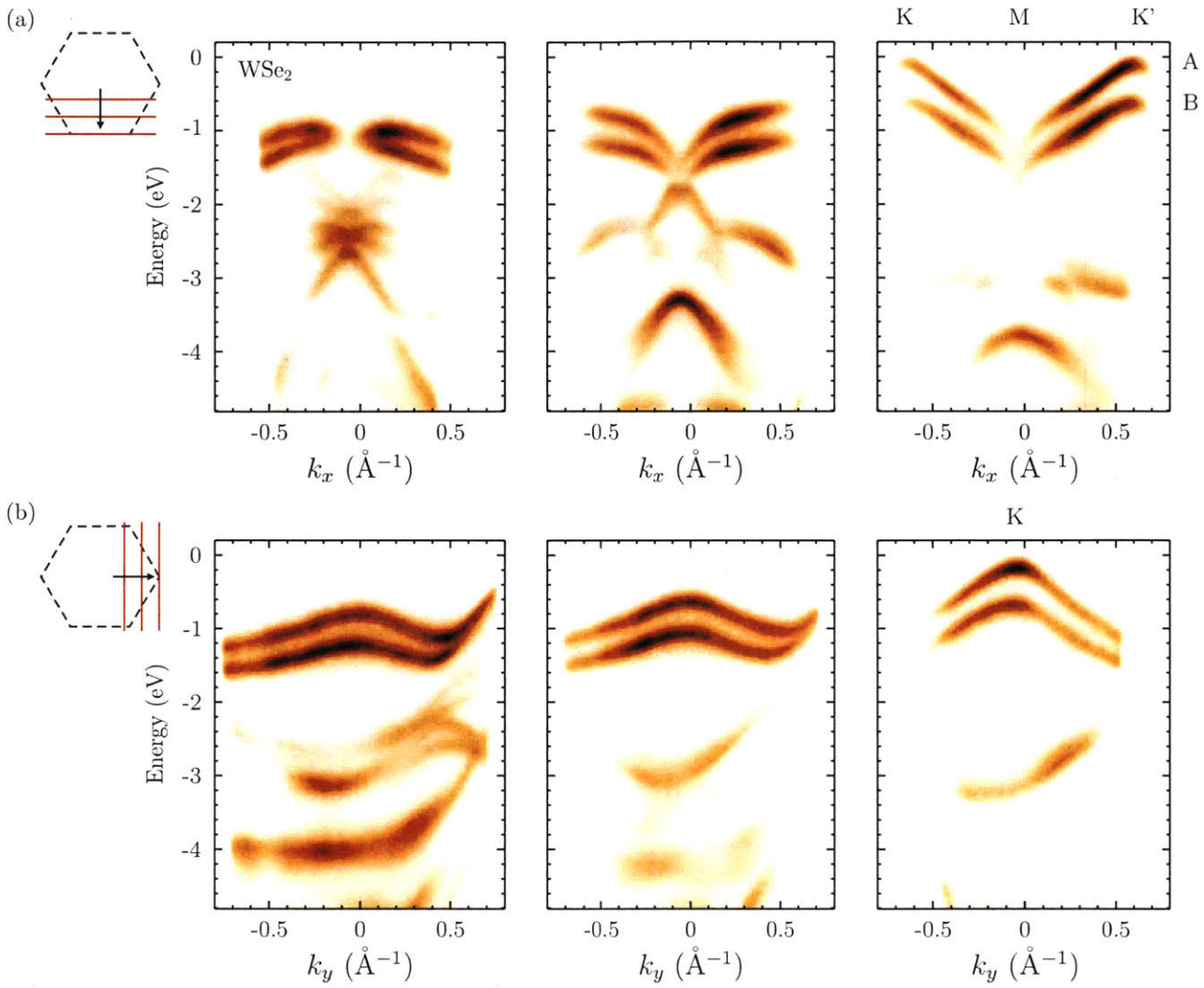

Figure 8.11: ARPES bandstructure of bulk WSe_2. **(a)** $E(k_x)$ linecuts as k_y is varied between Γ & M. **(b)** $E(k_y)$ linecuts as k_x is varied between Γ & K.

$(K \rightarrow K)$ and indirect $(\Gamma \rightarrow Q)$ gaps in bulk WSe_2. Note that WSe_2 is an indirect gap semiconductor where the conduction band minimum is located halfway along the $\Gamma - K$ direction, denoted as Q valley. Due to the low symmetry of this point, there are 6 inequivalent Q valleys in the Brillouin zone. By using TR-ARPES with 1.59 eV pump and 30 eV probe we can study the dynamics of photoexcited electrons in bulk WSe_2. **Figure 8.12a-b** shows that the photoexcited electrons are found to quickly accumulate at the Q valleys and stay there with lifetime longer than 4 ps. In addition, there is a very short-lived signal at around time-zero at energy within the gap. We ascribe this to photon-dressed replicas of

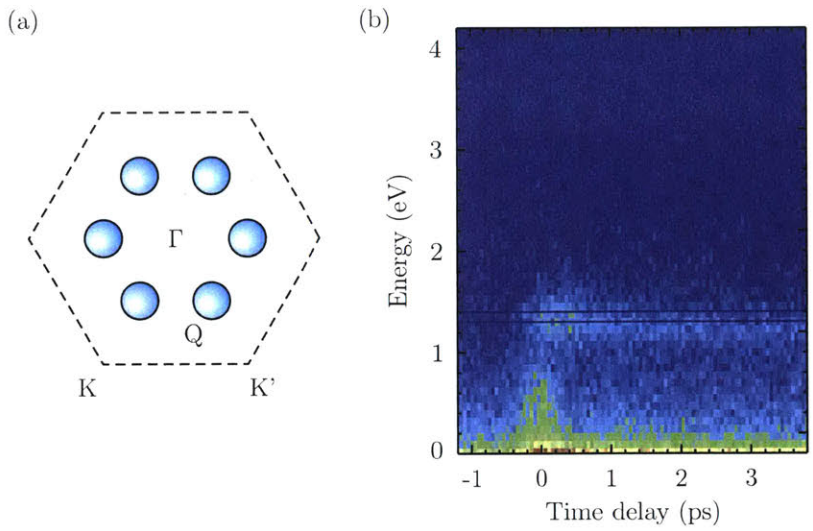

Figure 8.12: (a) Brillouin zone of WSe_2 showing the six inequivalent Q valleys located in between Γ and K points. **(b)** Population lifetime of the excited electrons in the Q valleys.

the lower valence bands that are induced by the pump pulse. Clear observation of such photon-dressed replicas is hindered by dissipation due to photoexcited electrons.

In order to obtain a clearer observation of photon-dressed replicas in TMDs, we must pick a system where dissipation can be avoided. Bulk WS_2 is an ideal material system for this purpose because, though it has an indirect gap of 1.41 eV ($\Gamma \rightarrow Q$), it has a direct gap of 1.77 eV ($K \rightarrow K$) that is larger than the pump photon energy 1.59 eV. This allows us to induce photon-dressed replicas in the absence of photoexcited electrons (figure not shown). Here we can ignore phonon-assisted optical transition in the lowest order approximation.

8.2.2. WTe_2 semimetal

WTe_2 is a semimetal TMD with 1T' lattice structure. The crystal structure is strongly anisotropic due to Jahn-Teller distortion (1T→1T') between adjacent W atoms that perpendicularly dimerize along the resulting W chain. Recently, this material is reported to exhibit a large non-saturating magnetoresistance [163] and predicted to be a Type-II Weyl semimetal [164], which established a tremendous interest in condensed matter physics community. The bandstructure of bulk WTe_2 is calculated in Reference [1] and shown in

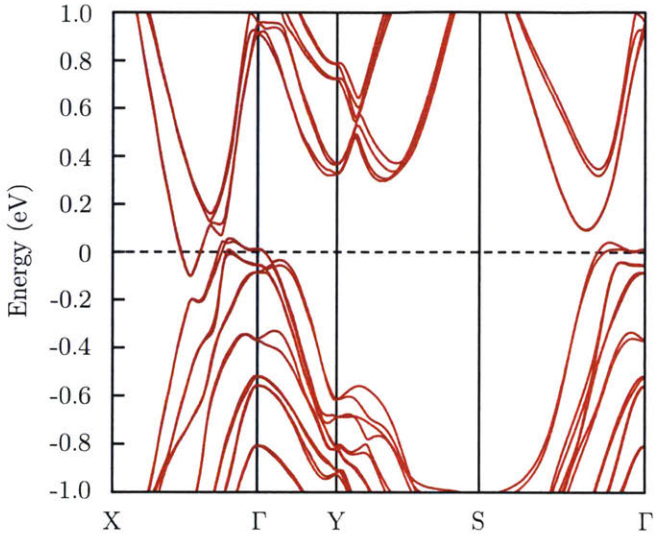

Figure 8.13: Calculated bandstructure of bulk WTe_2. Figure is obtained from Reference [1].

Fig 8.13. The Fermi level intersects both the electron pocket in conduction band and the hole pocket in valence band, which overlap significantly. Moreover, the two pockets have similar sizes at the Fermi level that suggests that carrier compensation is responsible for the reported large magnetoresistance [165]. However, little is known about the nonequilibrium dynamics between these carriers, which could provide more direct information on their interactions.

Figure 8.14a shows the bandstructure of WTe_2 measured using 30 eV ARPES at 30 K. We can identify the electron pocket across the Fermi level rather well. By plotting the energy distribution curve of the electron pocket, we can measure the energy resolution of this system **(Fig 8.15)**. Meanwhile, the hole pocket feature is not as clear in this measurement, though a separate measurement using 6 eV ARPES can show both electron and hole pockets very clearly (not plotted here). **Figure 8.14b-c** shows the TR-ARPES results before and after photoexcitation of 1.59 eV. The promoted electrons at higher-energy bands allow us to reveal the energy dispersion of up to 500 meV above the Fermi level. By tuning the time delay between the pump and probe pulses, the carrier lifetimes can be measured and their dynamics can be studied. Further analysis in this direction is currently under progress.

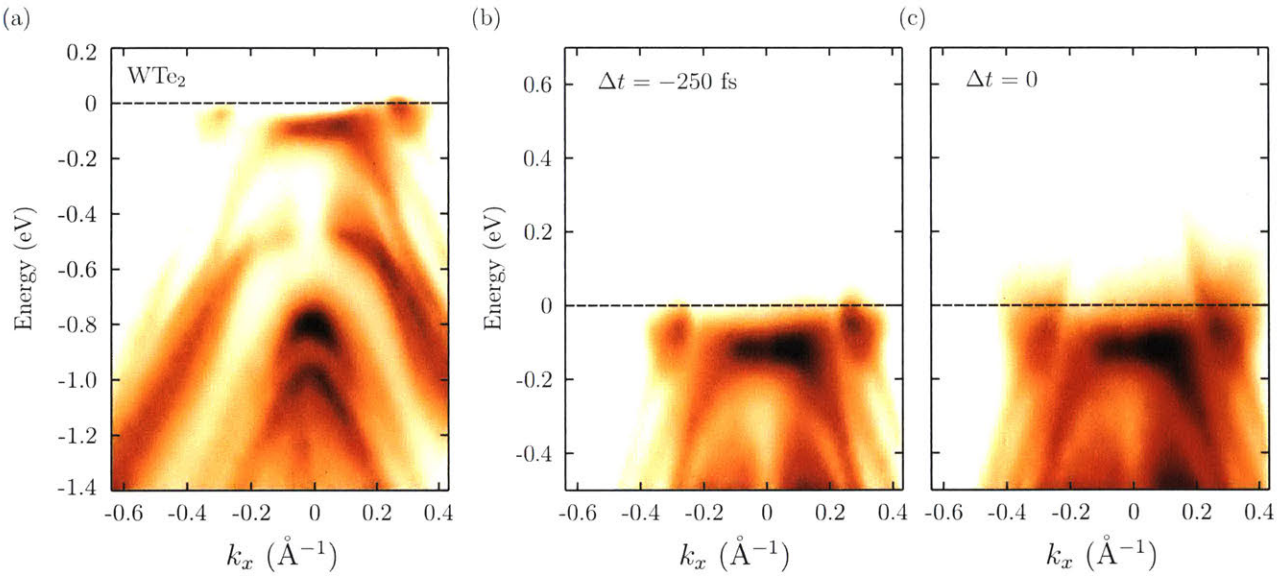

Figure 8.14: (a) ARPES bandstructure of bulk WTe_2 in equilibrium measured using 30 eV XUV. **(b)** TR-ARPES results of bulk WTe_2 at 250 fs before NIR pump pulse arrives, and **(c)** at zero delay.

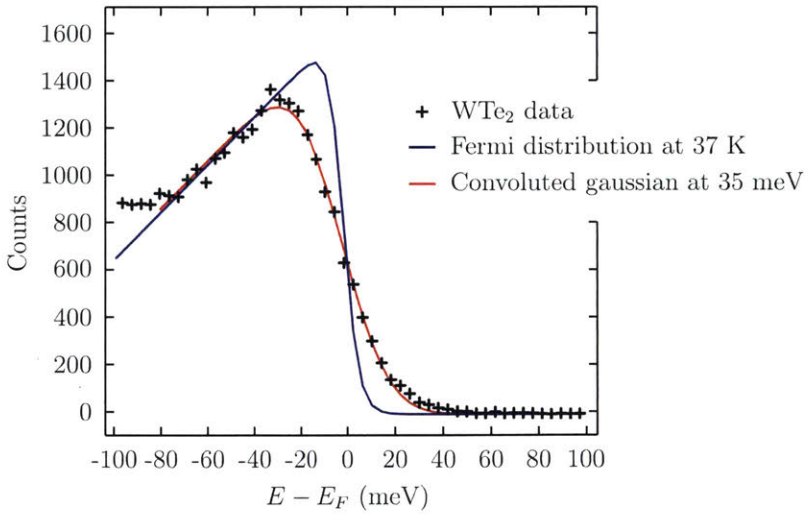

Figure 8.15: Energy resolution of our XUV ARPES setup as measured from the electron pocket of bulk WTe_2 at 37 K.

References:

1. J. Jiang et al. "Signature of strong spin-orbital coupling in the large nonsaturating magnetoresistance material WTe_2". *Phys. Rev. Lett.* **115**, 166601 (2015).
2. G. B. Liu, W. Y. Shan, Y. G. Yao, W. Yao, and D. Xiao. "Three-band tight-binding model for monolayers of group-VIB transition metal dichalcogenides". *Phys. Rev. B* **88**, 085433 (2013).
3. H. Yuan et al. "Generation and electric control of spin-valley-coupled circular photogalvanic current in WSe_2". *Nature Nano.* **9**, 851-7 (2014).
4. K. Kośmider, J. W. González, and J. Fernández-Rossier. "Large spin splitting in the conduction band of transition metal dichalcogenide monolayers". *Phys. Rev. B* **88**, 245436 (2013).
5. A. Kormányos et al. "k·p theory for two-dimensional transition metal dichalcogenide semiconductors". *2D Materials* **2**, 022001 (2015).
6. A. Chernikov et al. "Exciton binding energy and nonhydrogenic Rydberg series in monolayer WS_2". *Phys. Rev. Lett.* **113**, 076802 (2014).
7. A. H. Castro Neto, F. Guinea, N. M. R. Peres, K. S. Novoselov, and A. K. Geim. "The electronic properties of graphene". *Rev. Mod. Phys.* **81**, 109-162 (2009).
8. S. Ryu, C. Mudry, C. Y. Hou, and C. Chamon. "Masses in graphenelike two-dimensional electronic systems: Topological defects in order parameters and their fractional exchange statistics". *Phys. Rev. B* **80**, 205319 (2009).
9. E. Wang et al. "Gaps induced by inversion symmetry breaking and second-generation Dirac cones in graphene/hexagonal boron nitride". *Nature Phys.* **12**, 1111-1115 (2016).
10. Y. H. Lee et al. "Synthesis of large-area MoS_2 atomic layers with chemical vapor deposition". *Adv. Mater.* **24**, 2320-5 (2012).
11. Y. H. Lee et al. "Synthesis and transfer of single-layer transition metal disulfides on diverse surfaces". *Nano Lett.* **13**, 1852-7 (2013).
12. S. Wachter, D. K. Polyushkin, O. Bethge, and T. Mueller. "A microprocessor based on a two-dimensional semiconductor". *Nature Commun.* **8**, 14948 (2017).
13. K. F. Mak, C. Lee, J. Hone, J. Shan, and T. F. Heinz. "Atomically thin MoS_2: a new direct-gap semiconductor". *Phys. Rev. Lett.* **105**, 136805 (2010).
14. A. Splendiani et al. "Emerging photoluminescence in monolayer MoS_2". *Nano Lett.* **10**, 1271-5 (2010).
15. D. Xiao, G. B. Liu, W. Feng, X. Xu, and W. Yao. "Coupled spin and valley physics in monolayers of MoS_2 and other group-VI dichalcogenides". *Phys. Rev. Lett.* **108**, 196802 (2012).
16. G. B. Liu, D. Xiao, Y. Yao, X. Xu, and W. Yao. "Electronic structures and theoretical modelling of two-dimensional group-VIB transition metal dichalcogenides". *Chem. Soc. Rev.* **44**, 2643-63 (2015).

17. X. X. Zhang, Y. You, S. Y. Zhao, and T. F. Heinz. "Experimental Evidence for Dark Excitons in Monolayer WSe_2". *Phys. Rev. Lett.* **115**, 257403 (2015).

18. K. F. Mak, K. L. He, J. Shan, and T. F. Heinz. "Control of valley polarization in monolayer MoS_2 by optical helicity". *Nature Nano.* **7**, 494-498 (2012).

19. H. L. Zeng, J. F. Dai, W. Yao, D. Xiao, and X. D. Cui. "Valley polarization in MoS_2 monolayers by optical pumping". *Nature Nano.* **7**, 490-493 (2012).

20. T. Cao et al. "Valley-selective circular dichroism of monolayer molybdenum disulphide". *Nature Commun.* **3**, 887 (2012).

21. R. R. Alfano and S. L. Shapiro. "Observation of self-phase modulation and small-scale filaments in crystals and glasses". *Phys. Rev. Lett.* **24**, 592-594 (1970).

22. A. B. Kuzmenko. "Kramers–Kronig constrained variational analysis of optical spectra". *Rev. Sci. Instrum.* **76**, 083108 (2005).

23. L. A. Falkovsky. "Optical properties of graphene". *J. Phys. Conf. Ser.* **129**, 012004 (2008).

24. T. Stauber, N. M. R. Peres, and A. K. Geim. "Optical conductivity of graphene in the visible region of the spectrum". *Phys. Rev. B* **78**, 085432 (2008).

25. E. Hecht, *Optics*. 4th ed. Addison-Wesley (2002).

26. E. J. Sie, A. J. Frenzel, Y.-H. Lee, J. Kong, and N. Gedik. "Intervalley biexcitons and many-body effects in monolayer MoS_2". *Phys. Rev. B* **92**, 125417 (2015).

27. K. F. Mak, K. L. McGill, J. Park, and P. L. McEuen. "Valleytronics. The valley Hall effect in MoS_2 transistors". *Science* **344**, 1489-92 (2014).

28. S. Wu et al. "Electrical tuning of valley magnetic moment through symmetry control in bilayer MoS_2". *Nature Phys.* **9**, 149-153 (2013).

29. E. J. Sie et al. "Valley-selective optical Stark effect in monolayer WS_2". *Nature Mater.* **14**, 290-4 (2015).

30. J. Kim et al. "Ultrafast generation of pseudo-magnetic field for valley excitons in WSe_2 monolayers". *Science* **346**, 1205-8 (2014).

31. A. R. Klots et al. "Probing excitonic states in suspended two-dimensional semiconductors by photocurrent spectroscopy". *Sci. Rep.* **4**, 6608 (2014).

32. H. M. Hill et al. "Observation of excitonic Rydberg states in monolayer MoS_2 and WS_2 by photoluminescence excitation spectroscopy". *Nano Lett.* **15**, 2992-7 (2015).

33. K. F. Mak et al. "Tightly bound trions in monolayer MoS_2". *Nature Mater.* **12**, 207-11 (2013).

34. J. S. Ross et al. "Electrical control of neutral and charged excitons in a monolayer semiconductor". *Nature Commun.* **4**, 1474 (2013).

35. C. H. Lui et al. "Trion-induced negative photoconductivity in monolayer MoS_2". *Phys. Rev. Lett.* **113**, 166801 (2014).

36. A. Singh et al. "Coherent electronic coupling in atomically thin $MoSe_2$". *Phys. Rev. Lett.* **112**, 216804 (2014).

37. C. Mai et al. "Many-body effects in valleytronics: direct measurement of valley lifetimes in single-layer MoS_2". *Nano Lett.* **14**, 202-6 (2014).

38. Y. Song and H. Dery. "Transport theory of monolayer transition-metal dichalcogenides through symmetry". *Phys. Rev. Lett.* **111**, 026601 (2013).

39. A. Kormányos et al. "Monolayer MoS_2: Trigonal warping, the Γ valley, and spin-orbit coupling effects". *Phys. Rev. B* **88**, 045416 (2013).

40. T. Cheiwchanchamnangij and W. R. L. Lambrecht. "Quasiparticle band structure calculation of monolayer, bilayer, and bulk MoS_2". *Phys. Rev. B* **85**, 205302 (2012).

41. T. Yu and M. W. Wu. "Valley depolarization due to intervalley and intravalley electron-hole exchange interactions in monolayer MoS_2". *Phys. Rev. B* **89**, 205303 (2014).

42. C. R. Zhu et al. "Exciton valley dynamics probed by Kerr rotation in WSe_2 monolayers". *Phys. Rev. B* **90**, 161302(R) (2014).

43. J. Shang et al. "Observation of excitonic fine structure in a 2D transition-metal dichalcogenide semiconductor". *ACS Nano* **9**, 647-55 (2015).

44. D. Kleinman. "Binding energy of biexcitons and bound excitons in quantum wells". *Phys. Rev. B* **28**, 871-879 (1983).

45. J. Singh, D. Birkedal, V. Lyssenko, and J. Hvam. "Binding energy of two-dimensional biexcitons". *Phys. Rev. B* **53**, 15909-15913 (1996).

46. A. Thilagam. "Exciton complexes in low dimensional transition metal dichalcogenides". *J. Appl. Phys.* **116**, 053523 (2014).

47. K. W. Stone et al. "Two-quantum 2D FT electronic spectroscopy of biexcitons in GaAs quantum wells". *Science* **324**, 1169-73 (2009).

48. D. B. Turner and K. A. Nelson. "Coherent measurements of high-order electronic correlations in quantum wells". *Nature* **466**, 1089-92 (2010).

49. J. Inoue and A. Tanaka. "Photoinduced transition between conventional and topological insulators in two-dimensional electronic systems". *Phys. Rev. Lett.* **105**, 017401 (2010).

50. T. Kitagawa, T. Oka, A. Brataas, L. Fu, and E. Demler. "Transport properties of nonequilibrium systems under the application of light: Photoinduced quantum Hall insulators without Landau levels". *Phys. Rev. B* **84**, (2011).

51. N. H. Lindner, G. Refael, and V. Galitski. "Floquet topological insulator in semiconductor quantum wells". *Nature Phys.* **7**, 490-495 (2011).

52. J. H. Shirley. "Solution of Schrodinger Equation with a Hamiltonian Periodic in Time". *Phys. Rev.* **138**, B979-B987 (1965).

53. S. H. Autler and C. H. Townes. "Stark effect in rapidly varying fields". *Phys. Rev.* **100**, 703-722 (1955).

54. J. S. Bakos. "AC Stark effect and multiphoton processes in atoms". *Phys. Rep.* **31**, 209-235 (1977).

55. C. N. Cohen-Tannoudji and W. D. Phillips. "New mechanisms for laser cooling". *Physics Today* **43**, 33-40 (1990).

56. B. H. Bransden and C. J. Joachain, *Physics of Atoms and Molecules*. 2nd ed. Addison-Wesley (2003).

57. E. T. Jaynes and F. W. Cummings. "Comparison of quantum and semiclassical radiation theories with application to beam maser". *Proc. IEEE* **51**, 89-109 (1963).

58. M. Brune et al. "Quantum rabi oscillation: A direct test of field quantization in a cavity". *Phys. Rev. Lett.* **76**, 1800-1803 (1996).

59. H. R. Gutierrez et al. "Extraordinary room-temperature photoluminescence in triangular WS_2 monolayers". *Nano Lett.* **13**, 3447 (2012).

60. Y. H. Wang, H. Steinberg, P. Jarillo-Herrero, and N. Gedik. "Observation of Floquet-Bloch states on the surface of a topological insulator". *Science* **342**, 453-457 (2013).

61. M. Joffre, D. Hulin, A. Migus, and A. Antonetti. *J. Mod. Opt.* **35**, 1951 (1988).

62. D. Fröhlich, A. Nöthe, and K. Reimann. "Observation of the resonant optical Stark effect in a semiconductor". *Phys. Rev. Lett.* **55**, 1335-1337 (1985).

63. A. Mysyrowicz et al. "Dressed excitons in a multiple-quantum-well structure: Evidence for an optical Stark effect with femtosecond response time". *Phys. Rev. Lett.* **56**, 2748-2751 (1986).

64. D. S. Chemla et al. "The excitonic optical Stark effect in semiconductor quantum wells probed with femtosecond optical pulses". *J. Lumin.* **44**, 233-246 (1989).

65. C. Sieh et al. "Coulomb memory signatures in the excitonic optical Stark effect". *Phys. Rev. Lett.* **82**, 3112-3115 (1999).

66. A. Hayat et al. "Dynamic Stark effect in strongly coupled microcavity exciton polaritons". *Phys. Rev. Lett.* **109**, 033605 (2012).

67. N. S. Koster et al. "Giant dynamical Stark shift in germanium quantum wells". *Appl. Phys. Lett.* **98**, 161103 (2011).

68. M. Combescot. "Optical Stark effect of the exciton. II. Polarization effects and exciton splitting". *Phys. Rev. B* **41**, 3517-3533 (1990).

69. B. A. Bernevig, T. L. Hughes, and S. C. Zhang. "Quantum spin Hall effect and topological phase transition in HgTe quantum wells". *Science* **314**, 1757-1761 (2006).

70. P. M. Perez-Piskunow, G. Usaj, C. A. Balseiro, and L. E. F. F. Torres. "Floquet chiral edge states in graphene". *Phys. Rev. B* **89**, 121401(R) (2014).

71. X. Liu et al. "Strong light–matter coupling in two-dimensional atomic crystals". *Nature Photon.* **9**, 30-34 (2014).

72. C. Mai et al. "Exciton valley relaxation in a single layer of WS_2 measured by ultrafast spectroscopy". *Phys. Rev. B* **90**, 041414(R) (2014).

73. W. Zhao et al. "Evolution of electronic structure in atomically thin sheets of WS_2 and WSe_2". *ACS Nano* **7**, 791-7 (2013).

74. M. Asada, A. Kameyama, and Y. Suematsu. "Gain and intervalence band absorption in quantum-well lasers". *IEEE J. Quant. Electron.* **20**, 745-753 (1984).

75. T. C. Berkelbach, M. S. Hybertsen, and D. R. Reichman. "Theory of neutral and charged excitons in monolayer transition metal dichalcogenides". *Phys. Rev. B* **88**, 045318 (2013).

76. S. Schmittrink and D. S. Chemla. "Collective excitations and the dynamic Stark effect in a coherently driven exciton system". *Phys. Rev. Lett.* **57**, 2752-2755 (1986).

77. E. J. Sie, C. H. Lui, Y. H. Lee, J. Kong, and N. Gedik. "Observation of intervalley biexcitonic optical Stark effect in monolayer WS_2". *Nano Lett.* **16**, 7421-7426 (2016).

78. A. Von Lehmen, D. S. Chemla, J. P. Heritage, and J. E. Zucker. "Optical Stark effect on excitons in GaAs quantum wells". *Opt. Lett.* **11**, 609 (1986).

79. M. Combescot and R. Combescot. "Excitonic Stark shift: A coupling to "semivirtual" biexcitons". *Phys. Rev. Lett.* **61**, 117-120 (1988).

80. D. Hulin and M. Joffre. "Excitonic optical Stark redshift: The biexciton signature". *Phys. Rev. Lett.* **65**, 3425-3428 (1990).

81. Y. Li et al. "Measurement of the optical dielectric function of monolayer transition-metal dichalcogenides: MoS_2, $MoSe_2$, WS_2, and WSe_2". *Phys. Rev. B* **90**, 205422 (2014).

82. H. Wang, C. Zhang, and F. Rana. "Ultrafast dynamics of defect-assisted electron-hole recombination in monolayer MoS_2". *Nano Lett.* **15**, 339-45 (2015).

83. J. R. Schaibley et al. "Population pulsation resonances of excitons in monolayer $MoSe_2$ with sub-1 meV linewidths". *Phys. Rev. Lett.* **114**, 137402 (2015).

84. Q. Wang et al. "Valley carrier dynamics in monolayer molybdenum disulfide from helicity-resolved ultrafast pump-probe spectroscopy". *ACS Nano* **7**, 11087-93 (2013).

85. S. Sim et al. "Exciton dynamics in atomically thin MoS_2: Interexcitonic interaction and broadening kinetics". *Phys. Rev. B* **88**, 075434 (2013).

86. H. Shi et al. "Exciton dynamics in suspended monolayer and few-layer MoS_2 2D crystals". *ACS Nano* **7**, 1072-80 (2013).

87. E. A. Pogna et al. "Photo-induced bandgap renormalization governs the ultrafast response of single-layer MoS_2". *ACS Nano* **10**, 1182-8 (2016).

88. A. Steinhoff, M. Rosner, F. Jahnke, T. O. Wehling, and C. Gies. "Influence of excited carriers on the optical and electronic properties of MoS_2". *Nano Lett.* **14**, 3743-8 (2014).

89. Y. You et al. "Observation of biexcitons in monolayer WSe_2". *Nature Phys.* **11**, 477-481 (2015).

90. I. Kylänpää and H.-P. Komsa. "Binding energies of exciton complexes in transition metal dichalcogenide monolayers and effect of dielectric environment". *Phys. Rev. B* **92**, 205418 (2015).

91. X. Xu, W. Yao, D. Xiao, and T. F. Heinz. "Spin and pseudospins in layered transition metal dichalcogenides". *Nature Phys.* **10**, 343-350 (2014).

92. E. del Valle et al. "Two-photon lasing by a single quantum dot in a high-Q microcavity". *Phys. Rev. B* **81**, 035302 (2010).

93. S. Schumacher et al. "Cavity-assisted emission of polarization-entangled photons from biexcitons in quantum dots with fine-structure splitting". *Opt. Express* **20**, 5335-42 (2012).

94. Y. Li et al. "Valley splitting and polarization by the Zeeman effect in monolayer $MoSe_2$". *Phys. Rev. Lett.* **113**, 266804 (2014).

95. D. MacNeill et al. "Breaking of valley degeneracy by magnetic field in monolayer $MoSe_2$". *Phys. Rev. Lett.* **114**, 037401 (2015).

96. G. Aivazian et al. "Magnetic control of valley pseudospin in monolayer WSe_2". *Nature Phys.* **11**, 148-152 (2015).

97. A. Srivastava et al. "Valley Zeeman effect in elementary optical excitations of monolayer WSe_2". *Nature Phys.* **11**, 141-147 (2015).

98. J. B. Stark, W. H. Knox, and D. S. Chemla. "Spin-resolved femtosecond magnetoexciton interactions in GaAs quantum wells". *Phys. Rev. B* **46**, 7919-7922 (1992).

99. S. A. Crooker, D. D. Awschalom, J. J. Baumberg, F. Flack, and N. Samarth. "Optical spin resonance and transverse spin relaxation in magnetic semiconductor quantum wells". *Phys. Rev. B* **56**, 7574-7588 (1997).

100. M. Combescot and R. Combescot. "Optical Stark effect of the exciton: Biexcitonic origin of the shift". *Phys. Rev. B* **40**, 3788-3801 (1989).

101. S. Schmitt-Rink, D. S. Chemla, and H. Haug. "Nonequilibrium theory of the optical Stark effect and spectral hole burning in semiconductors". *Phys. Rev. B* **37**, 941-955 (1988).

102. E. J. Sie et al. "Large, valley-exclusive Bloch-Siegert shift in monolayer WS_2". *Science* **355**, 1066-1069 (2017).

103. C. Cohen-Tannoudji, J. Dupont-Roc, and G. Grynberg, *Atom-Photon Interactions.* Wiley-VCH (1998).

104. F. Bloch and A. Siegert. "Magnetic resonance for nonrotating fields". *Phys. Rev.* **57**, 522-527 (1940).

105. W. E. Lamb and R. C. Retherford. "Fine structure of the Hydrogen atom by a microwave method". *Phys. Rev.* **72**, 241-243 (1947).

106. H. A. Bethe. "The electromagnetic shift of energy levels". *Phys. Rev.* **72**, 339-341 (1947).

107. R. Grimm, M. Weidemüller, and Y. B. Ovchinnikov. "Optical dipole traps for neutral atoms". *Adv. At. Mol. Opt. Phys.* **42**, 95-170 (2000).

108. T. Niemczyk et al. "Circuit quantum electrodynamics in the ultrastrong-coupling regime". *Nature Phys.* **6**, 772-776 (2010).

109. P. Forn-Diaz et al. "Observation of the Bloch-Siegert shift in a qubit-oscillator system in the ultrastrong coupling regime". *Phys. Rev. Lett.* **105**, 237001 (2010).

110. J. Tuorila et al. "Stark effect and generalized Bloch-Siegert shift in a strongly driven two-level system". *Phys. Rev. Lett.* **105**, 257003 (2010).

111. M. D. Crisp. "Jaynes-Cummings model without the rotating-wave approximation". *Phys. Rev. A* **43**, 2430-2435 (1991).

112. P. Rivera et al. "Valley-polarized exciton dynamics in a 2D semiconductor heterostructure". *Science* **351**, 688-91 (2016).

113. J. R. Schaibley et al. "Valleytronics in 2D materials". *Nature Reviews Materials* **1**, 16055 (2016).

114. A. Kundu, H. A. Fertig, and B. Seradjeh. "Floquet-engineered valleytronics in Dirac systems". *Phys. Rev. Lett.* **116**, 016802 (2016).

115. J. E. Jones. "On the determination of molecular fields. II. From the equation of state of a gas". *Proc. R. Soc. A* **106**, 463-477 (1924).

116. J. E. Lennard-Jones. "Cohesion". *Proc. Phys. Soc.* **43**, 461-482 (1931).

117. J. B. Mock, G. A. Thomas, and M. Combescot. "Entropy ionization of an exciton gas". *Solid State Commun.* **25**, 279-282 (1978).

118. D. Semkat et al. "Ionization equilibrium in an excited semiconductor: Mott transition versus Bose-Einstein condensation". *Phys. Rev. B* **80**, 155201 (2009).

119. R. Zimmermann. "Dynamical T-matrix theory for high-density excitons in coupled quantum wells". *physica status solidi (b)* **243**, 2358-2362 (2006).

120. M. M. Ugeda et al. "Giant bandgap renormalization and excitonic effects in a monolayer transition metal dichalcogenide semiconductor". *Nature Mater.* **13**, 1091-5 (2014).

121. A. Chernikov, C. Ruppert, H. M. Hill, A. F. Rigosi, and T. F. Heinz. "Population inversion and giant bandgap renormalization in atomically thin WS_2 layers". *Nature Photon.* **9**, 466-470 (2015).

122. R. Schmidt et al. "Ultrafast Coulomb-induced intervalley coupling in atomically thin WS_2". *Nano Lett.* **16**, 2945-50 (2016).

123. C. Ruppert, A. Chernikov, H. M. Hill, A. F. Rigosi, and T. F. Heinz. "The role of electronic and phononic excitation in the optical response of monolayer WS_2 after ultrafast excitation". *Nano Lett.* **17**, 644-651 (2017).

124. D. R. Wake, H. W. Yoon, J. P. Wolfe, and H. Morkoç. "Response of excitonic absorption spectra to photoexcited carriers in GaAs quantum wells". *Phys. Rev. B* **46**, 13452-13460 (1992).

125. N. Peyghambarian et al. "Blue shift of the exciton resonance due to exciton-exciton interactions in a multiple-quantum-well structure". *Phys. Rev. Lett.* **53**, 2433-2436 (1984).

126. D. Hulin et al. "Well-size dependence of exciton blue shift in GaAs multiple-quantum-well structures". *Phys. Rev. B* **33**, 4389-4391 (1986).

127. K. H. Schlaad et al. "Many-particle effects and nonlinear optical properties of GaAs/(Al,Ga)As multiple-quantum-well structures under quasistationary excitation conditions". *Phys. Rev. B* **43**, 4268-4275 (1991).

128. S. Schmitt-Rink, D. Chemla, and D. Miller. "Theory of transient excitonic optical nonlinearities in semiconductor quantum-well structures". *Phys. Rev. B* **32**, 6601-6609 (1985).

129. Y. Yu et al. "Fundamental limits of exciton-exciton annihilation for light emission in transition metal dichalcogenide monolayers". *Phys. Rev. B* **93**, (2016).

130. D. Sun et al. "Observation of rapid exciton-exciton annihilation in monolayer molybdenum disulfide". *Nano Lett.* **14**, 5625-9 (2014).

131. Y. Chen et al. "Temperature-dependent photoluminescence emission and Raman scattering from $Mo_{1-x}W_xS_2$ monolayers". *Nanotechnology* **27**, 445705 (2016).

132. M. Rösner, E. Şaşıoğlu, C. Friedrich, S. Blügel, and T. O. Wehling. "Wannier function approach to realistic Coulomb interactions in layered materials and heterostructures". *Phys. Rev. B* **92**, 085102 (2015).

133. L. Yuan and L. Huang. "Exciton dynamics and annihilation in WS_2 2D semiconductors". *Nanoscale* **7**, 7402-8 (2015).

134. P. D. Cunningham, K. M. McCreary, and B. T. Jonker. "Auger recombination in chemical vapor deposition-grown monolayer WS_2". *J. Phys. Chem. Lett.* **7**, 5242-5246 (2016).

135. A. V. Stier, K. M. McCreary, B. T. Jonker, J. Kono, and S. A. Crooker. "Exciton diamagnetic shifts and valley Zeeman effects in monolayer WS_2 and MoS_2 to 65 Tesla". *Nature Commun.* **7**, 10643 (2016).

136. C. Schindler and R. Zimmermann. "Analysis of the exciton-exciton interaction in semiconductor quantum wells". *Phys. Rev. B* **78**, 045313 (2008).

137. P. Steinleitner et al. "Direct observation of ultrafast exciton formation in a monolayer of WSe_2". *Nano Lett.* **17**, 1455-1460 (2017).

138. F. Ceballos, Q. Cui, M. Z. Bellus, and H. Zhao. "Exciton formation in monolayer transition metal dichalcogenides". *Nanoscale* **8**, 11681-8 (2016).

139. B. Gao et al. "Studies of intrinsic hot phonon dynamics in suspended graphene by transient absorption microscopy". *Nano Lett.* **11**, 3184-9 (2011).

140. P. H. Handel and C. Kittel. "Van der Waals interactions and exciton condensation". *Proc. Nat. Acad. Sci. USA* **68**, 3120-1 (1971).

141. A. L. Ivanov and H. Haug. "Existence of exciton crystals in quantum wires". *Phys. Rev. Lett.* **71**, 3182-3185 (1993).

142. J. Böning, A. Filinov, and M. Bonitz. "Crystallization of an exciton superfluid". *Phys. Rev. B* **84**, 075130 (2011).

143. C. Friedrich, S. Blügel, and A. Schindlmayr. "Efficient implementation of the GW approximation within the all-electron FLAPW method". *Phys.Rev. B* **81**, 125102 (2010).

144. A. A. Mostofi et al. "An updated version of wannier90: A tool for obtaining maximally-localised Wannier functions". *Comput. Phys. Commun.* **185**, 2309-2310 (2014).

145. A. Ramasubramaniam. "Large excitonic effects in monolayers of molybdenum and tungsten dichalcogenides". *Phys. Rev. B* **86**, 115409 (2012).

146. A. Molina-Sánchez and L. Wirtz. "Phonons in single-layer and few-layer MoS_2 and WS_2". *Phys. Rev. B* **84**, 155413 (2011).

147. Y. H. Wang et al. "Observation of a warped helical spin texture in Bi_2Se_3 from circular dichroism angle-resolved photoemission spectroscopy". *Phys. Rev. Lett.* **107**, 207602 (2011).

148. Y. Wang, *Laser-based ARPES of Topological Insulators.* PhD Thesis, Harvard University, USA (2012).

149. F. Mahmood, *Femtosecond Spectroscopy of Coherent Phenomena in Quantum Materials.* PhD Thesis, Massachusetts Institute of Technology, USA (2016).

150. Y. H. Wang et al. "Measurement of intrinsic dirac fermion cooling on the surface of the topological insulator Bi_2Se_3 using time-resolved and angle-resolved photoemission spectroscopy". *Phys. Rev. Lett.* **109**, 127401 (2012).

151. M. Ferray et al. "Multiple-harmonic conversion of 1064 nm radiation in rare gases". *J. Phys. B* **21**, L31-L35 (1988).

152. X. F. Li, A. L'Huillier, M. Ferray, L. A. Lompré, and G. Mainfray. "Multiple-harmonic generation in rare gases at high laser intensity". *Phys. Rev. A* **39**, 5751-5761 (1989).

153. P. B. Corkum. "Plasma perspective on strong field multiphoton ionization". *Phys. Rev. Lett.* **71**, 1994-1997 (1993).

154. M. Lewenstein, P. Balcou, M. Y. Ivanov, A. L'Huillier, and P. B. Corkum. "Theory of high-harmonic generation by low-frequency laser fields". *Phys. Rev. A* **49**, 2117-2132 (1994).

155. P. Antoine, A. L'Huillier, M. Lewenstein, P. Salières, and B. Carré. "Theory of high-order harmonic generation by an elliptically polarized laser field". *Phys. Rev. A* **53**, 1725-1745 (1996).

156. T. Rohwer, *Ultrafast Dynamics in Correlated Materials - A Time-Resolved XUV ARPES Experiment.* PhD Thesis, University of Kiel, Germany (2013).

157. A. Rundquist. "Phase-matched generation of coherent soft X-rays". *Science* **280**, 1412-1415 (1998).

158. P. Balcou, C. Cornaggia, A. S. L. Gomes, L. A. Lompre, and A. L'Huillier. "Optimizing high-order harmonic generation in strong fields". *J. Phys. B* **25**, 4467-4485 (1992).

159. A. L'Huillier and P. Balcou. "High-order harmonic generation in rare gases with a 1-ps 1053-nm laser". *Phys. Rev. Lett.* **70**, 774-777 (1993).

160. L. Misoguti, I. P. Christov, S. Backus, M. M. Murnane, and H. C. Kapteyn. "Nonlinear wave-mixing processes in the extreme ultraviolet". *Phys. Rev. A* **72**, 063803 (2005).

161. J. H. Hubbell et al. "Atomic form factors, incoherent scattering functions, and photon scattering cross sections". *J. Phys. Chem. Ref. Data* **4**, 471-538 (1975).

162. B. L. Henke, E. M. Gullikson, and J. C. Davis. "X-Ray interactions: photoabsorption, scattering, transmission, and reflection at E = 50-30,000 eV, Z = 1-92". *At. Data Nucl. Data Tables* **54**, 181-342 (1993).

163. M. N. Ali et al. "Large, non-saturating magnetoresistance in WTe_2". *Nature* **514**, 205-8 (2014).

164. A. A. Soluyanov et al. "Type-II Weyl semimetals". *Nature* **527**, 495-8 (2015).

165. I. Pletikosic, M. N. Ali, A. V. Fedorov, R. J. Cava, and T. Valla. "Electronic structure basis for the extraordinary magnetoresistance in WTe_2". *Phys. Rev. Lett.* **113**, 216601 (2014).